LBL-31027

Lawrence Berkeley Laboratory

UNIVERSITY OF CALIFORNIA

Materials & Chemical Sciences Division

Part I: Kinetic Energy Dependencies of Selected Ion-Molecule Reactions.
Part II: Photochemistry of $(FSO_3)_2$, FSO_3, and FNO

J.D. Burley
(Ph.D. Thesis)

July 1991

LOAN COPY
Circulates
for 4 weeks
Bldg. 50 Library.
LBL-31027
Copy 2

Prepared for the U.S. Department of Energy under Contract Number DE-AC03-76SF00098

DISCLAIMER

This document was prepared as an account of work sponsored by the United States Government. While this document is believed to contain correct information, neither the United States Government nor any agency thereof, nor the Regents of the University of California, nor any of their employees, makes any warranty, express or implied, or assumes any legal responsibility for the accuracy, completeness, or usefulness of any information, apparatus, product, or process disclosed, or represents that its use would not infringe privately owned rights. Reference herein to any specific commercial product, process, or service by its trade name, trademark, manufacturer, or otherwise, does not necessarily constitute or imply its endorsement, recommendation, or favoring by the United States Government or any agency thereof, or the Regents of the University of California. The views and opinions of authors expressed herein do not necessarily state or reflect those of the United States Government or any agency thereof or the Regents of the University of California.

LBL-31027

Part I: Kinetic Energy Dependencies of Selected Ion-Molecule Reactions.
Part II: Photochemistry of $(FSO_3)_2$, FSO_3, and FNO

J.D. Burley
(Ph.D. Thesis)

Department of Chemistry
University of California

and

Chemical Sciences Division
Lawrence Berkeley Laboratory
University of California
Berkeley, CA 94720

July 1991

This work was supported by the Director, Office of Energy Research,
Office of Basic Energy Sciences, Division of Chemical Sciences,
of the U.S. Department of Energy under Contract No. DE-AC03-76SF00098

Part I: Kinetic Energy Dependencies of Selected Ion - Molecule Reactions.

Part II: Photochemistry of $(FSO_3)_2$, FSO_3 , and FNO.

by

Joel David Burley

Department of Chemistry
University of California

and

Chemical Sciences Division
Lawrence Berkeley Laboratory
1 Cyclotron Road
Berkeley, CA 94720

ABSTRACT

In Part I, guided ion beam mass spectrometry is used to study the ion - molecule reactions $O^+(^4S) + H_2$ (D_2, HD), $O^+(^4S) + N_2$, $C^+(^2P) + O_2$ and $C^+(^2P) + N_2$. Integral reaction cross sections are measured as a function of kinetic energy in the center-of-mass frame. Reaction mechanisms and dynamics are examined, and the results are compared to the predictions of phase space theory. In some cases, thermochemistry for neutral and ionic species is derived.

In Part II, photoabsorption cross sections are measured for peroxydisulfuryl difluoride, $(FSO_3)_2$, and the fluorosulfate radical, FSO_3. Photoabsorption cross sections of nitrosyl fluoride, FNO, are also measured, and the FNO absorption spectrum is analyzed and assigned. Spectral results for FNO are compared to the predictions of *ab initio* calculations and to those obtained for the isoelectronic compound HONO.

Table of Contents

Part I: Kinetic Energy Dependencies of Selected Ion - Molecule Reactions.

Chapter 1: Experimental Techniques 1

1.1 General

1.2 Kinetic Energies

1.3 $O^+(^4S)$ Ion Source

1.4 $C^+(^2P)$ Ion Source

1.5 References

Chapter 2: Kinetic Energy Dependence of $O^+(^4S) + H_2$ (D_2, HD) 12

2.1 Introduction

2.2 Experimental

2.2.1 Pressure Dependence
2.2.2 Reaction Rates

2.3 Results

2.3.1 $O^+ + H_2, D_2$
2.3.2 $O^+ + HD$
2.3.3 Rate Constants

2.4 Discussion

2.4.1 Low Energy Behavior
2.4.2 Intermediate Energy Behavior
2.4.3 High Energy Behavior
2.4.4 Intramolecular Isotope Effect

2.5 Conclusion

2.6 Appendix: Conservation of Orbital Angular Momentum

2.7 References

Chapter 3: Kinetic Energy Dependence of $O^+(^4S) + N_2$ 46

3.1 Introduction

3.2 Results

3.2.1 Charge Transfer Reaction
3.2.2 Nitrogen Atom Abstraction: Cross Sections
3.2.3 Nitrogen Atom Abstraction: Rate Constants

3.3 Discussion

3.4 Conclusion

3.5 References

Chapter 4: Kinetic Energy Dependence of $C^+(^2P) + O_2$ 73

4.1 Introduction

4.2 Experimental

4.2.1 Pressure Dependence
4.2.2 Reaction Rates

4.3 Results

4.3.1 Total Cross Sections and Rate Constants
4.3.2 Branching Ratio: $O^+ + CO$ vs. $CO^+ + O$
4.3.3 $O_2^+ + C$
4.3.4 $CO^+ + O$: High Energies
4.3.5 $O^+ + CO$: High Energies

4.4 Discussion

4.4.1 Phase Space Calculations
4.4.2 Electronic State Correlations
4.4.3 Doublet Surfaces
4.4.4 Quartet Surfaces
4.4.5 Branching Ratio and Reaction Efficiency

4.5 Conclusion

4.6 Appendix: Molecular Orbital Correlations and Potential Energy Surfaces

4.6.1 C_{2v} Symmetry: Doublet Surfaces
4.6.2 C_{2v} Symmetry: Quartet Surfaces
4.6.3 $C_{\infty v}$ Symmetry

4.7 References

Chapter 5: Kinetic Energy Dependence of $C^+(^2P) + N_2$ 114

5.1 Introduction

5.1.1 Thermochemistry

5.2 Experimental

5.3 Results

5.3.1 Cross Sections
5.3.2 Comparison with Other Studies

5.4 Discussion

5.4.1 Reaction Thresholds
5.4.2 Electronic State Correlation Diagram
5.4.3 Phase Space Calculations

5.5 Conclusion

5.6 References

Part II: Photochemistry of $(FSO_3)_2$, FSO_3 , and FNO.

Chapter 6: Photoabsorption Cross Sections of $(FSO_3)_2$ and FSO_3 140

6.1 Introduction

6.2 Experimental

6.2.1 Cary Spectrometer
6.2.2 Temperature-Regulated Cell
6.2.3 Vacuum System
6.2.4 Sample
6.2.5 Experimental Procedure: Dimer Cross Sections, 180 - 360 nm
6.2.6 Experimental Procedure: Radical and Dimer Cross Sections, 340 - 450 nm

6.3 Results and Discussion

6.3.1 Dimer Cross Section Measurements at 298 K
6.3.2 Temperature-Dependent Measurements
6.3.3 Comparisons with Croce's Previous $\sigma(FSO_3)$ Measurements
6.3.4 Dimer Cross Section Measurements, 340 - 450 nm

6.4 Conclusion

6.5 References

Chapter 7: Spectroscopy and Photoabsorption Cross Sections of FNO 161

7.1 Introduction

7.2 Experimental

7.2.1 FNO Synthesis
7.2.2 Absorption Cell, Vacuum System
7.2.3 Cary Spectrometer

7.3 Results

7.3.1 Absorption Cross Sections, 350 - 180 nm
7.3.2 Vibronic Spectrum, 350 - 240 nm

7.4 Discussion

7.4.1 Summary of Spectral Assignments
7.4.2 Theoretical Studies
7.4.3 Comparisons with HONO

7.5 Appendix: FNO Photoabsorption Cross Sections, 350 - 180 nm

7.6 References

ACKNOWLEDGEMENTS

During my graduate studies I have had the good fortune to work closely with two men who are both outstanding scientists and all-around, classy individuals: Professors Peter B. Armentrout and Harold S. Johnston. Without their support, guidance, and enthusiasm this thesis would not have been possible. I thank Peter and Hal for all their assistance and wish them and their families the best of luck in the future.

Thanks are also extended to Kent Ervin, who took me under his wing and taught me the basics of running guided ion beam experiments, and to other members of the Armentrout Group: Natasha Aristov, Jerry Elkind, Rosy Georgiadis, Steve Loh, David Hales, Lee Sunderlin, Mary Ellen Weber, Rich Schultz, and B. H. Boo. I thank Lee for allowing me to invade his apartment during completion of the C^+ + N_2 project, and Dave Clemmer for his long-distance help with photocopies.

In the Johnston Group, thanks are in order to Daniel Oh, Doug Kinnison, Wade Sisk, Phil Hunter, Bongsoo Kim, Ken Patten, and Chip Miller. Wade deserves special recognition for his efforts to maintain group decorum, and so does Phil, who provided the computer code used to automate the Cary spectrometer. Ken supplied bountiful emotional support during the two-year NO_2 experiment from hell (not presented here), and Chip was a bottomless source of good ideas and an invaluable collaborator on the FNO project.

Bill Casteel and Rika Hagiwara of the research group of Professor Neil Bartlett provided the FNO and $(FSO_3)_2$ samples used in Part II. I thank them for their help and synthetic expertise, and for many helpful discussions.

Thanks are also in order to David, Kay, and especially Brooke, who provided unlimited support on the home front. Finally, I thank my family for their encouragement over the past six years.

Chapter One

Experimental Techniques

1.1 GENERAL

Since the apparatus used in these investigations has been described in detail elsewhere,[1,2] only a brief description is given here. Ground state O^+ and C^+ ions are produced in a source discussed below. The ions are extracted from the source, focused by a series of electrostatic lenses, and accelerated for mass analysis in a magnetic momentum analyzer. After mass selection, the ion beam is decelerated to the desired kinetic energy and focused into an octopole ion beam guide. This device uses rf fields to create a potential well in the radial direction without altering the axial motion of the ions. The octopole guides the ion beam through an interaction region containing the reactant gas. Use of the octopole insures that both reactant and product ions are efficiently collected. All trapped ions are extracted from the octopole, focused into a quadrupole mass filter for mass analysis, and then detected by a Daly type[3] secondary electron scintillation detector. A DEC MINC computer controls the apparatus and automates data acquisition. Raw ion intensities are converted to absolute reaction cross sections as described previously.[1,2] These cross sections are corrected for random counting noise and for reactions which occur outside the gas cell. Overall, the absolute magnitudes of the cross section measurements are estimated to be accurate to $\pm 20\%$.

Reactant gas pressures within the interaction region are measured with a capacitance manometer, and are typically within the range 0.01 - 0.50 mTorr. This is sufficiently low that secondary ion - molecule collisions are relatively improbable. However, "single collision" conditions are not strictly applicable because there is always a finite probability of an incident ion encountering more than one neutral molecule as it passes through the reaction cell.[4] Cross sections measured for $O^+(^4S)$ + N_2 (Chapter 3)[5] and $C^+(^2P)$ + N_2 (Chapter 5)[6] are independent of pressure, as expected for processes due to a single ion - molecule collision. In contrast, cross sections measured for $O^+(^4S)$ + H_2 (Chapter 2)[7] and $C^+(^2P)$ + O_2 (Chapter 4)[8] display slight pressure dependencies, indicating the presence of multiple collisions. To overcome this difficulty, cross section measurements for these latter two systems are made over a range of reactant gas pressures and then extrapolated to zero pressure to obtain the true "single collision" cross sections. (Additional discussion on the topic of multiple collisions in the reaction cell is presented in Chapters 2 and 4.)

1.2 KINETIC ENERGIES

Unless stated otherwise, all energies quoted in Part I of this dissertation correspond to the center-of-mass (c.m.) interaction energy, E_0 , which for a stationary target is related to the laboratory ion energy by equation (1.1),

$$E_0 = E_{lab} \cdot M/(m + M) \qquad (1.1)$$

where M is the mass of the neutral target molecule and m is the mass of the incident ion. To determine the absolute zero and distribution of the ion energy, a retarding

field analysis is used in which the dc potential of the interaction region is swept through the nominal ion energy zero (i.e. the potential of exit plate of the drift cell ion source, discussed below). Since the interaction region and the energy analysis region are physically the same, this method avoids ambiguities resulting from space charge effects, contact potentials, and focusing aberrations. For the O^+ beams used in Chapters 2 and 3, the derivative of the retarding field analysis curve is very close to a Gaussian distribution. The true ion beam energy zero is taken as the peak of this distribution, which typically has a full width at half maximum (FWHM) of 0.30 to 0.35 eV in the laboratory frame.[5,7] For the C^+ beams used in Chapter 5 ($C^+(^2P)$ + N_2), the derivative distribution is also Gaussian, but the FWHM is a somewhat broader 0.50 eV lab.[6] For the C^+ beams used in Chapter 4 ($C^+(^2P)$ + O_2), the distribution is slightly non-Gaussian and the true ion beam energy zero is taken as the 50% fall-off point of the distribution. The typical FWHM measured for these non-Gaussian C^+ beams is approximately 0.50 eV lab.[8] The absolute uncertainty in the energy scale for all measurements presented here is estimated to be ± 0.05 eV in the laboratory frame.

At the very low energies in the fall-off region of the retarding analysis curve, the slower ions are truncated from the distribution. This produces a narrowing of the ion energy distribution at these low energies and makes it possible to extend the energy range for cross section measurements to below one FWHM of the beam energy spread. This procedure has been described in detail elsewhere.[1,2] It should be

noted, however, that the uncertainties in the energies in this region are larger than those at higher energies.

1.3 $O^+(^4S)$ ION SOURCE

Atomic oxygen ions are produced by electron impact (EI) ionization of CO_2 at electron energies (Ee) of 70 - 100 eV. According to Hughes and Tiernan,[9] a beam of O^+ produced from CO_2 at Ee = 60 eV consists of approximately 96% ground state (^4S) and 4% excited states (^2D and higher). At the higher Ee's used in these experiments, the fraction of excited state O^+ initially present in the beam could be somewhat larger. If molecular oxygen is used as the source gas in place of CO_2, then the percentage of excited state O^+ produced by 60 eV EI rises to 28%.[9,10] This makes O_2 a less attractive source gas for production of $O^+(^4S)$ than CO_2; however, O_2 is used as the source gas for experiments which test the effectiveness of the state selection process described below.

To remove the excited state ions produced by EI, the O^+ beam is injected into a high pressure drift cell containing molecular nitrogen as a bath gas. The drift cell is similar in design to the one described by Bowers and coworkers[11] and has been described in detail in a previous report.[12] In the drift cell, the ions undergo multiple collisions with the bath gas while under the influence of a weak electric field. The approximate residence time of the ions in the drift cell is given by equation (1.2),

$$\tau = Z/KE \qquad (1.2)$$

where K is the ion mobility in $cm^2\ V^{-1}\ s^{-1}$, Z is the drift distance (2 cm), and E is the electric field strength (2.5 V cm^{-1}). The ion mobility can be calculated from equation (1.3),

$$K = K_0(760/P)(T/273.16) \tag{1.3}$$

where K_0 is the reduced mobility, P is the pressure of the bath gas in Torr, and T is the temperature of the gas (300 K). Although the reduced mobility of O^+ in nitrogen has not been measured directly, the reduced mobilities for ions similar in mass to oxygen range from 2 - 3 $cm^2\ V^{-1}\ s^{-1}$.[13] At a pressure of 0.150 Torr, this corresponds to τ = 50 - 70 μs. The average number of collisions experienced by an ion traversing the cell can be obtained by multiplying the residence time of the ion by the rate constant for the collision process and the bath gas density. If one assumes the collisional rate constant predicted by the Langevin-Gioumousis-Stevenson model,[14]

$$k_{LGS} = 2\pi e(\alpha/\mu)^{1/2} \tag{1.4}$$

where e is the electronic charge, $\mu = mM/(m + M)$ is the reduced mass, and $\alpha(N_2)$ = 1.74 $Å^3$ is the polarizability of the nitrogen molecule,[15] then the collision rate is 9.7 x 10^{-10} $cm^3\ s^{-1}$ and O^+ undergoes between 200 and 350 collisions as it passes through the cell.

Besides translationally thermalizing the ions in the beam, these collisions remove the two metastable, electronically excited states of oxygen ion initially present, $O^+(^2D)$ and $O^+(^2P)$. The ^2D state (3.3 eV above the ground state) has a radiative lifetime of 3.6 hours and is removed via reaction (1.5) at a rate about 1/6 that given by equation (1.4).[16] The ^2P state (5.0 eV above the ground state) has a

radiative lifetime of 4.57 s and is removed via charge transfer with N_2, reaction (1.6), or the quenching process, reaction (1.7).[16] This latter process occurs at a rate about

$$O^+(^2D) + N_2 \rightarrow N_2^+ + O \tag{1.5}$$

$$O^+(^2P) + N_2 \rightarrow N_2^+ + O \tag{1.6}$$

$$O^+(^2P) + N_2 \rightarrow O^+(^4S) + N_2 \tag{1.7}$$

half the LGS limit, equation (1.4), while the rate for reaction (1.6) is an order of magnitude slower.[16] Ground state O^+ is also lost via reactions (1.8) and (1.9), but the

$$O^+(^4S) + N_2 \rightarrow NO^+ + N \tag{1.8}$$

$$O^+(^4S) + N_2 \rightarrow N_2^+ + O \tag{1.9}$$

efficiency of these processes is approximately 100 times less than that for removal of the excited state ions. The overall effect is thus a drastic reduction in the amount of excited state O^+ in the beam.

To determine the effectiveness of the state selection process, the charge transfer reaction of O^+ with N_2 is monitored in the main chamber as a function of kinetic energy. Since the ground state reaction, process (1.9), is endothermic by 1.96 eV and the excited state reactions, processes (1.5) and (1.6), are exothermic (by 1.36 and 3.06 eV, respectively, if they produce N_2^+ in the $X^2\Sigma_g^+$ ground state, or by 0.20 and 1.90 eV if they produce the $N_2^+(A^2\Pi_u)$ first excited state), the presence of $O^+(^2D)$ or $O^+(^2P)$ in the beam can be easily detected by the formation of N_2^+ at low interaction energies. This is shown graphically in Figure 1-1. As the pressure in the drift cell is increased, production of N_2^+ decreases. At drift cell pressures of 0.070 Torr or higher, low energy production of N_2^+ is no longer discernable from random

background noise, but above 2 eV the cross section for the reaction of $O^+(^4S)$ is clearly visible. For a beam initially consisting of 30% excited state (^2D and ^2P) ions, a rigorous upper limit of 0.06% can be placed on the total amount of excited state O^+ present after state selection at $P(N_2)$ = 70 mTorr by assuming that the baseline scatter at low energies results exclusively from reactions (1.5) and (1.6). To ensure that excited states are completely eliminated, the ion source conditions used in the Chapters 2 and 3 differ from those of Figure 1-1 in two respects. First, drift cell pressures are maintained at 0.150 ± 0.010 Torr, more than twice the maximum shown in Figure 1-1. This minimizes the effect of minor pressure fluctuations within the drift cell on the state selection process, and further insures that the excited state ions are completely removed. Second, CO_2 is used as the source gas so that fewer excited state ions are initially present.[9] Thus, the actual percentage of excited state ions in beams produced under these operating conditions is probably far below 0.06%.

1.4 $C^+(^2P)$ ION SOURCE

Ground state atomic carbon ions are produced in the same high-pressure drift cell[12] used to remove excited state O^+ ions.[17] Electrons are injected at a kinetic energy of approximately 75 eV into the 2 cm drift region, which contains 0.150 Torr of CO gas. The C^+ ions formed by electron-impact ionization undergo numerous collisions with the CO bath gas while being drawn through the drift cell by an electric field of ~ 1 V cm^{-1}. According to the same type of analysis used above for O^+,

these conditions will cause each C^+ ion to experience ~ 700 collisions as it passes through the cell. These collisions serve to thermalize the ions, removing any excited states initially present. The ions drift to the end of the cell, where they are extracted through a 1 mm diameter exit aperture into the mass selection region of the apparatus.

To test for the presence of excited state C^+ ions, the reaction $C^+ + D_2 \rightarrow CD^+ + D$ is monitored in the main chamber as a function of kinetic energy. Since the reaction of the ground state ion, process (1.10), is endothermic by 0.43 eV and the reaction of the first excited state, process (1.11), is exothermic by -4.90 eV, the

$$C^+(^2P) + D_2 \rightarrow CD^+ + D \qquad (1.10)$$

$$C^+(^4P) + D_2 \rightarrow CD^+ + D \qquad (1.11)$$

presence of excited state ions in the beam is easily detected by the cross section behavior at low kinetic energies.[12] This diagnostic technique is used to ensure that the carbon ion beams produced in the high pressure sources contain no excited state contamination.

1.5 REFERENCES

1. K. M. Ervin, Ph.D. Thesis, Department of Chemistry, University of California, Berkeley (1986).

2. K. M. Ervin and P. B. Armentrout, J. Chem. Phys. **83**, 166 (1985).

3. N. R. Daly, Rev. Sci. Instrum. **31**, 264 (1960).

4. At the low pressures of the present study, the probability of a jth order collision is given by $(n \cdot \ell \cdot \sigma_{LGS})^j$, where n is the number density of the neutral target molecule, ℓ is the length of the interaction region (8.6 cm), and σ_{LGS} is the ion - molecule collision cross section predicted by the Langevin-Gioumousis-Stevenson model.

5. J. D. Burley, K. M. Ervin, and P. B. Armentrout, J. Chem. Phys. **86**, 1944 (1987).

6. J. D. Burley, L. S. Sunderlin, and P. B. Armentrout, J. Chem. Phys., in press (1991).

7. J. D. Burley, K. M. Ervin, and P. B. Armentrout, Int. J. Mass Spectrom. Ion Proc. **80**, 153 (1987).

8. J. D. Burley and P. B. Armentrout, Int. J. Mass Spectrom. Ion Proc. **84**, 157 (1988).

9. B. M. Hughes and T. O. Tiernan, J. Chem. Phys. **55**, 3419 (1971).

10. B. R. Turner, J. A. Rutherford, and D. M. J. Compton, J. Chem. Phys. **48**, 1602 (1968).

11. P. A. M. Van Koppen, P. R. Kemper, A. J. Illies, and M. T. Bowers, Int. J. Mass Spectrom. Ion Proc. **54**, 263 (1983).

12. K. M. Ervin and P. B. Armentrout, J. Chem. Phys. **84**, 6738 (1986).

13. E. W. McDaniel and E. A. Mason, The Mobility and Diffusion of Ions in Gases, (Wiley, New York, 1973), Table 7-1-H-1.

14. G. Gioumousis and D. P. Stevenson, J. Chem. Phys. **29**, 294 (1958).

15. E. W. Rothe and R. B. Bernstein, J. Chem. Phys. **31**, 1619 (1959).

16. E. E. Ferguson, F. C. Fehsenfeld, and D. L. Albritton, in Gas Phase Ion Chemistry **1**, edited by M. T. Bowers (Academic, New York, 1979), p. 53.

17. For some of the data in Chapter 5, ground state C^+ ions were formed in a flow tube source discussed in detail in R. H. Schultz and P. B. Armentrout, Int. J. Mass Spectrom. Ion Proc., submitted for publication (1991). The flow tube and drift cell sources yield comparable results.

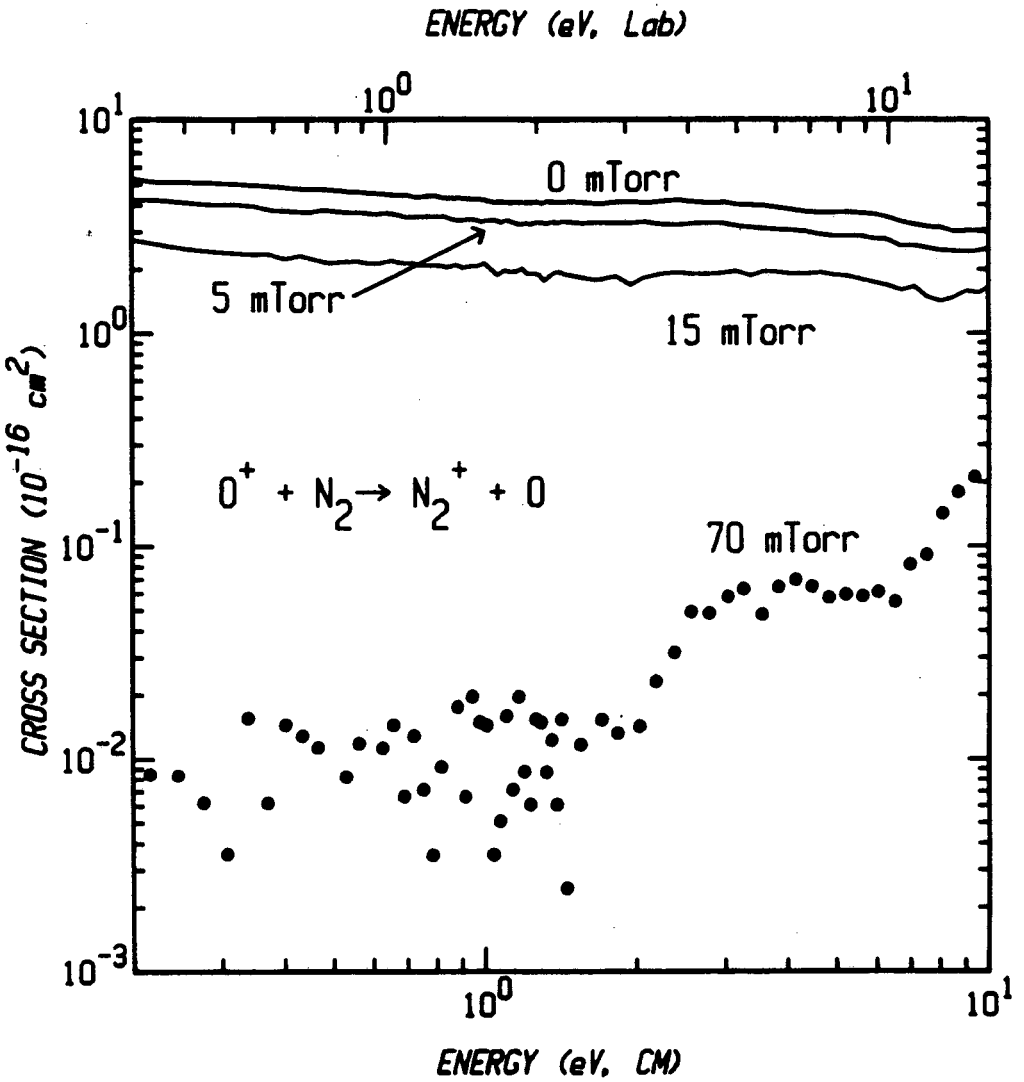

Figure 1-1. Cross sections for the charge transfer reaction of O^+ with N_2 as a function of relative translational energy (lower scale) and laboratory energy (upper scale). The O^+ is generated by electron impact ionization of O_2 at 70 eV. Results are shown for four different nitrogen pressures in the drift cell.

Chapter Two

Kinetic Energy Dependence of $O^+(^4S) + H_2$ (D_2, HD)

2.1 INTRODUCTION

Considering the amount of attention focused upon most ion - molecule reactions of possible astrophysical significance, the reactions of ground state atomic oxygen ion with molecular hydrogen and its isotopic variants, processes (2.1), (2.2), and (2.3),[1] have received relatively little attention from kineticists. The handful of

$$O^+(^4S) + H_2 \rightarrow OH^+(^3\Sigma^-) + H \qquad \Delta H^\circ = -0.54 \text{ eV} \qquad (2.1)$$

$$O^+(^4S) + D_2 \rightarrow OD^+(^3\Sigma^-) + D \qquad \Delta H^\circ = -0.51 \text{ eV} \qquad (2.2)$$

$$O^+(^4S) + HD \rightarrow OH^+(^3\Sigma^-) + D \qquad \Delta H^\circ = -0.51 \text{ eV} \qquad (2.3a)$$

$$\rightarrow OD^+(^3\Sigma^-) + H \qquad \Delta H^\circ = -0.55 \text{ eV} \qquad (2.3b)$$

experimental studies of reactions (2.1) - (2.3) which have been published in the literature currently consist of the differential cross section studies of Gillen, Mahan, and Winn (GMW),[2-4] the ion beam and luminescence measurements of Harris and Leventhal,[5,6] and a variety of rate constant determinations.[7-10] That relatively few experiments have been performed on reactions (2.1) - (2.3) is especially noteworthy in light of the large amount of work done on similar ion - molecule systems such as $O^+ + N_2 \rightarrow NO^+ + N$[11] and $Ar^+ + H_2 \rightarrow ArH^+ + H$.[12]

A general estimate of the magnitudes and energy dependences of the total reaction cross sections for processes (2.1) - (2.3) can be obtained from the Langevin-

Gioumousis-Stevenson (LGS) model for exothermic ion - molecule reactions.[13] This is given by equation (2.4),

$$\sigma_{LGS}(E) = \pi e(2\alpha/E)^{1/2} \tag{2.4}$$

where σ_{LGS} is the reaction cross section, E is the interaction energy of the reactants, e is the charge of the electron, and α is the polarizability of the target molecule ($\alpha(H_2) = 0.790$ Å^3, $\alpha(HD) = 0.783$ Å^3, $\alpha(D_2) = 0.775$ Å^3).[14] Interestingly, there is at present no well-studied example of a simple ion - molecule reaction whose experimentally measured cross section quantitatively matches the prediction of the LGS model. Of the many ion - molecule reactions studied prior to the present investigation, the reaction of argon ion with molecular hydrogen was long thought to match the LGS prediction. However, recent measurements on this system show that the cross section actually ranges from two-thirds σ_{LGS} at thermal energies up to about 90% of σ_{LGS} at $\sim$ 0.6 eV.[12]

While the LGS model can provide insight into a wide range of exothermic ion - molecule reactions when applied in an appropriate manner, it is sometimes abused.[15] Many times, this abuse results because deficiencies inherent in the model are not taken into account. Some of the deficiencies can be remedied by including higher order terms in the long range potential. Others can be corrected by explicitly considering the conservation of angular momentum or treating the reaction in a statistical fashion. Still others require detailed trajectory calculations on accurate *ab initio* potential energy surfaces.

Because the H_2O^+ system is relatively simple, accurate *ab initio* calculations of its potential energy surface are computationally feasible. For a collinear approach of reactants, calculations[16-19] generally agree that no barrier to reaction exists. For a perpendicular approach, calculations[20-23] indicate that the quartet surface is strongly repulsive such that a barrier to reaction of 4 to 7 eV is present.[2,22] These considerations have been summarized by GMW and others in the form of an electronic state correlation diagram.[2,6,20] They suggest that at low energies reactions (2.1) - (2.3) will occur primarily via direct, adiabatic processes where the reactants approach is near-collinear. Product formation should be restricted, however, for perpendicular approaches of the reactants.[2] Unfortunately, no trajectory calculations utilizing these detailed potential energy surfaces have been performed to obtain the cross sections for reactions (2.1) - (2.3).

In the present chapter, the kinetic energy dependencies of reactions (2.1) - (2.3) from 0.01 to 30 eV are investigated through the use of guided ion beam mass spectrometry. The results are compared to simple LGS theory (and an extension thereof which considers the quadrupole moment of H_2) and to phase space calculations of the cross sections. Several points are of particular interest. Does the LGS model accurately predict the magnitudes and energy dependences of the experimental cross sections? Does the extension of the model or phase space theory provide a better prediction than the LGS model? Does the requirement of a collinear approach inhibit reaction? If so, what is the energy dependence of this orientational limitation? What

intermolecular and intramolecular isotope effects are observed for the reactions with D_2 and HD? Are these accurately predicted by the various models?

2.2 EXPERIMENTAL

2.2.1 Pressure Dependence

In the present systems, formation of secondary and tertiary products, such as reactions (2.5) and (2.6), occurs very efficiently.[1,24] Therefore, it is necessary to pay

$$OH^+ + H_2 \rightarrow OH_2^+ + H \quad \Delta H^\circ = -1.0 \text{ eV} \tag{2.5}$$

$$OH_2^+ + H_2 \rightarrow OH_3^+ + H \quad \Delta H^\circ = -1.9 \text{ eV} \tag{2.6}$$

particular attention to the pressure dependence of reactions (2.1) - (2.3). Although it is possible to maintain reactant gas pressures low enough such that the probability of secondary or higher order collisions is essentially zero, such pressures are below the measurable range of the capacitance manometer. To overcome this difficulty, two different techniques are employed. In the first technique (discussed previously in Chapter 1), cross section measurements are made over a range of pressures and then extrapolated to zero pressure to obtain the true "single collision" cross section. In the second technique, second and third order product channels (i.e. reactions (2.5) and (2.6)) are monitored during experimental scans, and cross sections are adjusted to account for loss of primary product due to secondary and tertiary collisions. These two methods give very similar results and both are used to analyze the data for reactions (2.1) and (2.2). Only the first technique is used for reaction (2.3) because

of isotopic overlap between primary and higher order product channels (e.g. OD^+ and OH_2^+).

2.2.2 Reaction Rates

In order to compare the present results to previous flowing afterglow (FA),[7] ion cyclotron resonance (ICR),[8] and selected ion flow tube (SIFT) studies,[9,10] the cross sections must be converted into rate constants. The phenomenological rate constant is expressed by equation (2.7),

$$k(\langle E \rangle) = v_0 \cdot \sigma(E_0) \tag{2.7}$$

where $v_0 = (2E_0/\mu)^{1/2}$. The rate constants are a function of the mean relative energy of the reactants, $\langle E \rangle = E_0 + (3/2)\gamma k_B T$, where $\gamma = m/(m + M)$, k_B is the Boltzmann constant, and T is the temperature of the reactant gas (305 K). In the limit that $E_0 \rightarrow 0$, $k(\langle E \rangle)$ approaches the "bulk" thermal rate constant for the temperature $T' = \gamma \cdot T$. In most cases, the room temperature rate constant can be estimated by examining the behavior of $k(\langle E \rangle)$ at the lowest interaction energies. For reactions (2.1) - (2.3), $k(\langle E \rangle)$ is essentially constant at low values of $\langle E \rangle$. Accurate estimates of $k(T = 305\ K)$ are therefore obtained by fitting the low energy $k(\langle E \rangle)$ data to a horizontal line.

2.3 RESULTS

2.3.1 $O^+ + H_2, D_2$

A representative set of experimental results for reaction (2.1) is shown in Figure 2-1, along with the cross section predicted by the LGS model, equation (2.4).

At low interaction energies the agreement between the data and the model is excellent. A numerical fit to several sets of data over the range $0.015 \leq E_0 \leq 0.3$ eV is given by $\sigma(E_0) = (16.0 \pm 0.4)\ E_0^{-0.50 \pm 0.02}$ Å^2. This is $7 \pm 3\%$ larger in magnitude than the Langevin prediction of $\sigma_{LGS}(E) = 15.0\ E^{-0.50}$ Å^2. The small discrepancy between the data and the LGS model is well within the $\pm 20\%$ uncertainty in the absolute cross sections.

At the very lowest energies, $E_0 < 0.015$ eV, the experimentally observed cross section curves away from an $E^{-0.5}$ energy dependence. This deviation is believed to be an artifact which results from an inaccurate determination of the true ion energy distributions at these extremely low energies. For energies significantly below one FWHM of the beam spread (0.039 eV c.m.), the assumption that the ion energy distribution can be represented by a truncated Gaussian becomes questionable. This can lead to calculated average energies which are smaller than the true average energies produced in the laboratory. The net result of this process is that the cross sections calculated at the lowest energies are shifted to the left by a small amount, such that the apparent cross section begins to level off. For this reason, the lowest energy cross section (or rate constant) measurements are not included in any of the empirical fits in this study.

Upon reaching an interaction energy of ~ 0.3 eV, the experimentally observed cross section begins to deviate from the prediction of the LGS model. For the range $0.3 \leq E_0 \leq 6.0$ eV, the energy dependence of the data is $\sigma(E_0) = (10.3 \pm 0.3)\ E_0^{-0.81 \pm 0.02}$ Å^2. At $E_0 = 4.48$ eV, thermodynamic dissociation of the OH^+

product to O + H^+ becomes possible.[1] Shortly after this point the cross section falls off rapidly as $\sigma(E_0) = (1.25 \pm 0.50 \times 10^3)\ E_0^{-3.5 \pm 0.5}\ \text{Å}^2$.

Figure 2-2 presents representative results for reaction (2.2). Although the energy dependence of the D_2 cross section is nearly identical to that observed for H_2, the magnitude of the D_2 cross section is ~ 16% smaller. For the energy range $0.02 \leq E_0 \leq 0.25$ eV, the best fit to several sets of data is $\sigma(E_0) = (13.5 \pm 1.5) \times E_0^{-0.51 \pm 0.04}\ \text{Å}^2$, which is 9 ± 10% smaller than the Langevin prediction of $\sigma_{LGS}(E) = 14.8\ E^{-0.50}\ \text{Å}^2$. In the range $0.25 \leq E_0 \leq 5$ eV the energy dependence is $\sigma(E_0) = (8.36 \pm 0.30)\ E_0^{-0.74 \pm 0.04}\ \text{Å}^2$. The thermodynamic threshold for dissociation of OD^+ is 4.56 eV.[1] At energies somewhat above this point, the cross section declines as $\sigma(E_0) = (2.15 \pm 0.25 \times 10^3)\ E_0^{-3.6 \pm 0.1}\ \text{Å}^2$.

2.3.2 O^+ + HD

Representative results for reaction (2.3) are shown in Figure 2-3. The magnitude of the total cross section is intermediate to the magnitudes observed for H_2 and D_2, and the energy dependence of the total cross section is the same as that seen for H_2 and D_2. In the region $0.015 \leq E_0 \leq 0.25$ eV, the cross section takes on the form $\sigma(E_0) = (14.3 \pm 1.7)\ E_0^{-0.52 \pm 0.03}\ \text{Å}^2$. This is 4 ± 11% smaller than the Langevin prediction of $\sigma_{LGS}(E) = 14.9\ E^{-0.50}\ \text{Å}^2$. Between 0.25 and 6 eV, the form is $\sigma(E_0) = (10.3 \pm 0.5)\ E_0^{-0.75 \pm 0.03}\ \text{Å}^2$, and in the high energy region the cross section falls as $\sigma(E_0) = (1.13 \pm 0.50 \times 10^3)\ E_0^{-3.3 \pm 0.4}$.

As Figure 2-3 shows, the manner in which the product is partitioned between the hydride and deuteride channels shows considerable deviations from a 1:1 ratio. In

addition, the energy dependencies of the two product channels differ from each other and from the energy dependence shown by the total reaction cross section. Between interaction energies of 0.015 and 0.4 eV, the cross section for production of OH^+ shows the energy dependence $\sigma(E_0) = (9.71 \pm 1.50)\ E_0^{-0.47 \pm 0.10}\ \text{Å}^2$. Upon reaching 0.4 eV, a distinct break is noted and the energy dependence becomes $\sigma(E_0) = (5.95 \pm 0.20)\ E_0^{-1.0 \pm 0.06}\ \text{Å}^2$. This rate of decline is maintained until about 7 eV. At energies above 7 eV, the cross section falls off as $\sigma(E_0) = (250 \pm 150)\ E_0^{-2.8 \pm 0.3}\ \text{Å}^2$. For the OD^+ channel, the lowest energy region, 0.015 - 0.4 eV, is best fit by $\sigma(E_0) = (4.17 \pm 1.50)\ E_0^{-0.64 \pm 0.12}\ \text{Å}^2$. In the intermediate region, 0.4 - 5.3 eV, the data take the form $\sigma(E_0) = (4.30 \pm 0.25)\ E_0^{-0.50 \pm 0.11}\ \text{Å}^2$. Finally, at energies above 5.3 eV, the cross section falls as $\sigma(E_0) = (1.78 \pm 0.70 \times 10^3)\ E_0^{-3.9 \pm 0.3}\ \text{Å}^2$.

The isotopic branching ratio between reactions (2.3a) and (2.3b) is shown in Figure 2-4 in terms of the hydride product fraction. Initially, the hydride fraction is equal to 0.56. As the interaction energy is increased the hydride fraction becomes larger and eventually reaches a maxima of 0.66 near 0.4 eV. It then declines sharply and reaches a minima of 0.38 near 5 eV. At still higher energies, dissociation of the deuteride product becomes significant, and the hydride fraction increases rapidly. This is a result of the different fall-off rates for the hydride and deuteride products, Figure 2-3.

2.3.3 Rate Constants

In Figure 2-5, the rate constants for reactions (2.1) - (2.3) are plotted as a function of the mean relative interaction energy, $\langle E \rangle$. The data have been

converted from the cross sections shown in Figures 2-1 through 2-3 to rate constants via the use of equation (2.7). Also shown in Figure 2-5 are the rate constants predicted by the LGS model,[13]

$$k_{LGS} = 2\pi e(\alpha/\mu)^{1/2} \tag{2.8}$$

which is independent of the interaction energy. For reactions (2.1) - (2.3), the k_{LGS} values are 1.56, 1.15 and 1.30, respectively, in units of 10^{-9} cm^3 s^{-1}. The generally good agreement between the experimental results and k_{LGS} is clear in this figure, as are deviations from k_{LGS}.

Experimental room temperature rate constants for reactions (2.1) - (2.3) are determined as described above. The results are 1.67, 1.04, and 1.25, respectively, in units of 10^{-9} cm^3 s^{-1}. The rate constants for reactions (2.3a) and (2.3b) are 0.71 and 0.54 x 10^{-9} cm^3 s^{-1}, respectively. In Table 2-I, the present result for reaction (2.1) is compared to room temperature rate constants from the literature. Close agreement exists between the present result and the ICR measurement of Kim *et al.*[8] and the SIFT value of Smith *et al.*.[9] Less favorable comparisons are noted with an early flowing afterglow value from Fehsenfeld *et al.*[7] (these results are known to be systematically too high) and a recent SIFT measurement by Lindinger and co-workers.[10] While few experimental details are given in this last paper, one possible explanation for the discrepancy is the presence of excited state O^+. Kim *et al.*[8] have shown (Table 2-I) that the rate constant for reaction of excited state oxygen ions with H_2 is considerably less than for $O^+(^4S)$.

2.4 DISCUSSION

2.4.1 Low Energy Behavior

The comparison between the present data and the LGS model at energies below 0.3 eV is excellent. The experimental values for the three systems average $\sim 2 \pm 10\%$ smaller than the theoretical values. This agreement implies that the two main assumptions upon which the Langevin model is based are valid for the $O^+ + H_2$ (D_2, HD) system. These assumptions are: (1) the collision cross section is determined primarily by the long range, ion-induced dipole potential and (2) reaction occurs upon every ion - molecule collision.[13] Because of the latter assumption, the Langevin model ordinarily serves as an upper limit to experimental reaction cross sections. In the $O^+ + H_2$ (D_2, HD) system, it therefore appears that production of OH^+ (OD^+) is occurring with approximately 100% efficiency.

The LGS model as formulated in equations (2.4) and (2.8) ignores several higher order terms in the long range potential between O^+ and H_2. It therefore cannot be used to make a rigorous prediction of the behavior of the $O^+ + H_2$ system. H_2 has a permanent quadrupole moment ($Q = 1.23 \times 10^{-26}$ esu cm^2)[25] such that the "normal" ion-induced dipole potential used in the derivation of the LGS cross section,

$$V(r) = -e^2\alpha/2r^4 \tag{2.9}$$

is incomplete. The leading correction is given by equation (2.10),

$$V(r,\Theta) = (3 \cdot \cos^2\Theta - 1) \cdot Qe/2r^3 \tag{2.10}$$

where r is the ion - molecule distance, and Θ is the angle between the H_2 axis and the line of centers. This leads to a potential which is repulsive for $\Theta = 0°$ (collinear approach) and attractive for $\Theta = 90°$ (perpendicular approach).

The effect of the angular dependence of equation (2.10) on the rate of reaction has been treated approximately by Su and Bowers[26] in their average quadrupole orientation (AQO) model. Using this approach, the potential is averaged over all permissible values of Θ. A Langevin capture criterion is then applied, and the rate constant is determined on the basis of the reactants ability to surmount the centrifugal barrier. For reaction (2.1), k_{AQO} is found to be 1.61×10^{-9} cm^3 s^{-1}, in slightly better agreement with the experimental result than k_{LGS}, Table 2-I. For reactions (2.2) and (2.3), the values of k_{AQO} are 1.19 and 1.35×10^{-9} cm^3 s^{-1}, respectively, if $Q(D_2) = Q(HD) = Q(H_2)$. These values are in slightly worse agreement with the experimental results than the corresponding k_{LGS}'s. On average, the experimental results are 6 $\pm$ 10% less than the k_{AQO} values.

While the long range charge - quadrupole interaction favors a perpendicular approach of reactants, the perpendicular orientation presents an appreciable (4 to 7 eV) electronic barrier to reaction at small internuclear distances.[20-23] As mentioned in the introduction, this electronic barrier disappears if the reactants align in a collinear manner.[16,17,19] However, the collinear configuration results in a long range charge - quadrupole barrier of $\sim$ 0.07 eV.[12] Even a barrier as small as this would evidence itself as a distinct deviation from the $E^{-0.5}$ energy dependence observed at low energies.[27] Given these considerations, the efficiency of the reactions at low energies

implies that the reactants reorient from the perpendicular configuration favorable at long range to a collinear configuration as the internuclear distance decreases. At low interaction energies, there is apparently ample time for such a reorientation to take place.

One final feature of the low energy cross sections that deserves comment is the intermolecular isotope effect. The differences in magnitude which exist between the cross sections for reactions (2.1) and (2.2), and (2.1) and (2.3), are 17% and 11%, respectively. These discrepancies are substantially greater than the ~ 1% and ~ 0.5% differences which would be expected on the basis of polarizibility differences between H_2 and D_2, and H_2 and HD. (Since these differences in magnitude are not affected by the operating conditions of the experimental apparatus, it is unlikely that they are due to an experimental artifact.) At present, no explanation is offered for the larger than expected deviations, but it is noted that similar intermolecular isotope effects have been observed for other atomic ion + H_2, D_2, and HD systems.[27,28]

2.4.2 Intermediate Energy Behavior

At intermediate energies, 0.3 to 5.0 eV, the reaction cross section deviates below the LGS prediction. Effects which may act to reduce the likelihood of reactions (2.1) - (2.3) in this energy range are angular momentum constraints and the possibility of vibrational excitation of the H_2 (D_2, HD) target molecule. These processes can be examined in more detail by using phase space theory (PST). Phase space calculations were carried out for reactions (2.1) - (2.3) using modified versions of programs originally developed by Bowers and Chesnavich.[29]

The results of these calculations for reaction (2.1) are shown in Figure 2-6. The PST cross sections calculated for reactions (2.2) and (2.3) are identical to those calculated for hydrogen. The PST cross sections match the prediction of the LGS model at energies below 0.3 eV. This indicates that the phase space available to the exothermic products greatly exceeds that available to the reactants. Excellent agreement is noted between the phase space prediction and the experimentally observed cross sections at energies below ~ 1 eV, Figure 2-6. Most interesting is the fact that the PST cross sections deviate from σ_{LGS} at the same energy as the experimental data.

Additional PST calculations, also shown in Figure 2-6, demonstrate why the phase space cross sections deviate from σ_{LGS}. The deviation coincides with a rise in the PST cross section for no reaction, σ_{NR}. One reason for this is that the phase space available to the back reaction increases with increasing total energy. This is explicitly shown for the component of σ_{NR} which corresponds to vibrational excitation of the H_2 and has a thermodynamic onset of 0.55 eV. However, this effect alone is insufficient to account for the increase in the calculated σ_{NR}. The increase in this non-reactive process and the concomitant decrease in the reactive cross section result primarily from a restriction in the product cross section due to angular momentum conservation. Qualitatively, this restriction occurs because the reduced mass of the products (μ' = 0.95 amu) is about half that of the reactants (μ = 1.79 amu). This makes it difficult to conserve orbital angular momentum during product formation. At low energies, this conservation requirement is not a problem since the exothermicity of the reaction

is available to compensate. At intermediate energies, however, the reaction exothermicity is insufficient to compensate and the reaction cross section is limited by the exit channel impact parameter. (A more rigorous demonstration of this argument is given in the Appendix.)

While this reasoning probably explains the initial deviation of the phase space calculations and the experimental results from σ_{LGS}, the PST cross sections are larger than the experimental values at energies above 1 eV. One possible explanation for this behavior is a dynamic effect which PST cannot include. Namely, as the energy increases, increasingly less time is available for the reactants to reorient to a collinear geometry. The reaction becomes more direct and the efficiency of reaction declines. This must be accompanied by an increase in the back reaction (perhaps with vibrational excitation). Another possible explanation for this reduction is competition from the alternate reaction channel

$$O^+(^4S) + H_2(^1\Sigma_g^+) \rightarrow OH(X^2\Pi) + H^+(^1S). \qquad \Delta H = 0.06 \text{ eV} \qquad (2.11)$$

This reaction is probably unlikely since it is a spin-forbidden process. No evidence for this reaction exists in previous work. No attempt was made to study this process since the apparatus is not suitable for quantitative measurements of very low mass product ions.

2.4.3 High Energy Behavior

At 4.48 eV,[1] dissociation of the OH^+ product formed in reaction (2.1) becomes energetically allowed. While the cross section does fall off soon after this energy, no sharp change in the cross section is noted at this point. Instead, the onset

of product decline is spread over the range of 5 to 7 eV. The cross sections for reaction (2.2) behave similarly, as do the total cross sections for reaction (2.3). When the cross section data in this fall-off region are analyzed with a previously discussed fitting routine,[30] a dissociation energy of 6.25 $\pm$ 0.50 eV is obtained for reaction (2.1).[31] Table 2-II lists the results for similar analyses of reactions (2.2), (2.3a), and (2.3b). Since this empirically derived dissociation energy lies well above the thermodynamic onset of 4.48 eV, the implication is that some of the energy available to the products is preferentially placed in translation. The hypothesis of translational excitation of products is consistent with a direct reaction mechanism and the previous crossed beam results of GMW.[2]

A simple model which predicts such product excitation is the spectator stripping model (SSM).[32] This model assumes that the incident ion interacts with only one hydrogen atom, and that the second "spectator" atom experiences no change in its pre-collision velocity. Conservation of linear momentum fixes the relative translational energy of the products, and any excess energy goes into internal excitation of the OH^+. At a certain point, the amount of energy deposited in internal excitation becomes equal to the bond dissociation energy of the diatomic product and the product dissociates. The threshold for this dissociation is given by equation (2.12),

$$E_S = (D^\circ + \Delta H^\circ)\cdot(m_A+m_B)\cdot(m_B+m_C)/[m_B(m_A+m_B+m_C)] \qquad (2.12)$$

where D° is the bond dissociation energy of the product ion, ΔH° is the heat of reaction (negative for processes (2.1) - (2.3)), and m_A, m_B and m_C are the masses of

the incident ion, the transferred atom, and the spectator atom, respectively.[32] The calculated values of E_s for reactions (2.1) - (2.3) are given in Table 2-II and indicated by arrows in Figures 2-1 through 2-3. It can be seen in Table 2-II that the SSM predicts that E_s(2.3a) is smaller than $E_s(2.1) \approx E_s(2.2)$, which in turn are smaller than E_s(2.3b), as is observed experimentally. However, in all cases product dissociation begins before E_s and stable product formation extends beyond E_s. This is an indication that the experimentally observed translational excitation of products has a relatively broad distribution and is not sharply defined as predicted by the overly simplified SSM. A broad distribution can be rationalized via the physically realistic assumption that C is not merely a spectator, but interacts to a varying extent with A and B during the collision.

Another possible contribution to the cross section at energies in excess of E_s is the formation of electronically excited products. GMW have suggested that reaction (2.13) accounts for the product velocity vector distributions they observed for reaction

$$O^+(^4S) + H_2(^1\Sigma_g^+) \rightarrow OH^+(^1\Delta) + H(^2S) \qquad \Delta H = 1.66 \text{ eV} \qquad (2.13)$$

reaction (2.1) at interaction energies above E_s (8 eV).[2] Although GMW did not consider the formation of the second excited state,

$$O^+(^4S) + H_2(^1\Sigma_g^+) \rightarrow OH^+(A^3\Pi) + H(^2S) \qquad \Delta H = 2.31 \text{ eV} \qquad (2.14)$$

their results are probably consistent with this process as well. Production of $OH^+(A^3\Pi)$ seems somewhat more likely than production of $OH^+(^1\Delta)$ since reaction (2.14) is spin allowed while reaction (2.13) is spin forbidden. Furthermore, Harris and Leventhal have detected formation of $OH^+(A^3\Pi)$ by luminescence.[6] While their

results indicate that this product state comes from the reaction of excited O^+ ions at low kinetic energies, they attribute the formation of $OH^+(A^3\Pi)$ to the reaction of $O^+(^4S)$ at kinetic energies of 10 eV and above. This suggests that this reaction is not a major contributor to the cross sections observed here. Unfortunately, the present data provide no direct information about the electronic state distributions of the products.

2.4.4 Intramolecular Isotope Effect

The branching ratio observed for reactions (2.3a) and (2.3b), shown in Figure 2-4, varies extensively as a function of energy. At the lowest energies, where the total reaction proceeds with near 100% efficiency, reaction (2.3a) is preferred over reaction (2.3b) by a factor of 1.27. This differs substantially from the prediction of phase space theory, which favors the OD^+ product by a factor of 2 because it has more closely spaced rotational and vibrational energy levels than OH^+. This can be demonstrated by arbitrarily making the rotational and vibrational constants of the OH^+ and OD^+ products the same (a physical impossibility) while retaining the correct masses and reaction energetics. The result of this calculation is in better agreement with the data, Figure 2-4, and barely favors OD^+ since reaction (2.3b) is slightly more exothermic than reaction (2.3a). This comparison is consistent with the idea that this reaction does not proceed through a long lived OH_2^+ intermediate.

At low energies, formation of OH^+ may be favored by effects which influence the orientation of reactants into the required collinear configuration. This argument assumes that whichever atom of the HD molecule is directed towards the incoming

oxygen ion will be the one to transfer. For HD, the center of force (i.e. the geometric center of the molecule) is displaced from the center of mass. Consequently, the incoming ion exerts a torque on HD as it approaches. The torque tends to align the HD molecule with the H atom directed towards the incident ion, such that the OH^+ product is favored. This orientational effect has been examined in detail for reactant ions other than O^+ by George and Suplinskas,[33] Light and Chan,[34] and Hierl.[35]

As the kinetic energy is increased, formation of OH^+ is increasingly preferred in the experiment and by the PST. This effect is independent of the internal density of states as shown by comparison of the regular PST calculation and the physically unrealistic calculation. Rather, it results from the requirement that orbital angular momentum be conserved throughout the course of the reaction. Because the reduced mass of reaction (2.3a) is nearly twice that of reaction (2.3b), it is easier for reaction (2.3a) to conserve orbital angular momentum than it is for reaction (2.3b) [see the Appendix for additional discussion on this topic].

At energies above ~ 0.4 eV, the preference for reaction (2.3a) declines sharply. The turnabout is partially due to density of states considerations, as shown in Figure 2-4 by contrasting the PST calculations which take into account the density of states of the products to those which do not. However, density of states effects do not completely explain the rapid decline displayed by the experimental branching ratio. A possible reason for the more rapid decline in the branching ratio is that the reaction has a strong orientational preference. This preference can be understood by

considering the mass weighted or 'skewed' potential energy surfaces for collinear interactions of O^+ and HD.[36] The skew angle for reaction (2.3b) is 57° such that reaction can occur via a sequence of two hard-sphere collisions: O^+ hits D, and D hits H, sending it away from the newly formed OD^+. The skew angle for reaction (2.3a) is 38° such that reaction requires a sequence of four hard-sphere collisions: the light H atom chatters between the heavier O^+ and D atoms. Such a sequence is improbable, however, if the reaction is slightly off-collinear as will be the case most often experimentally. Thus, when the reaction can be approximated by hard-sphere collisions, i.e. at higher energies, the probability of forming OD^+ should be enhanced, as observed experimentally.

At the highest energies, the OH^+ product predominates due to product stability requirements. Because OD^+ is more likely to be formed with internal energy in excess of its dissociation energy than is OH^+ (see Table 2-II), the fraction of hydride product rises dramatically as the energy is increased. By the time an interaction energy of 30 eV is reached, the hydride product accounts for more than 90% of the total cross section. The phase space calculations do not include a provision for product dissociation and therefore should not be compared to the data at high energies.

2.5 CONCLUSION

The questions posed in the introduction are now easily answered. Total cross sections for the reactions of $O^+(^4S)$ with H_2, D_2, and HD show excellent agreement

with the predictions of the Langevin-Gioumousis-Stevenson model[13] at low energies (below ~ 0.3 eV). Within experimental error, the AQO theory[26] provides comparably good predictions. These models fail to predict the observed intermolecular isotope effect which finds that $\sigma(H_2) : \sigma(HD) : \sigma(D_2)$ is 1.0 : 0.89 : 0.84. The observation that the reaction efficiency is approximately unity is interesting since the potential energy surfaces for reactions (2.1) - (2.3) are known to be highly repulsive for perpendicular approaches of the reactants. The observed behavior demonstrates that at low kinetic energies, the reactants can orient into the favorable collinear geometry with near 100% probability.

At higher kinetic energies, the experimental cross sections decline below the LGS predictions. The initial decline is shown by comparison with phase space theory calculations to be due to angular momentum constraints in the exit channel. The general derivation of this effect in the Appendix shows that this type of behavior should be a common experimental observation. Further decreases in the reaction efficiency are attributed to the fact that at higher energies, the reactants have less time to reorient to the favored collinear geometry. At the highest energies, above ~ 5 eV, the reaction cross sections decline precipitously due to product dissociation.

For reaction with HD, the intramolecular isotope branching ratio oscillates between favoring production of OH^+ at low energies to favoring OD^+ between 1.50 and 9.0 eV and then back to OH^+ at energies above 9.0 eV. Comparison with phase space theory calculations demonstrates that some of this behavior is again due to

angular momentum considerations. Orientational and dynamical effects are used to rationalize the remaining energetic behavior.

2.6 APPENDIX: Conservation of Orbital Angular Momentum

At low kinetic energies, the probability of reaction is given by the Langevin criterion, such that the maximum impact parameter which can lead to products is determined in the entrance channel. The result, taken from equation (2.4), is given by

$$b_{LGS}^2 = e(2\alpha/E)^{1/2}. \tag{2.A1}$$

The argument in the text notes that at higher energies, conservation of angular momentum can reduce the cross section below this limit. This will now be proven in a more quantitative fashion. For simplicity, it is useful to note that the rotational angular momentum of the reactants, J, is much less than the orbital angular momentum, L, for all but the lowest energies. In addition, rotational excitation of the products is ignored such that L = L' (primes refer to product quantities). This latter equality can be expanded by using the equation

$$L = \mu v b = (2\mu E)^{1/2} b \tag{2.A2}$$

where μ is the reduced mass, v is the relative velocity, E is the relative energy, and b is the impact parameter. A similar equation is obtained for the products. These two equations can be combined and rearranged to yield

$$b^2 = b'^2(\mu' E'/\mu E). \tag{2.A3}$$

If the Langevin criterion is applied in the exit channel, then $b'_{LGS}{}^2 = e(2\alpha'/E')^{1/2}$. Substitution of this expression into equation (2.A3) yields

$$b_{max}{}^2 = e(2\alpha'E')^{1/2}(\mu'/\mu E). \tag{2.A4}$$

If the limit on b established by equation (2.A4) is less than the limit of equation (2.A1), the cross section, $\sigma = \pi b_{max}{}^2$, will drop below the Langevin prediction.

Experimental circumstances when these considerations will be important can be seen most easily by examining equation (2.A3). For endothermic reactions, $E' < E$ such that the limit in equation (2.A4) is clearly important if $\mu' < \mu$. (This has been pointed out previously.[37]) For an exothermic reaction, E' can always exceed E. Therefore, if $\mu' > \mu$, the cross section is always limited by the Langevin criterion, equation (2.A1). However, if $\mu' < \mu$, this limit applies only at the lowest energies and the cross section limit in equation (2.A4) applies at higher energies. This last situation occurs in the present case of reaction (2.1), where $\mu' = 0.95$ amu is about half $\mu = 1.79$ amu. The maximum allowable value of E' is $E - \Delta H$ where ΔH is the heat of reaction, -0.54 eV. When E is below 0.5 eV, E' can exceed E by over a factor of two such that $\mu'E'/\mu E > 1$. In such circumstances, b is limited by the Langevin criterion and the cross section is given by equation (2.4). For $E > 0.5$ eV, $\mu'E'/\mu E < 1$ such that the maximum value of b is determined in the exit channel, equation (2.A4). The energy at which these limits are the same ($b_{LGS} = b_{max}$) is given by

$$E_c = E'(\alpha'\mu'^2/\alpha\mu^2) \tag{2.A5}$$

For reaction (2.1), equation (2.A5) yields $E_c = 0.24\ E'$. For $E' = E'_{max} = E - \Delta H$, E_c is found to be 0.17 eV. This is, in fact, the energy at which the PST cross section first deviates from σ_{LGS}, Figure 2-6. The effects of rotational excitation of the products (non-zero J') may change this argument quantitatively but the qualitative predictions should be ubiquitous. Indeed, Grice *et al.*[38] have noted this effect in a very different system.

If the same argument is applied to reaction (2.3), a different value of E_c is found for channels (2.3a) and (2.3b). This angular momentum restriction occurs at a low energy for formation of OD^+, $E_c = 0.12$ eV, since μ'/μ (= 0.95/2.54 = 0.37) is smaller than μ'/μ (= 0.53) for reaction (2.1). For formation of OH^+, E_c is higher, 0.43 eV, since μ'/μ (= 1.80/2.54 = 0.71) is larger than this ratio for reaction (2.1). This leads to the increasing preference for formation of OH^+ as the energy is raised from thermal energies, Figure 2-4.

2.7 REFERENCES

1. Reaction enthalpies correspond to T = 0 K and are based on $\Delta_f H[OH^+(^3\Sigma^-)]$ = 309.0 kcal mol^{-1} [K. E. McCulloh, Int. J. Mass. Spectrom. Ion Phys. **21**, 333 (1976)] and tabulated heats of formation [M. W. Chase, Jr., C. A. Davies, J. R. Downey, Jr., D. J. Frurip, R. A. McDonald, and A. N. Syverud, J. Phys. Chem. Ref. Data **14**, Supp. 1 (1985)]. Enthalpies are corrected for differences in zero point energies between H_2, HD, and D_2, and OH^+ and OD^+ using known spectroscopic constants [K. P. Huber and G. Herzberg, Constants of Diatomic Molecules (Van Nostrand Reinhold, New York, 1979)].
2. K. T. Gillen, B. H. Mahan, and J. S. Winn, J. Chem. Phys. **58**, 5373 (1973).
3. K. T. Gillen, B. H. Mahan, and J. S. Winn, Chem. Phys. Lett. **22**, 344 (1973).
4. K. T. Gillen, B. H. Mahan, and J. S. Winn, J. Chem. Phys. **59**, 6380 (1973).
5. H. H. Harris and J. J. Leventhal, J. Chem. Phys. **58**, 2333 (1973).
6. H. H. Harris and J. J. Leventhal, J. Chem. Phys. **64**, 3185 (1976).
7. F. C. Fehsenfeld, A. L. Schmeltekopf, and E. E. Ferguson, J. Chem. Phys. **46**, 2802 (1967).
8. J. K. Kim, L. P. Theard, and W. T. Huntress, Jr., J. Chem. Phys. **62**, 45 (1975).
9. D. Smith, N. G. Adams, and T. M. Miller, J. Chem. Phys. **69**, 308 (1978).
10. W. Federer, H. Villinger, F. Howorka, W. Lindinger, P. Tosi, D. Bassi, and E. Ferguson, Phys. Rev. Lett. **52**, 2084 (1984).

11. J. D. Burley, K. M. Ervin, and P. B. Armentrout, J. Chem. Phys. **86**, 1944 (1987), and references therein.

12. K. M. Ervin and P. B. Armentrout, J. Chem. Phys. **83**, 166 (1985), and references therein.

13. G. Gioumousis and D. P. Stevenson, J. Chem. Phys. **29**, 294 (1958).

14. J. O. Hirschfelder, C. R. Curtiss, and R. B. Bird, Molecular Theory of Gases and Liquids (John Wiley and Sons, New York, 1954), p. 947.

15. M. Henchman, in Ion-Molecule Reactions, edited by J. L. Franklin (Plenum, New York, 1972), Vol. 1, pp. 101-259.

16. G. Chambaud, Ph. Millie, and B. Levy, J. Phys. B: Atom. Molec. Phys. **11**, L211 (1978).

17. M. Gerard-Ain, J. Phys. B: Atom. Molec. Phys. **13**, L131 (1980).

18. F. O. Ellison and M. L. McCandlish, J. Phys. B: Atom. Molec. Phys. **15**, L229 (1982). These authors calculate a barrier of approximately 1 eV for a collinear approach of reactants.

19. D. M. Hirst, J. Phys. B: Atom. Molec. Phys. **17**, L505 (1984).

20. F. Fiquet-Fayard and P. M. Guyon, Mol. Phys. **11**, 17 (1966).

21. J. C. Leclerc, J. A. Horsley, and J. C. Lorquet, Chem. Phys. **4**, 337 (1974).

22. A. J. Lorquet and J. C. Lorquet, Chem. Phys. **4**, 353 (1974).

23. J. A. Smith, P. Jorgensen, and Y. Ohrn, J. Chem. Phys. **62**, 1285 (1975).

24. H. M. Rosenstock, K. Draxl, B. W. Steiner, and J. T. Herron, J. Phys. Chem. Ref. Data **6**, Suppl. 1 (1977).

25. J. D. Poll and L. Wolniewicz, J. Chem. Phys. **68**, 3053 (1978).

26. T. Su and M. T. Bowers, Int. J. Mass Spectrom. Ion Phys. **17**, 309 (1976).

27. K. M. Ervin and P. B. Armentrout, J. Chem. Phys. **86**, 2659 (1987).

28. K. M. Ervin and P. B. Armentrout, J. Chem. Phys. **84**, 6738 (1986).

29. W. J. Chesnavich and M. T. Bowers, J. Chem. Phys. **68**, 901 (1978).

30. M. E. Weber, J. L. Elkind, and P. B. Armentrout, J. Chem. Phys. **84**, 1521 (1986).

31. The best fit between the present cross section data and the fall-off model presented in reference 30 corresponds to D = 6.25 eV, f = 1.0, and p = 2.0.

32. A. Henglein and K. Lacmann, Adv. Mass Spectrom. **3**, 331 (1966); A. Henglein, in Ion - Molecule Reactions in the Gas Phase, edited by P. J. Ausloos (American Chemical Society, Washington, D.C., 1966), p. 63; A. Ding, K. Lacmann, and A. Henglein, Ber. Bunsenges. Phys. Chem. **71**, 596 (1967).

33. T. F. George and R. J. Suplinskas, J. Chem. Phys. **54**, 1046 (1971).

34. J. C. Light and S. Chan, J. Chem. Phys. **51**, 1008 (1969).

35. P. M. Hierl, J. Chem. Phys. **67**, 4665 (1977).

36. This effect has been discussed previously for the example of Kr^+ reacting with HD by S. Chivalak and P. M. Hierl, J. Chem. Phys. **67**, 4654 (1977).

37. J. L. Elkind and P. B. Armentrout, J. Phys. Chem. **89**, 5626 (1985).

38. M. E. Grice, K. Song, and W. J. Chesnavich, J. Phys. Chem. **90**, 3503 (1986).

TABLE 2-I

Thermal rate constants for reaction (2.1)

technique[a]	rate constant[b]	reference
GIB	1.67 ± 0.3	this work
FA	2.0 ± 0.6	7
ICR	1.58 ± 0.2	8[c]
ICR	1.32 ± 0.2	8[d]
SIFT	1.7 ± 0.3	9
SIFT	1.2 ± 0.4	10
LGS	1.56	
AQO	1.61	

[a]GIB - guided ion beam; FA - flowing afterglow; ICR - ion cyclotron resonance; SIFT - selected ion flow tube; LGS - Langevin-Gioumousis-Stevenson model, equation (2.8); AQO - average quadrupole orientation model.

[b]In units of 10^{-9} cm^3 s^{-1}; measured at ~ 300 K.

[c]CO_2 used as a source gas for O^+.

[d]O_2 used as a source gas for O^+. This yields about 30% excited states.

TABLE 2-II

Critical energies (eV) for product dissociation

Reaction	thermodynamic[a]	data[b]	E_S[c]
(2.1)	4.48	6.25	8.6
(2.2)	4.56	6.25	8.3
(2.3a)	4.51	6.85	12.3
(2.3b)	4.51	5.65	6.5

[a]Thermodynamic threshold for dissociation of ground state ionic product.

[b]Dissociation energy obtained from empirical fit of cross section data, see text.

[c]Critical spectator stripping energy for formation of ground state ($^3\Sigma^-$) ionic product according to equation (2.12).

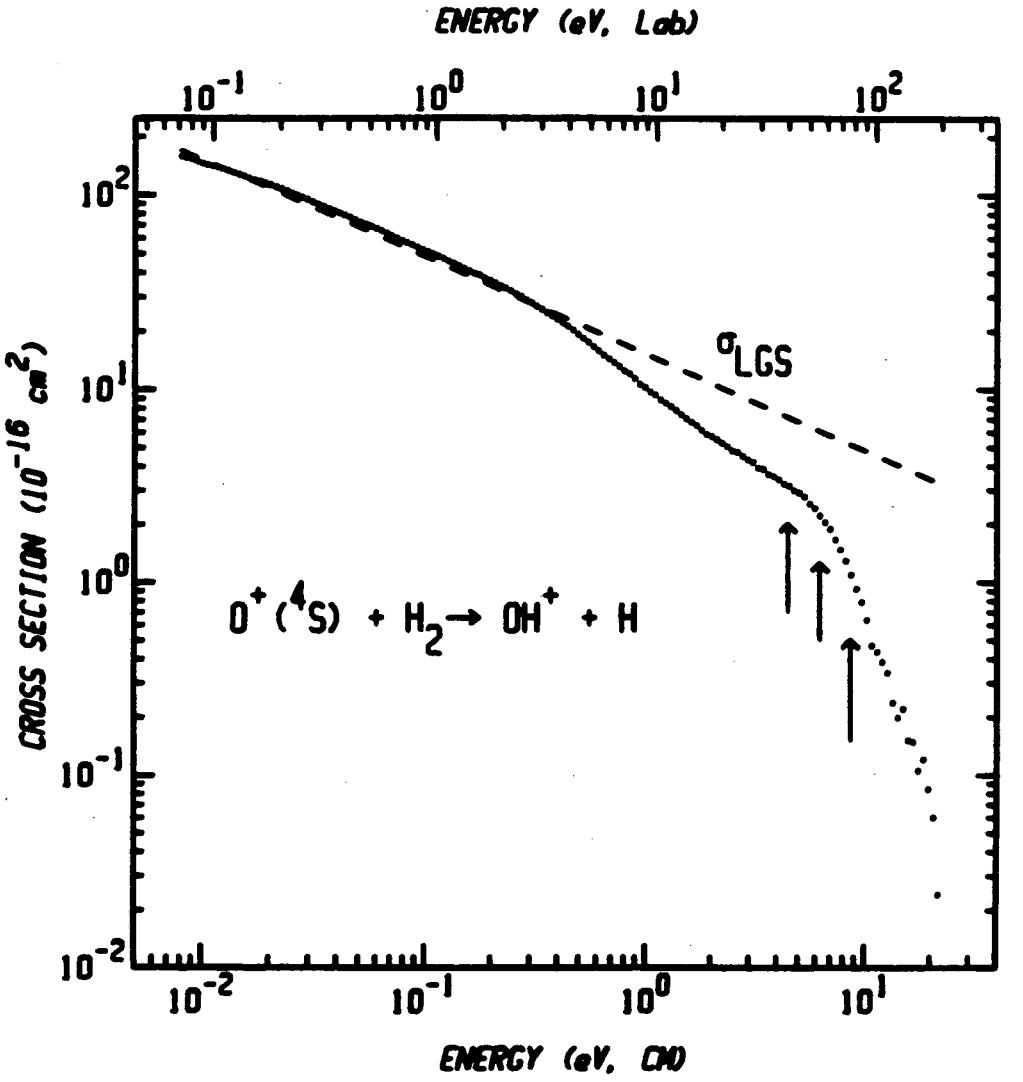

Figure 2-1. Cross sections for reaction (2.1) as a function of relative translational energy (lower scale) and laboratory energy (upper scale). The present data are denoted by points. The LGS cross section is given by the dashed line. Arrows indicate the thermodynamic onset for dissociation of OH^+ (4.48 eV), the empirically determined dissociation energy (6.25 eV), and the critical spectator stripping energy, E_s (8.59 eV).

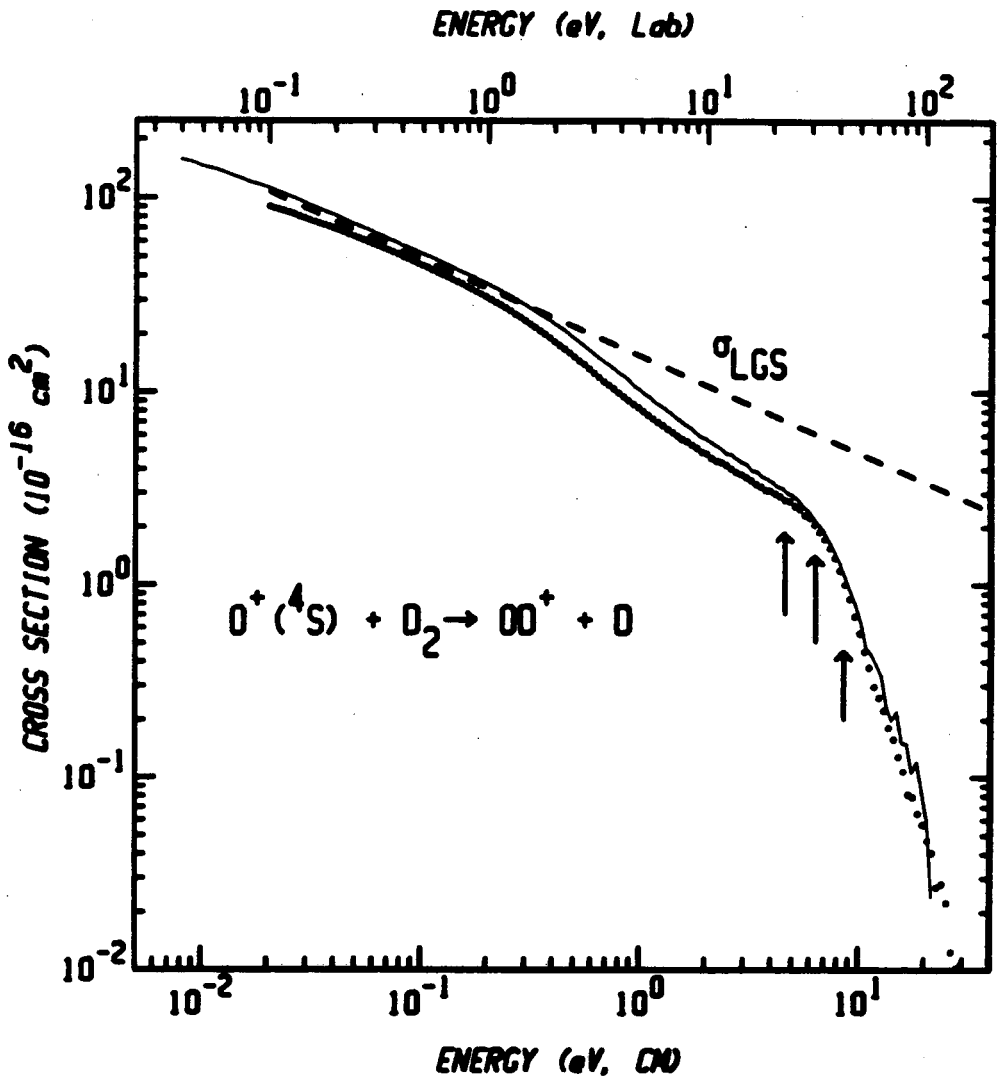

Figure 2-2. Cross sections for reaction (2.2) as a function of relative translational energy (lower scale) and laboratory energy (upper scale). The present data are denoted by points. The LGS cross section is given by the dashed line, and the solid curve reproduces the data for reaction (1) for comparison. Arrows indicate the thermodynamic onset for dissociation of OD^+ (4.56 eV), the empirically determined dissociation energy (6.25 eV), and the critical spectator stripping energy, E_s (8.33 eV).

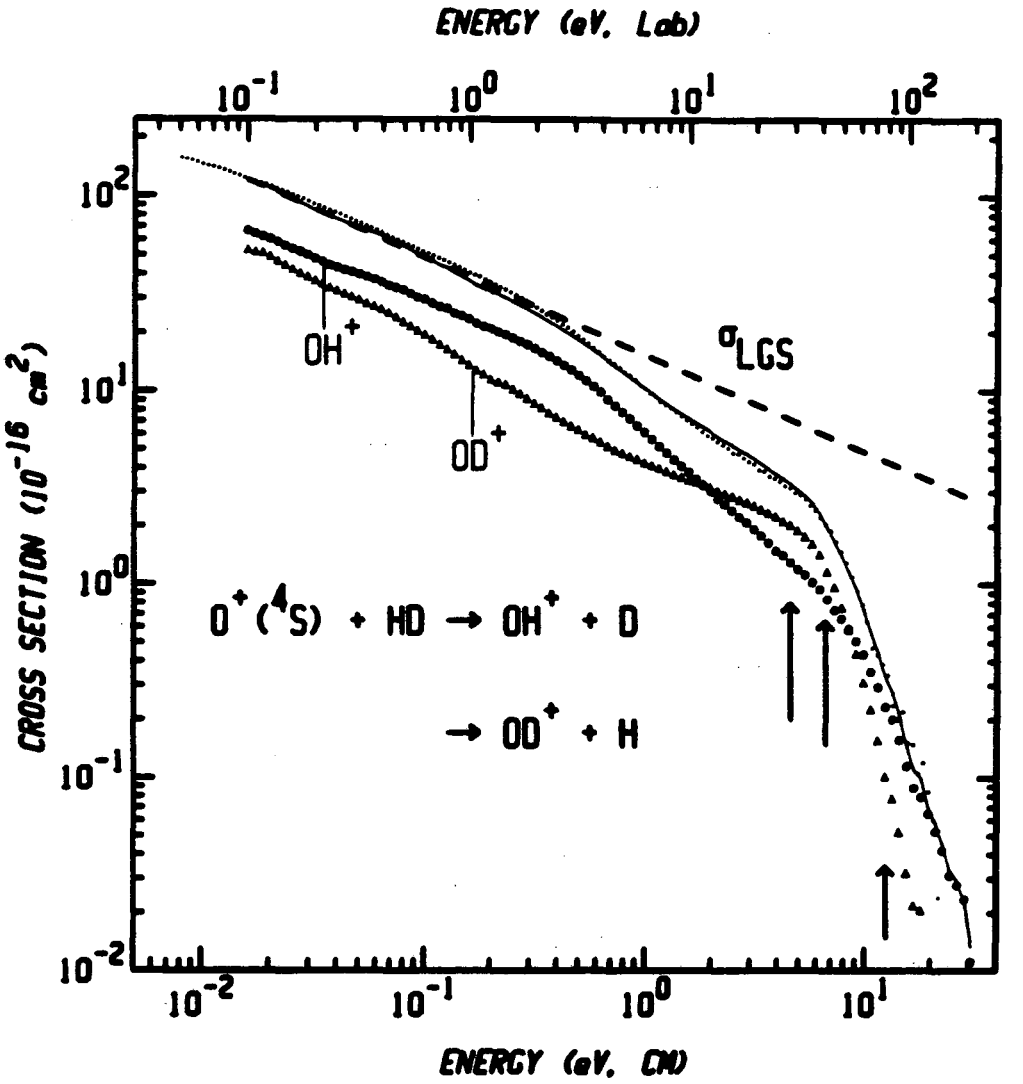

Figure 2-3. Cross sections for reaction (2.3) as a function of relative translational energy (lower scale) and laboratory energy (upper scale). The filled circles show the cross section for reaction (2.3a), the open triangles show the cross section for reaction (2.3b), and the solid line indicates their sum. The LGS cross section is given by the dashed line, and the dotted line reproduces the data for reaction (2.1) for comparison. Arrows indicate the thermodynamic onset for dissociation of HD (4.51 eV), and the critical spectator stripping energies for OD^+ (6.5 eV) and OH^+ (12.3 eV).

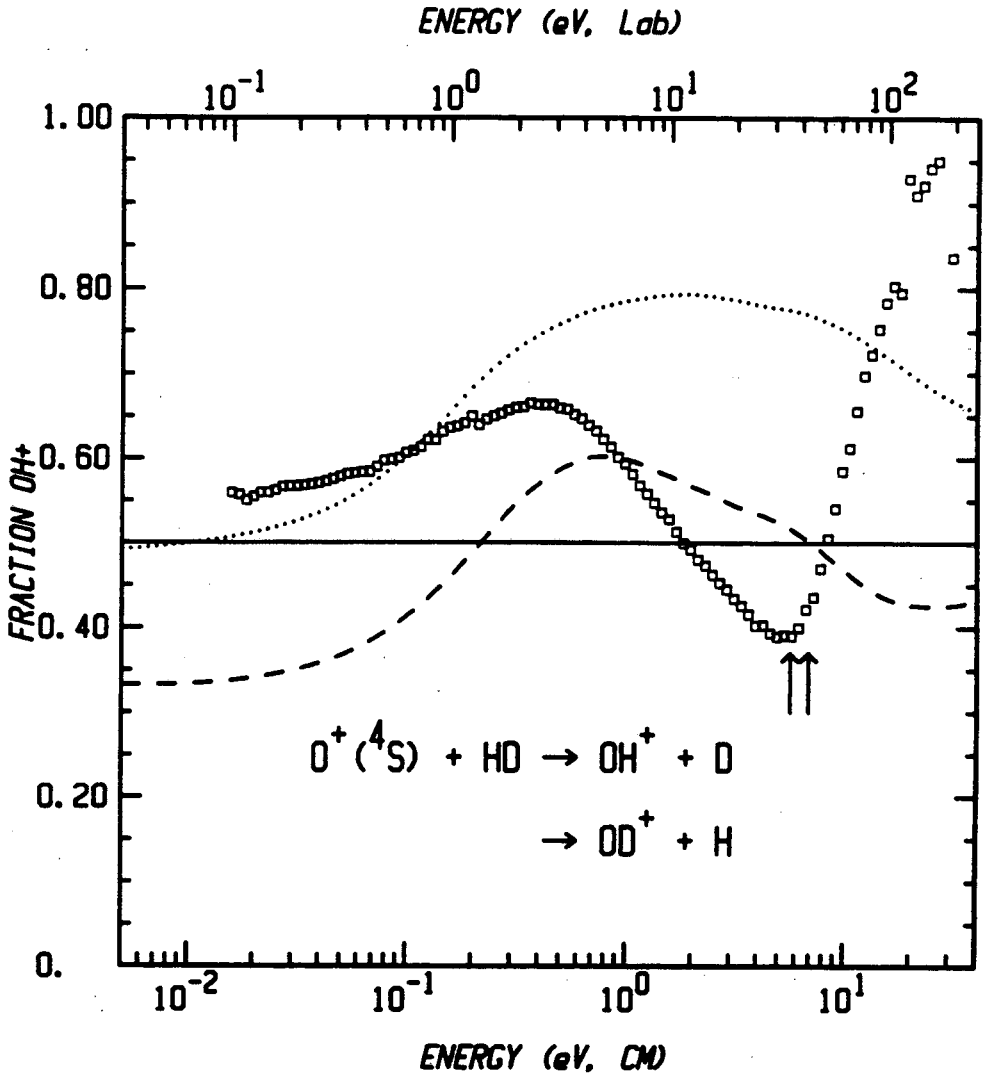

Figure 2-4. Isotopic branching ratio for reaction (2.3) presented in terms of the fraction of OH^+ produced. The ratio is plotted as a function of the relative translational energy (lower scale) and the laboratory energy (upper scale). Experimental results are denoted by the open squares, and the phase space theory prediction is given by the dashed line. The dotted line gives the phase space theory prediction when OH^+ and OD^+ are arbitrarily forced to have the same rotational and vibrational constants. Arrows at 5.65 and 6.85 eV designate the empirically determined dissociation energies for OD^+ and OH^+, respectively.

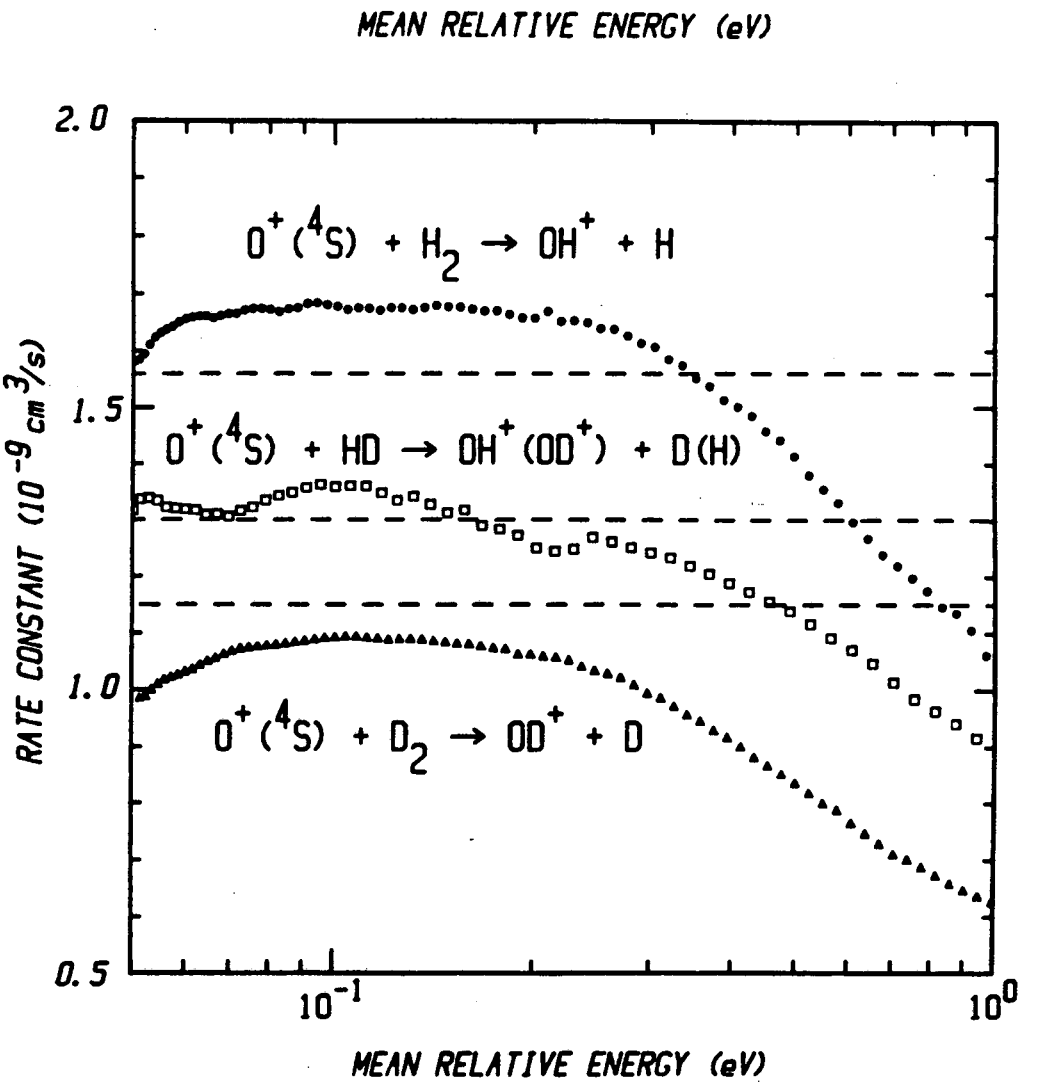

Figure 2-5. Phenomenological rate constants for reactions (2.1) - (2.3) as a function of the mean relative energy of the reactants. The filled circles, filled triangles, and open squares correspond to the data for reactions (2.1), (2.2), and (2.3), respectively, and are derived from the cross section data in Figures 2-1 through 2-3 via the use of equation (2.7). The LGS-predicted rate constants (equation (2.8)) for reactions (2.1), (2.2), and (2.3) are given by the upper, lower, and middle dashed lines, respectively.

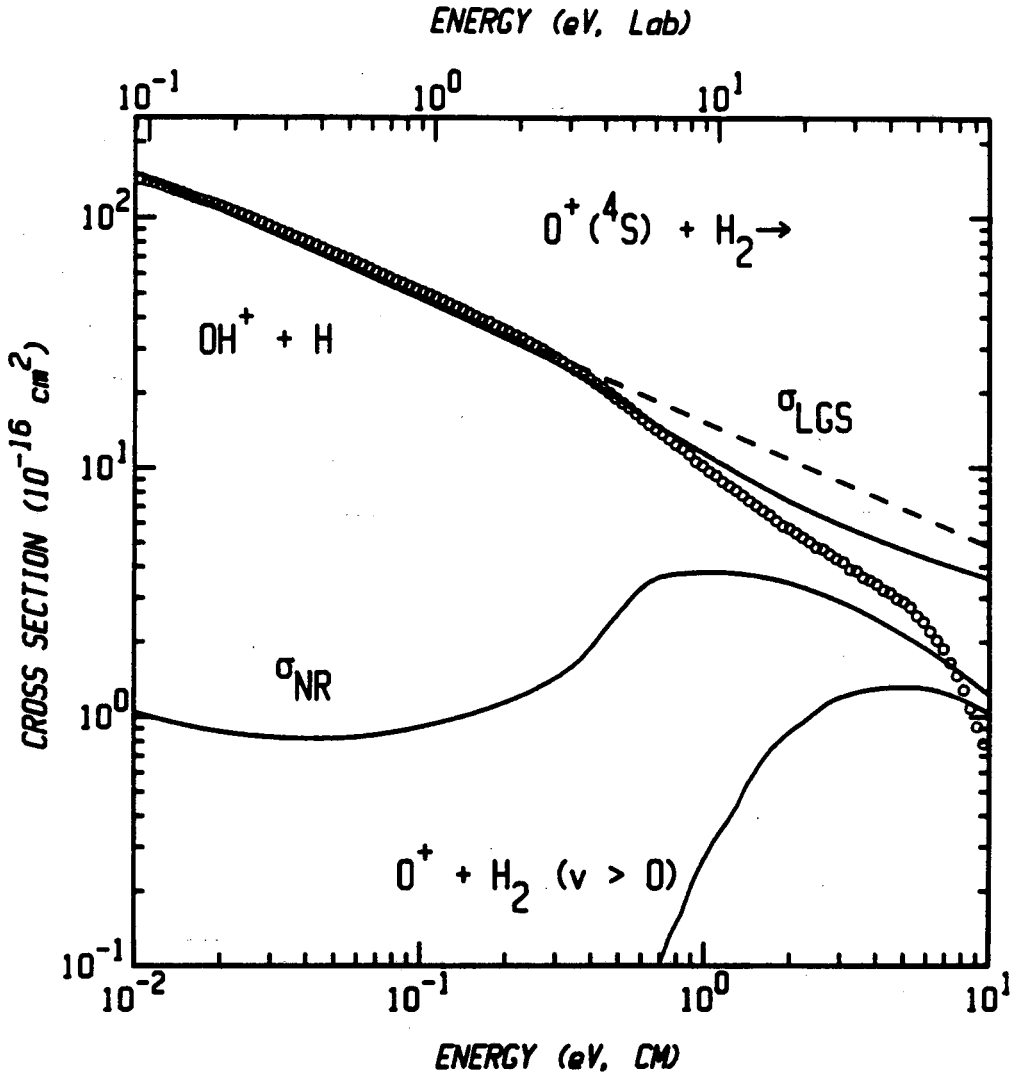

Figure 2-6. Phase space theory calculations of the reactive and nonreactive cross sections for reaction (2.1) as a function of relative translational energy (lower scale) and laboratory energy (upper scale). The lower, intermediate, and upper solid lines correspond to the PST cross section for vibrational excitation of the H_2 target molecule, the total PST cross section for no reaction (σ_{NR}, $v(H_2) \geq 0$), and the PST cross section for reaction (2.1), respectively. The present data are denoted by the open circles, and the LGS cross section is designated by the dashed line.

Chapter Three

Kinetic Energy Dependence of $O^+(^4S) + N_2$

3.1 INTRODUCTION

It was long thought that exothermic ion - molecule reactions proceed efficiently with cross sections that decline as predicted by the Langevin-Gioumousis-Stevenson (LGS) model.[1] One system which was found to contradict this predicted behavior is reaction (3.1), exothermic by 1.08 eV. This process,

$$O^+(^4S) + N_2(X^1\Sigma_g^+) \rightarrow NO^+(X^1\Sigma^+) + N(^4S), \qquad (3.1)$$

is extremely important in understanding the chemistry of the upper atmosphere and its atypical energy dependence is also of fundamental interest. For these reasons, reaction (3.1) is one of the better studied ion - molecule reactions. Ion beam,[2-10] flow/drift tube (FD),[11-14] selected ion flow tube (SIFT),[15,16] and flowing afterglow (FA) studies[17-23] have yielded information on the behavior of this reaction from thermal energies to over 20 eV.

While the collective energy range of these experiments is broad, the ability of any one study to examine the kinetic energy dependence over a wide range has been limited. Typically, ion beam studies have been useful for examining relatively high energy regimes but have been unable to generate reliable data below ~ 1 eV. FA methods provide access to the lowest energy regions, but are incapable of going much above 600 K ($3k_BT/2$ = 0.078 eV). Recent FD results bridge the gap between ion beam and FA studies, but do not extend to more than 3 eV. Unfortunately, the ion

energy distributions in FD methods are relatively broad and uncertain at energies above a few tenths of an electron volt. Despite this, a very careful and detailed analysis of the FD results has provided the cross section for reaction (3.1) over a two order of magnitude energy range.[13] The cross section obtained from this analysis disagrees somewhat with the results of beam studies above 1 eV but reproduces the rate constant behavior in both He and Ar buffers.[13] Overall, the consensus of all these studies is that the behavior of reaction (3.1) shows an inefficient channel at very low energies, < 0.2 eV, followed by a sharp increase in the cross section at higher energies.

To understand this behavior, theoretical work involving the use of potential energy surface correlation diagrams[24-32] and phase space calculations[33] has been carried out. These studies conclude that the failure of reaction (3.1) to proceed efficiently is due to a barrier on the surface which adiabatically correlates ground state reactants and products. In $C_{\infty v}$ symmetry, this is a $^4\Sigma^-$ surface which corresponds to an excited state of N_2O^+. If the angle of approach is altered, the barrier on this surface (now $1^4A''$) is lower with a calculated minimum of 0.15 ± 0.1 eV at a NNO angle of 126°.[28] This surface is shown schematically in Figure 3-1. At the lowest kinetic energies, reaction can only occur via a spin-forbidden transition between this $N_2O^+(1^4A'')$ surface and the $N_2O^+(1^2A'')$ surface. Hopper[28] has proposed two possible mechanisms for this low energy process: either the collisionally stabilized multistep reaction,

$$O^+(^4S) + N_2 + M \rightarrow N_2\text{-}O^+(1^4A'') + M \quad (3.2a)$$

$$N_2\text{-}O^+(1^4A'') \rightarrow N_2O^+(1^2A'') \quad (3.2b)$$

$$N_2O^+(1^2A'') \rightarrow NO^+ + N, \quad (3.2c)$$

or the single collision reaction,

$$O^+(^4S) + N_2 \rightarrow N_2O^+(1^2A'') \rightarrow NO^+ + N. \quad (3.3)$$

Hopper has argued that process (3.2) is the primary mechanism for reaction (3.1) at low energies and that process (3.3) is unimportant until energies below 0.001 eV. The rationale behind this assumption is that collisional stabilization of the $N_2O^+(1^4A'')$ intermediate in step (3.2a) enhances step (3.2b) by allowing for multiple "passes" of the N_2O^+ system through the intersection of the $1^4A''$ and $1^2A''$ surfaces. This proposal has not been subjected to an experimental test since all studies of reaction (3.1) at low energies[11-23] have been performed in flow tubes where a rare gas buffer is available as the third body in step (3.2a).

In the present chapter, guided ion beam mass spectrometry is used to investigate the kinetic energy dependence of reaction (3.1) from 0.03 to 30.0 eV. The results are compared to those discussed in the literature,[2-23] and the observed behavior is interpreted in light of the theoretical calculations.[27-32] Several points are of particular interest. Can the guided ion beam technique provide accurate information at the very low kinetic energies previously available to only flowing afterglow and flow/drift methods? If so, is the cross section derived from FD rate constant data accurate? Since the beam technique is performed without the presence of a buffer gas, which mechanism, (3.2) or (3.3), is dominant at the lowest kinetic energies?

3.2 RESULTS

3.2.1 Charge Transfer Reaction

The cross section for the charge transfer reaction

$$O^+(^4S) + N_2(X^1\Sigma_g^+) \rightarrow N_2^+ + O \tag{3.4}$$

is shown in Figure 3-2. The cross section exhibits an onset near the thermodynamic threshold of 1.96 eV for production of ground state $N_2^+(X^2\Sigma_g^+)$ and then rises in an interesting, double-humped fashion to give an early plateau and a secondary threshold near 6 eV. This second feature may be due to formation of $N_2^+(B^2\Sigma_u^+)$, which lies 3.2 eV above the ground state, and thus has a threshold at 5.2 eV. Finally, the cross section reaches a sharp maximum at about 10 eV before declining rapidly. This peak appears to correspond to dissociation of the N_2^+ product, which can begin at 10.7 eV.[34] However, the absolute cross section for the charge transfer process may not be completely reliable, especially at higher energies, because of inefficient collection of the N_2^+ product. Charge transfer products are susceptible to losses since they can be formed with little forward velocity in the laboratory frame.

The overall magnitude of the present result is in good agreement with the phase space calculations of Wolf,[33] Figure 3-2. The shape of the predicted cross section does not contain the sharp secondary threshold observed here but does show a decline beginning at about 10 eV. This decrease in the cross section prevents the present data from extrapolating smoothly to the results of Moran and Wilcox,[35] who measured a slowly increasing cross section of $\sim$ 1 Å^2 at laboratory energies above 500 eV, $E_0 > 318$ eV. This may simply be due to the differing energy regions

examined but may also be caused by the inefficient collection mentioned above. In another study, Ottinger and Simonis[36] observed emission from $N_2^+(B^2\Sigma_u^+)$ product at a laboratory energy of 1,000 eV, E_0 = 636 eV. The cross section measured for this process was 0.046 Å^2. Again, no direct comparison with the present results can be made.

3.2.2 Nitrogen Atom Abstraction: Cross Sections

At interaction energies below 0.25 eV, the cross section for reaction (3.1) decreases as the energy is increased. The energy dependence of the decline is similar to the $E^{-0.5}$ dependence predicted by the LGS model, equation (2.4). The magnitude of the measured cross section, however, is approximately 400 times less than that predicted by equation (2.4). Between 0.25 and 2.0 eV, the cross section rises rapidly with increasing energy. At energies above 2.0 eV, the cross section rises more gently until a maximum of ~ 4.0 Å^2 is observed near 8 eV. Shortly after this maximum, dissociation of the NO^+ product to $O^+(^4S)$ and $N(^4S)$ becomes energetically possible. The overall process,

$$O^+ + N_2 \rightarrow O^+ + N + N, \qquad (3.5)$$

has a thermodynamic threshold equal to $D^o(N_2)$ = 9.76 eV.[34]

Also shown in Figure 3-2 are the cross section results from Rutherford and Vroom.[5] Agreement between the two sets of data is excellent. Similar agreement is noted with an earlier experiment of Giese,[2] although his rather scattered data are not plotted here. Results of Stebbings, Turner, and Rutherford[10] also show approximate

agreement with the current report, but cannot be compared directly because of a significant presence of excited state O^+ in their ion beam.

One interpretation of previous beam studies which deserves comment concerns the spectator stripping model (SSM).[37] Both the merged beam results of Neynaber and Magnuson[8] and the kinetic energy measurements of Leventhal[4] indicate that the peak velocity of the NO^+ product in reaction (3.1) can be adequately represented by the SSM for the energy range $2 \leq E_0 \leq 12$ eV. However, the SSM (equation 2.12) also predicts that the NO^+ product becomes unstable with respect to dissociation at a kinetic energy of 13.3 eV (this energy is marked by an arrow in Figure 3-2). Clearly, the decline in the cross section for NO^+ correlates not with E_s but with the thermodynamic threshold at 9.8 eV. This shows that the *distribution* of product internal energies (and therefore, product kinetic energies as well) is not adequately described by the simplistic and physically unrealistic SSM.

3.2.3 Nitrogen Atom Abstraction: Rate Constants

It is of interest to compare directly the present cross section results with those of FA and FD experiments which measure reaction rates. To do this, the cross sections are converted into phenomenological rate constants using equation (2.7). Rate constants derived in this manner can be directly compared to those measured in FA and FD experiments once the differences in the ion energy distributions are taken into account.

Figure 3-3 presents the phenomenological rate constant $k(\langle E \rangle)$ for reaction (3.1), as calculated by equation (2.7). Also shown in Figure 3-3 are the FA results of

Ferguson *et al.*,[19] and the FD measurements of Albritton *et al.*[13] and Johnsen and Biondi.[11] Considering the very different methods used to obtain these results and the slowness of the reaction, the qualitative agreement is rather good. The general energy dependence is comparable and the absolute magnitudes of the rate constants are within a factor of 5 at all energies. Nevertheless, the quantitative comparison is somewhat disappointing since the observed differences lie outside the combined range of experimental error for the ion beam ($\pm 20\%$) and FD or FA experiments ($\pm 30\%$).

Several possible explanations of why the present rate constants are higher at low energies can be readily discounted. As noted above, the relative uncertainty of the measured cross sections (and rate constants) is less than 20% even at the lowest point. The absolute magnitudes shown here were reproduced several times during the course of several months of experimentation. The *maximum* contribution from excited state O^+ is calculated to be a factor of 5 less than the lowest cross section (or rate constant) measured. The possibility that the energy of the ions is influenced by the rf power driving the octopole was found to be negligible. The shape of the cross section did not change with octopole power and the magnitudes were reproducible within 20% at all kinetic energies. Cross sections are independent of N_2 pressure throughout the energy range examined as expected for a single bimolecular event. The inability of these factors to account for the disagreements between the present data and the FD and FA data strongly suggests that the differences are caused by differences in the ion energy distributions. These differences are discussed in detail below.

3.3 DISCUSSION

While the experimentally measured cross sections and rate constants are reasonable approximations to the true cross sections and rate constants, the experimental conditions broaden sharp features in their behavior as a function of kinetic energy. In this section, the manner in which the distribution of ion kinetic energies and the random thermal motion of the reactant gas obscure the true cross section is examined. It is not possible to determine a unique form for the true cross section by directly deconvoluting the energy-broadened experimental results.[38] An indirect method is therefore used in which a particular model for the true cross section is convoluted over the experimental distributions of ion and neutral energies.[38,39] The convoluted form of the trial cross section is then compared directly to the experimentally observed cross section. Finally, the parameters of the trial function are adjusted to obtain the best possible fit to the actual data.

The simplest cross section model (which will be referred to as I) is completely empirical and uses the equation

$$\sigma(E) = \sigma_1 E^{-u} + \sigma_2(1-E_T/E)^w, \tag{3.6}$$

where σ_1, u, σ_2, E_T, and w are adjustable parameters. E is the *true* interaction energy between the reactants and differs from the energies E_0 and $<E>$ which are average values for particular experimental distributions of energies. The first term in equation (3.6) accounts for the exothermic behavior at low energies and the second term accounts for the endothermic behavior at high energies. The specific form of equation (3.6) which is found to best represent the data corresponds to σ_1 = (0.036 ±

0.010) $Å^2$ eV^u, u = 0.53 ± 0.10, σ_2 = (4.4 ± 0.2) $Å^2$, E_T = 0.40 ± 0.10 eV, and w = 2.8 ± 0.8. As shown in Figure 3-4, convolution of this model over the experimental distribution of energies yields a result which is in excellent agreement with the present data at all energies. Also shown in Figure 3-4 is a model for the decline in the cross section at energies above 9.76 eV. This model is described in detail in a previous report.[40,41]

A somewhat more sophisticated model, II, can be developed by incorporating Landau-Zener theory[42,43] to calculate the probability of a transition from the $1^4A''$ surface to the $1^2A''$ surface during the course of a collision. This probability[42-44] is

$$P = 2p(1 - p), \tag{3.7}$$

where

$$p = \exp[-(A/E_C)^{1/2}] \tag{3.8}$$

is the probability of staying on the $1^4A''$ surface upon a single passage of the N_2O^+ system through the $1^4A''$ - $1^2A''$ intersection, A is the coupling strength between the two surfaces, and E_C is the relative kinetic energy at the intersection. Multiplication of the LGS collision cross section, σ_{LGS} as given by equation (2.4), by P gives the Landau-Zener cross section for reaction (3.1) at energies below E_T. In the limit of small p, equation (3.7) and equation (3.8) simplify to $P = 2(A/E_C)^{1/2}$ such that

$$\sigma(E) = 2\sigma_{LGS}(A/E_C)^{1/2}, \quad E < E_T. \tag{3.9}$$

The overall form of the expression for the cross section is now

$$\sigma(E) = 2\sigma_{LGS}(A/E_C)^{1/2} + \sigma_2(1-E_T/E)^w, \tag{3.10}$$

where the second term is unchanged from equation (3.6). This expression contains two new parameters, A and E_C. In the absence of any information regarding these quantities, a simple treatment assumes that $E_C = E$ and treats A as an adjustable parameter. The best fit between this model and the data is obtained when $A = 1.3 \times 10^{-8}$ eV, $\sigma_2 = (4.5 \pm 0.2)$ Å^2, $E_T = 0.28 \pm 0.05$ eV, and $w = 4.3 \pm 0.9$. The unconvoluted form of this model has an E^{-1} energy dependence, which is appreciably steeper than the $E^{-0.53}$ dependence of the first model. Because of this, the convoluted form of the second model reaches a considerably smaller minimum that skirts the lower edge of the data in the region before threshold, Figure 3-4.

A third model, III, uses equation (3.10) in conjunction with Hopper's calculated result[28] that the crossing between the $1^4A''$ and $1^2A''$ surfaces occurs at an energy 0.10 eV below that of the separated O^+ and N_2 reactants. Now, $E_C = E + 0.10$ eV and the energy dependence of the first term in equation (3.10) is intermediate to that of the first two models. The best fit to the data is obtained when $A = 8.3 \times 10^{-8}$ eV, $\sigma_2 = (4.5 \pm 0.2)$ Å^2, $E_T = 0.30 \pm 0.06$ eV, and $w = 4.0 \pm 0.7$, Figure 3-4.

The average value of E_T from all three models is 0.33 ± 0.08 eV. This lies within the 0.2 - 0.5 eV estimate of the "effective" adiabatic barrier calculated by Hopper.[32] Furthermore, the relative behavior of the present results compares favorably with Hopper's semiclassical trajectory calculations[32] using $E_T = 0.25$ and 0.99 eV, Figure 3-5. This lends support to Hopper's conclusions concerning the topology of the $1^4A''$ hypersurface.

In contrast, the current results cannot be interpreted with the main mechanism hypothesized by Hopper[28] for energies below the adiabatic threshold, mechanism (3.2). In the first step of this mechanism, reaction (3.2a), a three body collisional stabilization occurs to trap N_2-$O^+(1^4A")$ in a shallow potential energy well due to the ion-induced dipole attraction, Figure 3-1. Given the improbability of secondary ion - molecule collisions within the interaction region of the apparatus, such a mechanism can be ruled out for the formation of NO^+ observed in this study. In addition, the ability of Landau-Zener theory[42-44] to account for the low energy cross section results confirms the feasibility of mechanism (3.3), the single collision, spin-forbidden process. This is particularly evident from a comparison of the values of A found here (10^{-7} - 10^{-8} eV) to the value of 2.7 x 10^{-5} eV estimated by Tully[45] for a similar system, the spin-forbidden unimolecular decomposition of nitrous oxide to $N_2(^1\Sigma_g^+)$ and $O(^3P)$. Since the values of A which fit the present data are smaller than this, it is clear that the present agreement with a Landau-Zener model does not require an unreasonably large coupling constant.

Also shown in Figure 3-5 is the cross section derived from the FD data of Albritton *et al.*.[13] This result was obtained using a procedure similar to that used here. Specifically, a trial cross section is convoluted with ion and neutral energy distributions and compared with FD rate constant data in both He and Ar buffers. The shape of the cross section is adjusted until both sets of data are reproduced. The difference between this procedure[13] and that of the present report is that in the latter case it is possible to measure the ion energy distribution directly, while this is

calculated[46,47] for the FD work. This calculation involves two steps. First, an ion-neutral interaction potential is derived from a series of ion mobility measurements.[48,49] Then, the derived potential is used to estimate the ion energy distribution corresponding to a particular set of experimental conditions. Figure 3-5 makes it clear that a substantial disagreement exists *at all energies* between the present results and the cross section derived from the FD data. This is despite the fact that the FD data and the present results converted to rate constants agree at elevated energies, Figure 3-3. In general, this demonstrates how very difficult it is to convert from a macroscopic rate constant to a microscopic cross section.

A qualitative understanding of the origins of the disagreement can be gleaned from an examination of the ion energy distributions associated with each experiment. In both the FD and the ion beam studies, the N_2 reactant has a thermal distribution of energies corresponding to the ambient temperature, ~ 300 K. In the present beam experiment, the incident $O^+(^4S)$ ions have a Gaussian energy distribution with a FWHM of 0.2 eV (0.3 eV lab). This energy distribution does not change with kinetic energy until truncation of the slow ions, which occurs at energies less than ~ 0.2 eV. In the FD (and FA) rate constant determinations, the presence of a high pressure buffer gas (He or Ar) insures that the ions maintain a Maxwellian distribution at low energies. In the FD experiments, the ions are accelerated through the buffer gas by a weak electric field. As the field strength increases, the distribution of ion energies begins to deviate from a Maxwellian distribution in a manner which depends on the detailed interactions of the ion with the buffer gas. Since accurate experimental deter-

minations of the true distribution of reactant energies have not yet proven possible, it is necessary to estimate (or calculate) the distributions as outlined above.[13]

Figure 3-6a compares the ion speed distributions for these experiments at an average laboratory energy of 0.64 eV (E_0 = 0.41 eV, $\langle E \rangle$ = 0.42 eV).[50] It can be seen that the distribution for the ion beam is by far the narrowest. Distributions in He and Ar buffers are similar to Maxwell-Boltzmann (MB), but the He distribution has fewer high speed ions than the Ar distribution. As one progresses from beam to He buffer to Ar buffer, there are more kinetically "hot" ions with speeds that correspond to larger cross sections. Thus, the apparent threshold for reaction (3.1) is lower in the Ar buffer than in the He buffer which in turn is lower than in the beam data which in turn is lower than the true threshold energy, $E_T \approx 0.3$ eV. This progression is easily seen in Figure 3-3.

The discrepancy between the "true" cross section obtained from the present data and the FD cross section above ~ 0.3 eV is now clear. In the threshold region, the FD cross section is smaller than the beam cross section while at higher energies the FD cross section is larger, Figure 3-5. These differences in cross section magnitude probably compensate for one another during the convolution over the FD ion energy distributions, which are quite broad at these energies. In contrast, the experimental energy distributions in the ion beam experiment are much narrower at elevated energies. This is clearly demonstrated by the fact that, above 0.7 eV, the measured and "true" cross sections do not differ appreciably, Figure 3-4.

The situation at low interaction energies is qualitatively different. This is shown in Figure 3-6b, which compares the ion beam speed distribution at a laboratory energy of 0.10 eV (E_0 = 0.064 eV, $\langle E \rangle$ = 0.078 eV) to a MB distribution having the same average energy, $3k_BT/2$ (T = 774 K). The MB distribution exactly reproduces the speed distribution in FA studies and is a reasonable approximation to the distribution found in FD experiments. At this energy, the FA and FD distributions are narrower and have a lower most-probable speed than the ion beam distribution. The high pressure conditions of the FA and FD experiments now serve to reduce the spread of the reactant energies compared to the static FWHM of the ion beam. Just as energy broadening in the FD experiment gave results which were high in the region near threshold, energy broadening in the beam experiment produces high results at low energies. One factor in particular plays an important role in this process. At low energies, slow ions are truncated from the ion beam distribution. This shifts the peak of the ion speed distribution towards zero and yields more ions with very low velocities than a MB distribution. Since ions with speeds near zero correspond to very large cross sections, this causes the ion beam method to give high cross section results at very low energies.

The effect can be seen both in Figure 3-5 and Figure 3-3. Figure 3-5 shows that convolution of the FD derived cross section[13] over the present experimental distribution of energies yields a result which is in agreement with the present data at the lowest energies. Figure 3-3 shows that model II (equation (3.10) with E_C = E) converts to a rate constant which matches the FA and FD data within experimental

uncertainties. Because this model is roughly consistent with all sets of data it is probably the best estimate of the true cross section over the energy range examined.

Unfortunately, differences in ion energy distributions do not appear to account for the disagreements observed immediately before the adiabatic threshold, from about 0.1 to 0.3 eV. This discrepancy is probably a reflection of the joint experimental uncertainties involved in measurements of very slow reactions at these energies; however, it is possible that some of the residual discrepancy results from differences in interaction region pressure. This is the other major difference in experimental conditions between the ion beam and the FA and FD studies besides the energy distributions. The differences between the present data and the FA and FD rate constant data imply that three-body collisional stabilization diminishes production of NO^+ at low interaction energies. However, Bohme *et al.*[23] have found the opposite effect and have shown that the reaction rate increases with increasing He buffer gas pressure at 82 K, $\langle E \rangle = 0.011$ eV. This study may not be definitive, however, since the rate constant was obtained by measuring the decline in the O^+ signal. In their detailed study of this system, Albritton *et al.*[13] concluded that erroneous rate constants are obtained for this reaction when measured in this manner. Further FD measurements on the quantitative three-body pressure dependence of reaction (3.1) at low energies would help to resolve this issue.

The observation that the reaction rate increases with increasing buffer gas pressure[23] supports Hopper's prediction[28] that collisional stabilization of N_2O^+ promotes reaction at low energies, reaction scheme (3.2). At the same time, both the

present results and Landau-Zener[42-44] theory indicate that reaction can occur via a single collision process, reaction scheme (3.3). Together, these observations imply that at low pressures reaction (3.1) proceeds via a single collision process, and at higher pressures, reaction may be enhanced via process (3.2). At energies above threshold, where the reactants are not required to undergo a spin-forbidden transition, this pressure dependence is not expected to play a major role.

3.4 CONCLUSION

Guided ion beam mass spectrometry has been used to examine the kinetic energy dependence of the reaction of ground state atomic oxygen ion with molecular nitrogen from 0.03 to 30 eV. This represents a much wider energy range than has been examined previously in any single ion beam, flowing afterglow (FA), or flow/drift (FD) study. Cross sections for the NO^+ + N product channel show an exothermic dependence on kinetic energy below 0.25 eV. The present results demonstrate that this reactivity occurs via a single collision mechanism, equation (3.3), which can be modeled using a Landau-Zener formalism. At higher energies, the cross sections exhibit an endothermic kinetic energy dependence with an apparent threshold of 0.33 $\pm$ 0.08 eV. This corresponds to the effective activation barrier on the quartet reaction surface.

The present results are in good qualitative agreement with all previous beam, FA, and FD studies. This demonstrates that the guided ion beam technique can provide reasonably accurate experimental cross sections and rate constants throughout

the energy range examined. However, the present data (converted to rate constant form) and the results of FA and FD studies do not agree quantitatively. The disagreements are shown to result primarily from differences in ion energy distributions. A model, II, for the "true" cross section behavior which is consistent within experimental error with the FA and FD and beam data, is derived. This model differs from the "true" cross section previously derived from FD data. This latter cross section is inconsistent with the cross sections measured directly in the present experiment. The discrepancy is almost certainly due to the extreme difficulties in accounting for the distribution of ion energies in FD studies. Finally, it is observed that differences in interaction region pressures between the FA and FD studies and the ion beam study could also influence the reaction rate observed at low energies. Additional work would be useful in uncovering the low energy dynamics associated with reaction (3.1) and in ascertaining the role of multiple collisions in this process.

3.5 REFERENCES

1. G. Gioumousis and D. P. Stevenson, J. Chem. Phys. **29**, 294 (1958).
2. C. Giese, in Ion-Molecule Reactions in the Gas Phase, edited by P. J. Ausloos (American Chemical Society, Washington, D.C., 1966), p. 20.
3. B. R. Turner, J. A. Rutherford, and D. M. J. Compton, J. Chem. Phys. **48**, 1602 (1968).
4. J. J. Leventhal, J. Chem. Phys. **54**, 5102 (1971).
5. J. A. Rutherford and D. A. Vroom, J. Chem. Phys. **55**, 5622 (1971).
6. B. M. Hughes and T. O. Tiernan, J. Chem. Phys. **55**, 3419 (1971).
7. R. B. Cohen, J. Chem. Phys. **57**, 676 (1972).
8. R. H. Neynaber and G. D. Magnuson, J. Chem. Phys. **58**, 4586 (1973).
9. G. P. K. Smith and R. J. Cross, Jr., J. Chem. Phys. **60**, 2125 (1974).
10. R. F. Stebbings, B. R. Turner, and J. A. Rutherford, J. Geophys. Res. **71**, 771 (1966).
11. R. Johnsen and M. A. Biondi, J. Chem. Phys. **59**, 3504 (1973).
12. M. McFarland, D. L. Albritton, F. C. Fehsenfeld, E. E. Ferguson, and A. L. Schmeltekopf, J. Chem. Phys. **59**, 6610 (1973); M. McFarland, D. L. Albritton, F. C. Fehsenfeld, E. E. Ferguson, and A. L. Schmeltekopf, J. Chem. Phys. **59**, 6620 (1973).
13. D. L. Albritton, I. Dotan, W. Lindinger, M. McFarland, J. Tellinghuisen, and F. C. Fehsenfeld, J. Chem. Phys. **66**, 410 (1977).
14. R. Johnsen and M. A. Biondi, J. Chem. Phys. **73**, 190 (1980).

15. D. Smith, N. G. Adams, and T. M. Miller, J. Chem. Phys. **69**, 308 (1978).

16. J. Glosik, A. B. Rakshitt, N. D. Twiddy, N. G. Adams, and D. Smith, J. Phys. B: Atom. Molec. Phys. **11**, 3365 (1978).

17. A. L. Schmeltekopf, E. E. Ferguson, and F. C. Fehsenfeld, J. Chem. Phys. **48**, 2966 (1968).

18. D. B. Dunkin, F. C. Fehsenfeld, A. L. Schmeltekopf, and E. E. Ferguson, J. Chem. Phys. **49**, 1365 (1968).

19. E. E. Ferguson, D. K. Bohme, F. C. Fehsenfeld, and D. B. Dunkin, J. Chem. Phys. **50**, 5039 (1969).

20. D. K. Bohme, D. B. Dunkin, F. C. Fehsenfeld, and E. E. Ferguson, J. Chem. Phys. **49**, 5201 (1968).

21. G. F. O. Langstroth and J. B. Hasted, Disc. Faraday Soc. **33**, 298 (1962).

22. J. Sayers and D. Smith, Disc. Faraday Soc. **37**, 167 (1964).

23. D. K. Bohme, D. B. Dunkin, F. C. Fehsenfeld, and E. E. Ferguson, J. Chem. Phys. **51**, 863 (1969).

24. J. J. Kaufman and W. S. Koski, J. Chem. Phys. **50**, 1942 (1969).

25. T. F. O'Malley, J. Chem. Phys. **52**, 3269 (1970).

26. A. Pipano and J. J. Kaufman, J. Chem. Phys. **56**, 5258 (1972).

27. D. G. Hopper, Chem. Phys. Lett. **31**, 446 (1975).

28. D. G. Hopper, J. Am. Chem. Soc. **100**, 1019 (1978).

29. D. G. Hopper, J. Chem. Phys. **72**, 3679 (1980).

30. D. G. Hopper, J. Chem. Phys. **72**, 4676 (1980).

31. D. G. Hopper, J. Chem. Phys. **76**, 1068 (1982).

32. D. G. Hopper, J. Chem. Phys. **77**, 314 (1982).

33. F. A. Wolf, J. Chem. Phys. **44**, 1619 (1966).

34. K. P. Huber and G. Herzberg, Constants of Diatomic Molecules, (Van Nostrand Reinhold, New York, 1979).

35. T. F. Moran and J. B. Wilcox, J. Chem. Phys. **69**, 1397 (1978).

36. C. Ottinger and J. Simonis, Chem. Phys. **28**, 97 (1978).

37. A. Henglein and K. Lacmann, Adv. Mass. Spectrom. **3**, 331 (1966); A. Henglein, in Ion-Molecule Reactions in the Gas Phase, edited by P. J. Ausloos (American Chemical Society, Washington, D.C., 1966), p. 63; A. Ding, K. Lacmann, and A. Henglein, Ber. Bunsenges. Phys. Chem. **71**, 596 (1967).

38. K. M. Ervin and P. B. Armentrout, J. Chem. Phys. **83**, 166 (1985).

39. C. Lifshitz, R. L. C. Wu, T. O. Tiernan and D. T. Terwillger, J. Chem. Phys. **68**, 247 (1978).

40. M. E. Weber, J. L. Elkind, and P. B. Armentrout, J. Chem. Phys. **84**, 1521 (1986).

41. The best fit between the present cross section data and the fall-off model presented in reference 40 corresponds to D = 9.76 eV, f = 1.0, and p = 4.0.

42. L. D. Landau, Phys. Z. Sowjetunion **2**, 46 (1932).

43. C. Zener, Proc. R. Soc. London Ser. A **137**, 696 (1932).

44. A. P. M. Baede, Ad. Chem. Phys. **30**, 463 (1975).

45. J. Tully, J. Chem. Phys. **61**, 61 (1974).

46. L. A. Viehland and E. A. Mason, J. Chem. Phys. **66**, 422 (1977).

47. S. L. Lin and J. N. Bardsley, J. Chem. Phys. **66**, 435 (1977).

48. W. Lindinger and D. L. Albritton, J. Chem. Phys. **62**, 3517 (1975).

49. I. Dotan, W. Lindinger, and D. L. Albritton, J. Chem. Phys. **64**, 4544 (1976).

50. D. L. Albritton, in Kinetics of Ion - Molecule Reactions, edited by P. J. Ausloos (Plenum, New York, 1979), p. 132.

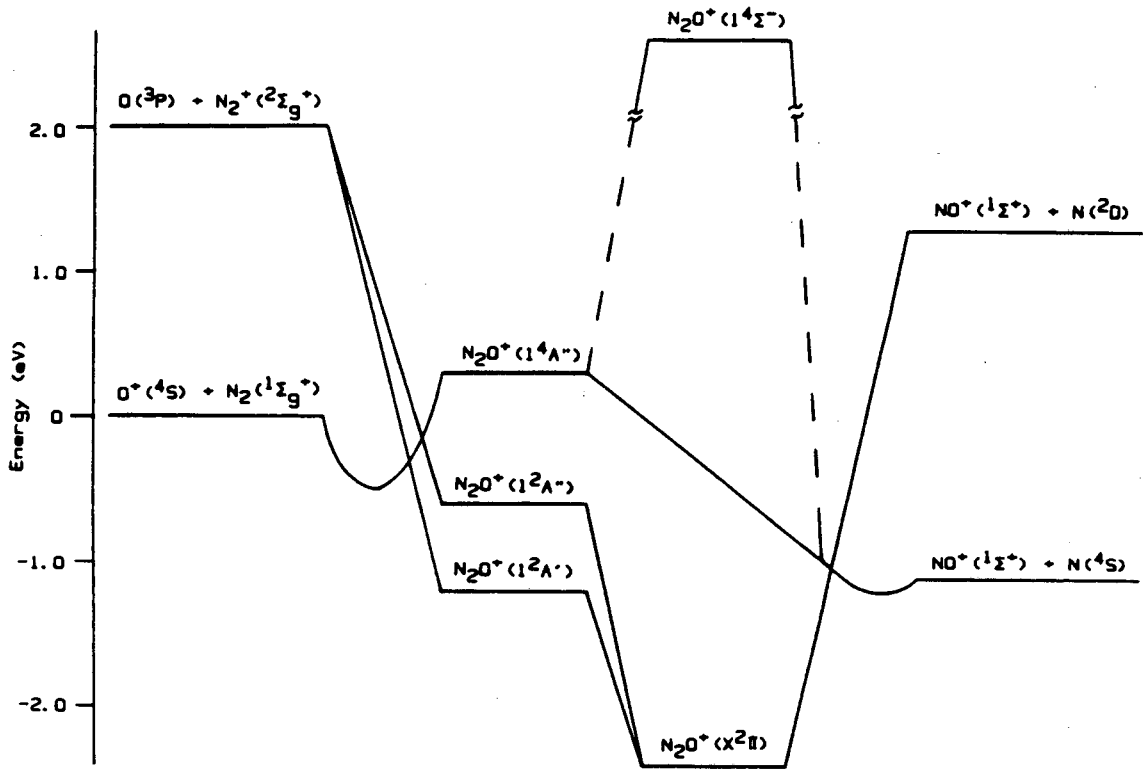

Figure 3-1. Electronic state correlation diagram for N_2O^+ in C_s (130°) and $C_{\infty v}$ symmetry. The energies of the C_s intermediates, the location of the crossing between the $1^4A''$ and $1^2A''$ surfaces, and the depths of the $O^+ + N_2$ and $NO^+ + N$ ion - induced dipole potential wells are taken from Hopper, reference. 28.

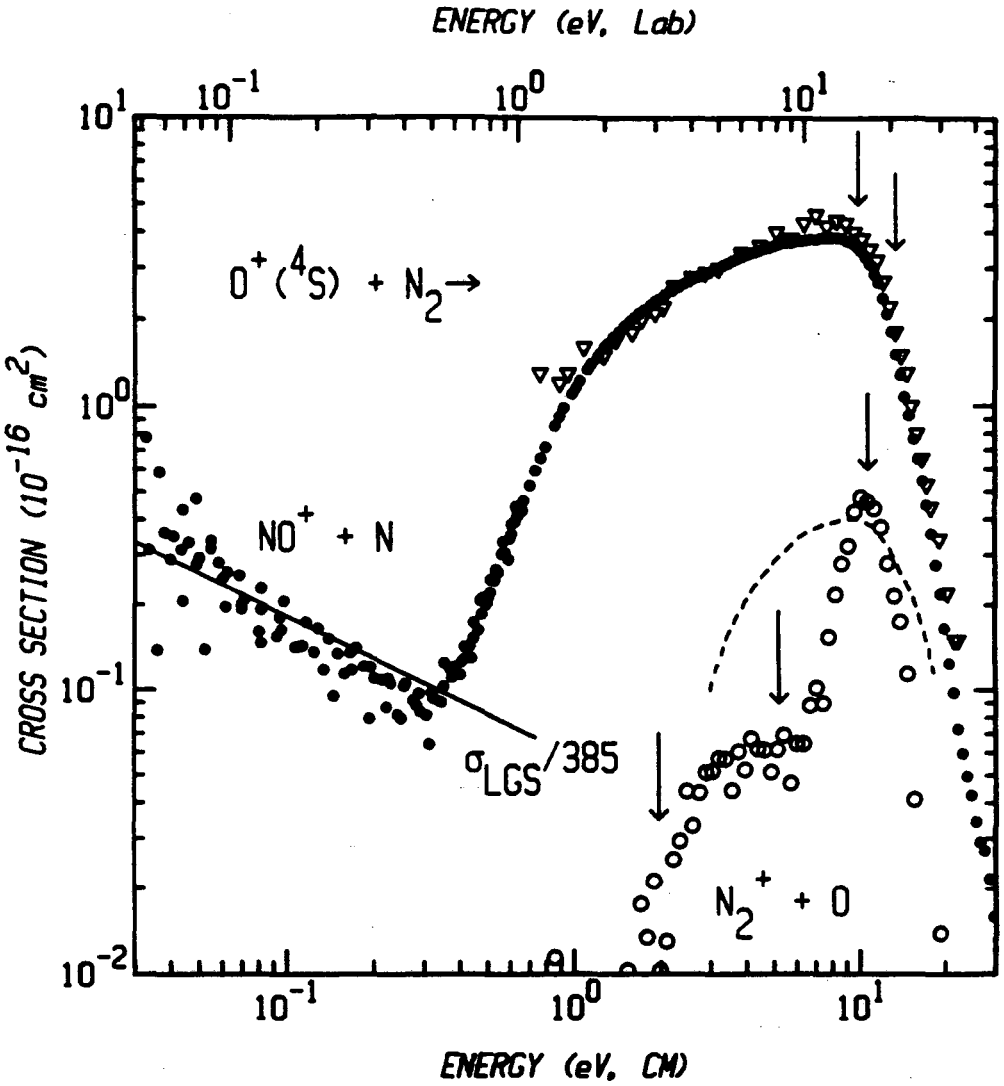

Figure 3-2. Cross sections for reactions (3.1) (filled circles) and (3.4) (open circles) as a function of relative translational energy (lower scale) and laboratory energy (upper scale). The O^+ is generated by electron impact ionization of CO_2 at 70 eV and passed through the drift cell filled with N_2. For the $NO^+ + N$ channel, arrows indicate the thermodynamic and spectator stripping dissociation energies of NO^+ at 9.76 eV and 13.3 eV, respectively. For the $N_2^+ + O$ channel, arrows designate the thermodynamic thresholds for production of $N_2^+(X^2\Sigma_u^+)$ at 1.96 eV and of $N_2^+(B^2\Sigma_u^+)$ at 5.2 eV, and the thermodynamic dissociation energy of N_2^+ at 10.7 eV. Also included are cross section data from reference 5 for reaction (3.1) (open triangles), a phase space cross section for reaction (3.4) from reference 33 (dashed line), and the LGS cross section (equation (2.4)) scaled down by a factor of 385 (solid line).

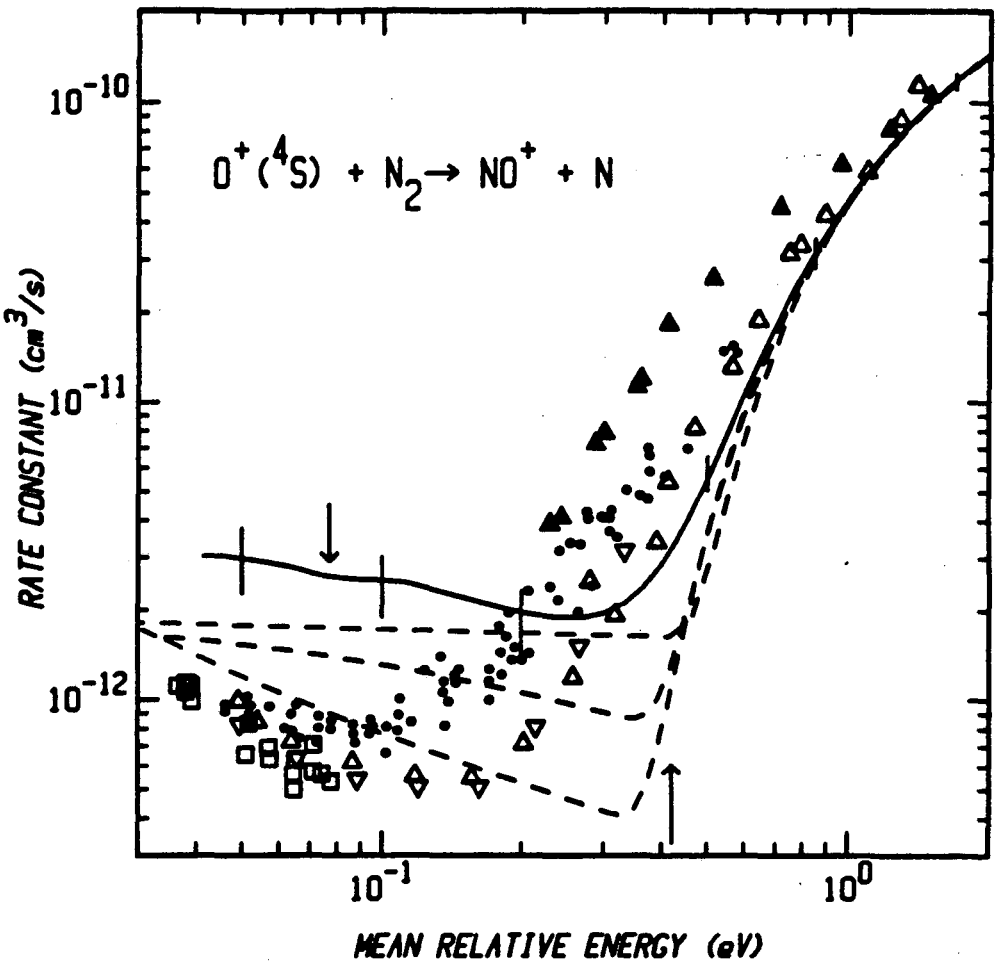

Figure 3-3. Phenomenological rate constants for reaction (3.1) as a function of the mean relative energy of the reactants. The present data (solid line with error bars) are derived from the cross section data in Figure 3-2 through the use of equation (2.7). Also included are the flowing afterglow results of reference 19, (open squares), the flow/drift tube results of reference 11 (solid circles), and the argon (solid triangles) and helium (open triangles) buffered FD data from reference 13. The upper, lower, and middle dashed lines correspond to the rate constants obtained from the unconvoluted forms of models I, II, and III, respectively, which are discussed in the text. Vertical arrows are located at 0.10 eV and 0.64 eV lab, the two energies examined in Figure 3-6.

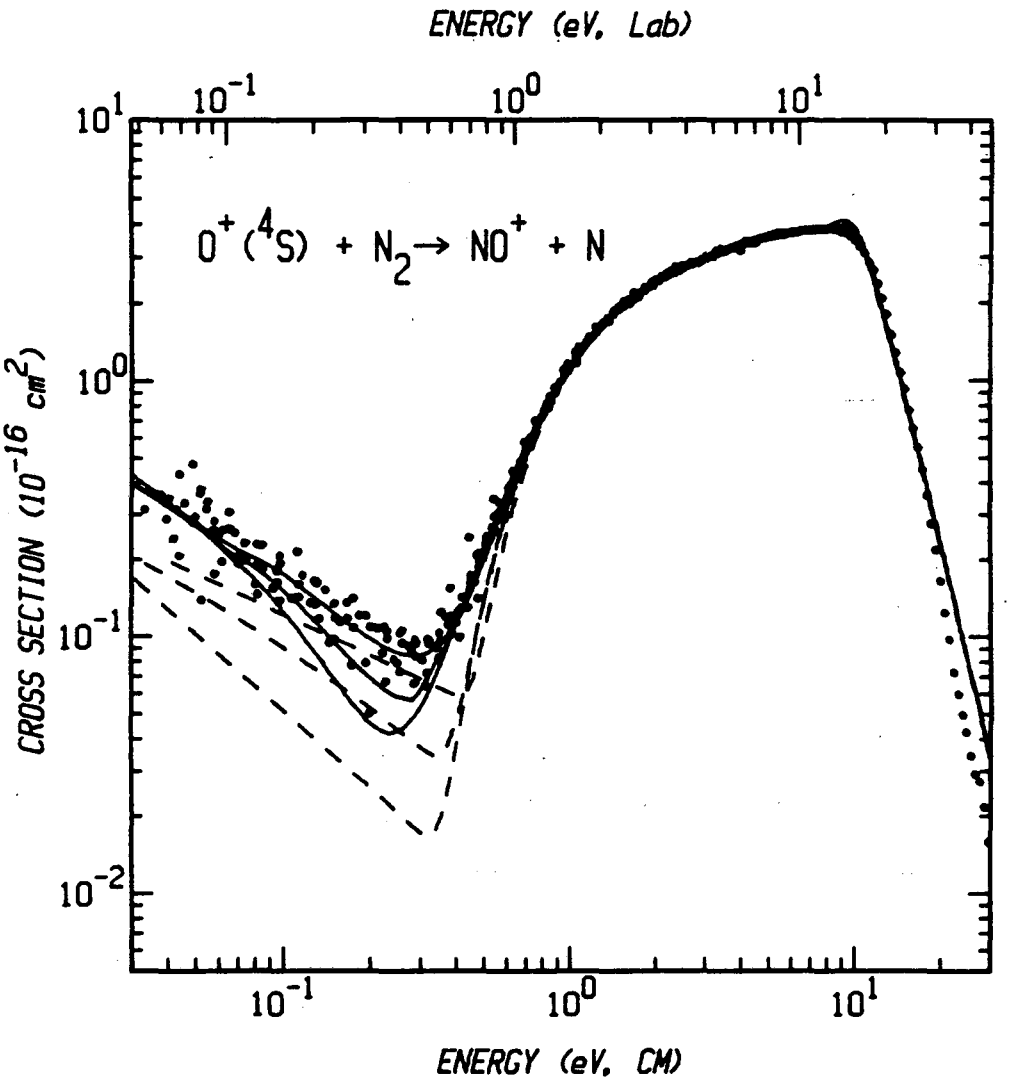

Figure 3-4. Cross sections for reaction (3.1) as a function of the relative translational energy (lower scale) and laboratory energy (upper scale). The data (solid circles, same as Figure 3-2) are compared with the three cross section models discussed in the text (dashed lines) and their convolutions over the experimental energy distribution (solid lines). Models I, II, and III correspond to the upper, lower, and middle curves, respectively.

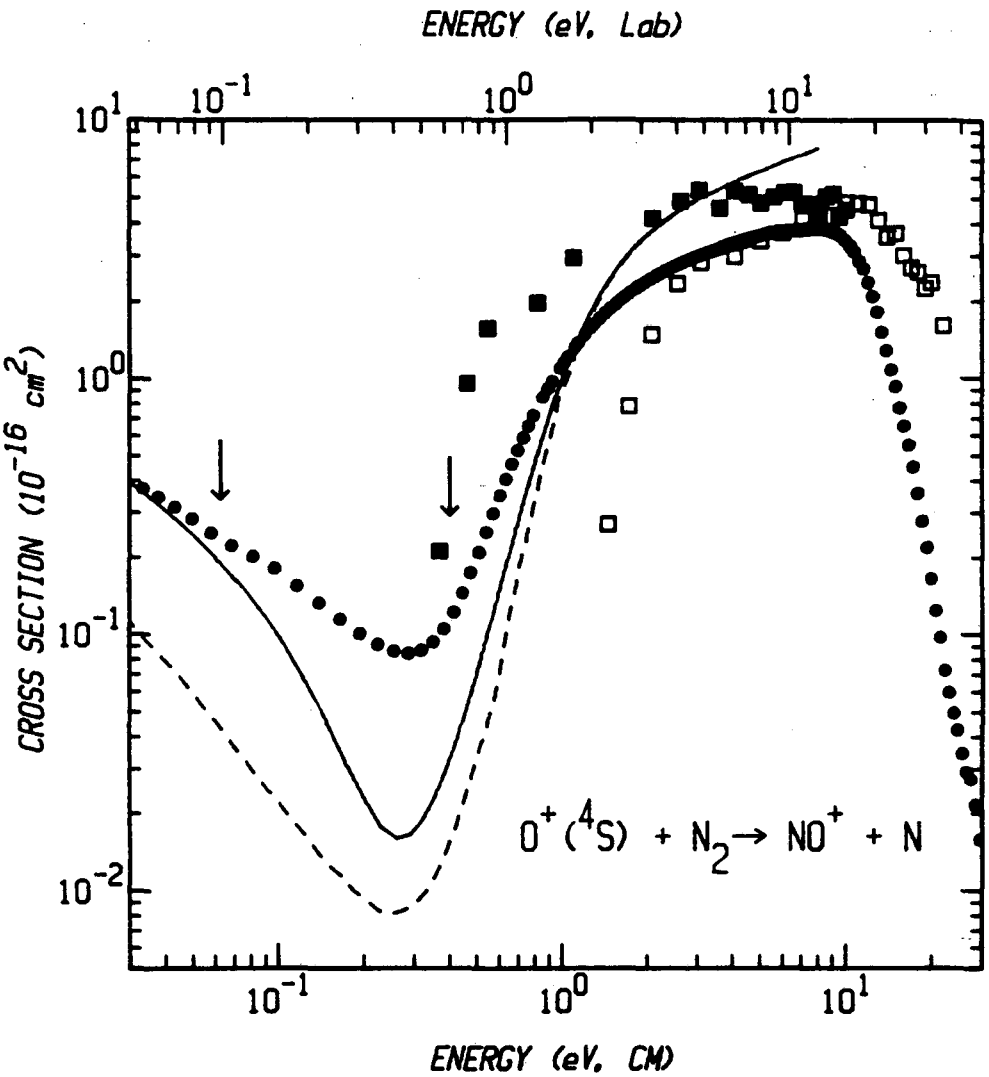

Figure 3-5. Cross sections for reaction (3.1) as a function of the relative translational energy (lower scale) and laboratory energy (upper scale). The present results are given by the solid circles and represent an average of the data shown in Figure 3-2. The cross section derived by Albritton and coworkers (reference 13) and its convolution over the distribution of energies in the present ion beam experiment are designated by the dashed and solid lines, respectively. Results of Hopper's semiclassical trajectory calculations (reference 32) are denoted by the solid (0.25 eV barrier height) and open (0.99 eV barrier height) squares. Vertical arrows are located at 0.10 eV and 0.64 eV lab, the two energies examined in Figure 3-6.

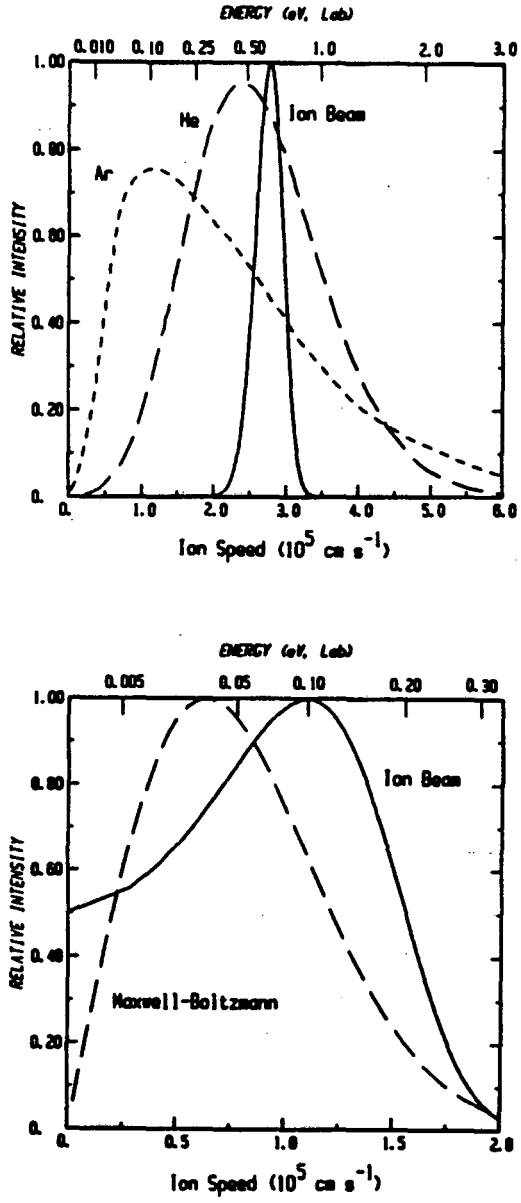

Figure 3-6. Ion speed (lower scale) and energy (upper scale) distributions for an average laboratory energy of 0.64 eV (part a) and 0.10 eV (part b). The distributions from the present experiment are shown by the solid lines, and the FD distributions (reference 50) are shown by the dashed (Ar buffer) and broken (He buffer) lines. The Maxwell-Boltzmann distribution is given by a broken line in part b.

Chapter Four

Kinetic Energy Dependence of $C^+(^2P) + O_2$

4.1 INTRODUCTION

The reaction of ground state atomic carbon ion with molecular oxygen has three primary reaction channels: atom abstraction, process (4.1a); abstraction - charge transfer, process (4.1b); and simple charge transfer, process (4.1c).[1]

$$C^+(^2P) + O_2 \rightarrow CO^+ + O \qquad \Delta H^\circ = -3.24 \text{ eV} \qquad (4.1a)$$

$$\rightarrow O^+ + CO \qquad \Delta H^\circ = -3.64 \text{ eV} \qquad (4.1b)$$

$$\rightarrow O_2^+ + C \qquad \Delta H^\circ = 0.81 \text{ eV} \qquad (4.1c)$$

To date, these reactions have been examined by a wide range of techniques: flowing afterglow (FA),[2-4] flow/drift tube (FD),[5] selected ion flow tube (SIFT),[6-10] ion cyclotron resonance (ICR),[11,12] and ion beams.[13-17] Reaction rate constants[2,3,5-9,11,12] and reaction cross sections[15-17] have been measured, and the branching ratio between channels (4.1a) and (4.1b) has been obtained.[5-12] In some cases, disposal of reaction exoergicity has also been investigated.[4,12-14,17] Despite this intense effort, the mechanism of this reaction is not well understood and values for the cross sections, rate constants, and branching ratios cover a surprisingly large range.

One possible explanation for the variation in the previous results is that the electronic or kinetic energies of the C^+ ion were not adequately controlled in many of these studies. In the present chapter, beams of pure ground state C^+ are generated and reacted with O_2 over a kinetic energy range of 0.05 to 35 eV. Total reaction

cross sections, reaction rate constants, and product branching ratios are measured, and compared to previous results and to the predictions of phase space theory (PST). Finally, the reaction mechanism and potential energy surfaces for these processes are discussed in some detail.

4.2 EXPERIMENTAL

4.2.1 Pressure Dependence

For the present system, multiple collisions in the main cell are a problem because the secondary charge transfer reaction between CO^+ and O_2, process (4.2),[1]

$$CO^+ + O_2 \rightarrow O_2^+ + CO \qquad \Delta H^\circ = -1.94 \text{ eV} \qquad (4.2)$$

is fairly efficient (the rate constant at 300 K is 1-2 x 10^{-10} cm^3 s^{-1}).[2,8,18] The effect that this reaction has on the data is shown by Figures 4-1a and 4-1b. In Figure 4-1a, product ion formation is measured at an energy of ~ 0.15 eV, well below the thermodynamic threshold for reaction (4.1c). At this energy the data show linear pressure dependencies for the single collision processes (4.1a) and (4.1b), and a quadratic pressure dependence for formation of O_2^+ via the reaction sequence (4.1a) + (4.2). In Figure 4-1b, the same measurement is repeated at an energy of ~ 4 eV. Because this energy is in excess of the thermodynamic threshold for reaction (4.1c) and the contribution of the secondary reaction (4.2) is small at this energy, a linear pressure dependence is observed for all three reaction channels. Although it is possible to maintain the O_2 reactant gas pressures low enough so that the effect of reaction (4.2) is negligible at all energies, such pressures are below the measurable

range of the capacitance manometer. To overcome this difficulty, cross section measurements are made over a range of O_2 pressures and then extrapolated to zero pressure to obtain the true "single collision" cross sections.

4.2.2 Reaction Rates

In order to compare the present results to previous FA, FD, SIFT and ICR studies, the cross sections must be converted into rate constants. The true thermal rate constant as a function of temperature is obtained by averaging the experimental cross section over a Maxwell-Boltzmann distribution of relative energies,

$$k(T) = (1/\pi\mu)^{1/2} \cdot (2/k_B T)^{3/2} \int_0^\infty \sigma(E) \cdot E \cdot \exp(-E/k_B T) \cdot dE, \qquad (4.3)$$

where μ is the reduced mass of the reactants, k_B is the Boltzmann constant, T is the temperature in degrees Kelvin, and E is the actual relative energy of the reactants. Since only the translational energy of the reactants is varied in these experiments, equation (4.3) is actually an expression for $k(T_t)$, the rate constant as a function of translational temperature. Reaction rates for specific temperatures can be obtained by direct numerical integration of equation (4.3); however, this relies on accurately relating the experimentally observed cross section, $\sigma(E_0)$, to the true cross section, $\sigma(E)$.

Rate constants can also be calculated as functions of the mean relative energy of the reactants via equation (2.7). A description of this technique is given in the experimental section of Chapter 2.

4.3 RESULTS

4.3.1 Total Cross Sections and Rate Constants

The experimental results for reactions (4.1a) - (4.1c) and their total are shown in Figure 4-2. For comparison, the collision cross section predicted by the Langevin-Gioumousis-Stevenson (LGS) model[19,20] is also presented. At the lowest energies, the experimentally measured total cross section approaches the magnitude of σ_{LGS}, but the experimental cross section falls off more rapidly than σ_{LGS} as the kinetic energy increases. While the experimental cross section is 0.77 σ_{LGS} at $E_0 = 0.05 \pm 0.036$ eV, it is 0.53 σ_{LGS} at 0.1 eV, 0.38 σ_{LGS} at 0.5 eV, and ~ 0.30 σ_{LGS} from 2 to 5 eV. The experimental cross section then drops off to a minimum efficiency of 0.15 σ_{LGS} at an energy of ~ 17 eV before rising to ~ 0.2 σ_{LGS} at the highest energies measured. A numerical fit to the data over the range $0.1 \leq E_0 \leq 3.0$ eV is given by $\sigma(E_0) = (7.3 \pm 1.1)\, E_0^{-0.66 \pm 0.09}$ Å^2 while σ_{LGS} takes on the form $21.3\, E^{-0.5}$ Å^2. At higher energies, $6 \leq E_0 \leq 12$ eV, the total cross section can be numerically represented as $\sigma(E_0) = (31 \pm 16)\, E_0^{-1.4 \pm 0.2}$ Å^2. At the highest energies, the cross section levels out at a value of ~ 0.7 Å^2. At the lowest energies, $0.05 \leq E_0 \leq 0.1$ eV, the total cross section behaves as $(3.6 \pm 2.5)\, E_0^{-1.0 \pm 0.4}$ Å^2. It should be noted, however, that the behavior of the cross sections in this energy region is rather uncertain since the energy scale uncertainty is ± 0.036 eV. For example, a shift in the energy scale of only 0.025 eV would mean that the total cross section behaves as $7.0\, E_0^{-0.63}$ between 0.025 and 2 eV.

In Figure 4-3, the rate constants for reactions (4.1a) - (4.1c) are plotted as a function of the mean relative interaction energy, <E>. The data are the same as those shown in Figure 4-2, but have been converted to rate constant form through the use of equation (2.7). Also shown in Figure 4-3 is the rate constant predicted by the LGS model.[19,20] For reaction (4.1, total), k_{LGS} is equal to 1.00×10^{-9} cm^3 s^{-1}. As can be seen from the data in Figure 4-3, the experimental rate constant for the total reaction at the lowest mean relative energy, $\langle E \rangle = 0.06 \pm 0.036$ eV, is 7.7×10^{-10} cm^3 s^{-1}. This should be a reasonable approximation to the room temperature rate constant since $3k_BT/2 = 0.04$ eV at T = 300 K. The thermal rate constant can also be obtained by using equation (4.3) with T = 300 K. This procedure requires that the true form of the cross section be known down to very low energies. Since this is not directly measured, it is necessary to extrapolate the experimental cross sections. The extrapolation can be done in several reasonable ways and these lead to k(300) values ranging from 7.1 to 7.9×10^{-10} cm^3 s^{-1}. The average of all the various values leads to k(300) = $(7.6 \pm 0.3) \times 10^{-10}$ cm^3 s^{-1}, with an absolute uncertainty of $\pm 20\%$ (1.6×10^{-10} cm^3 s^{-1}). If the uncertainty associated with the energy scale (± 0.036 eV) is explicitly considered, the uncertainty in the rate constant increases to $\pm 30\%$ (2.3×10^{-10} cm^3 s^{-1}).

The average k(300) value obtained from the present data is compared to several room temperature rate constants from the literature in Table 4-I. The present result is in good agreement with the FD measurements of St. Niccolini *et al.*,[5] and the SIFT measurement of Tichy *et al.*.[9] The ICR measurement of Rincon, Pearson, and

Bowers (RPB),[12] the FA measurement of Rakshit *et al.*,[3] and the SIFT measurements of Adams and Smith,[6,7] and Miller *et al.*[8] are within experimental error. The measurements of Fehsenfeld *et al.*[2] and Anicich *et al.*[11] are almost certainly too high. As noted by RPB,[12] some of these measurements may be high due to the presence of excited state C^+ ions. The present value pertains to ground state $C^+(^2P)$ and so do the values from references 3, 11, and 12. Tichy *et al.*[9] correct their results for the presence of excited C^+ ions such that the value reported is judged to be for ground state C^+ ions. In all other work, the possibility that excited $C^+(^4P)$ ions are present cannot be eliminated.

The behavior of the total rate constant as a function of energy can also be compared with the results of St. Niccolini *et al.*,[5] who studied the energy dependence of reaction (4.1) in a flow drift tube from $\langle E \rangle = 0.04$ to 1 eV. The rates St. Niccolini measured did not vary over this energy range within experimental error. This behavior clearly differs from that shown by the present data, which decrease by about a factor of 2 over the 0.04 - 1.0 eV range. (This discrepancy is discussed further below.) Other relevant studies include those of Miller *et al.*,[8] who found that the rate constant for reaction (4.1) is relatively insensitive ($<12\%$ variation) to temperature from 90 K ($3k_BT/2 = 0.01$ eV) to 450 K ($3k_BT/2 = 0.06$ eV), and Rakshit *et al.*,[3] who found the same rate constant at 300 and 100 K. However, these results are not directly comparable to those of the present report since the latter do not cover this low energy range.

4.3.2 Branching Ratio: $O^+ + CO$ vs. $CO^+ + O$

As Figure 4-2 shows, the manner in which the total cross section is partitioned between reactions (4.1a), (4.1b), and (4.1c) is highly dependent on the interaction energy. At energies below the onset for reaction (4.1c), σ_{total} is partitioned entirely between reactions (4.1a) and (4.1b). Over the energy range $0.1 \leq E_0 \leq 1.0$ eV, the cross sections for these products behave as $\sigma(4.1a) = (5.1 \pm 0.6)\ E_0^{-0.50 \pm 0.08}\ \text{Å}^2$ and $\sigma(4.1b) = (2.1 \pm 0.4)\ E_0^{-1.0 \pm 0.1}\ \text{Å}^2$. Above 1 eV, $\sigma(4.1b)$ continues to fall as E_0^{-1} until about 4 eV; however, $\sigma(4.1a)$ declines as $(4.9 \pm 0.6)\ E_0^{-0.63 \pm 0.06}\ \text{Å}^2$ from 1 to 4 eV. This change in the energy behavior of the $CO^+ + O$ channel is largely due to competition with reaction (4.1c), $O_2^+ + C$. Indeed, the sum of the cross sections for reactions (4.1a) and (4.1c) behaves as $(5.1 \pm 0.6)\ E_0^{-0.50 \pm 0.04}\ \text{Å}^2$ between 0.1 and 4 eV, the same energy dependence shown by $\sigma(4.1a)$ at low energies. This indicates that reaction (4.1c) competes primarily with reaction (4.1a) and does not appear to have an appreciable effect on reaction (4.1b).

The competition between channels (4.1a) and (4.1b) is shown in Figure 4-4 in terms of the O^+ product fraction, $f(O^+) = \sigma(4.1b)/[\sigma(4.1a) + \sigma(4.1b)]$. At the lowest energy, the $O^+ + CO$ channel is favored over $CO^+ + O$ by a 0.60 to 0.40 margin. This is in good agreement with a variety of measurements at thermal energies, Table 4-I. However, as the interaction energy increases, the value of the branching ratio declines. At $E_0 = 0.13 \pm 0.04$ eV ($\langle E \rangle = 0.14$ eV), the total cross section is divided equally between O^+ and CO^+, and at higher energies CO^+ is favored. The steady decline in the branching ratio is a direct result of the different

energy dependencies for the two reaction channels. The change in the branching ratio can be given numerically as $f(O^+) = -0.243 \log(E_0) + 0.284$ for energies between 0.05 and 0.8 eV. (Note that this formula predicts that $f(O^+) = 0.66$ at $\langle E \rangle = 0.039$ eV $= 3k_BT/2$ at 300 K.) If the fraction of O^+ product is calculated as $f(O^+) = \sigma(4.1b)/\sigma(4.1, \text{total})$, then this numerical form for $f(O^+)$ continues to be valid until about 4 eV, Figure 4-4. This is another indication that the $O_2^+ + C$ product channel primarily competes with the $CO^+ + O$ product channel.

Previous researchers have also measured the kinetic energy dependence of the branching ratio between reactions (4.1a) and (4.1b). Results from these studies, Figure 4-4, also show that the fraction of O^+ product drops with increasing kinetic energy. Unfortunately, the quantitative comparisons between different sets of data are not completely satisfactory. The data of St. Niccolini *et al.*[5] were obtained using a flow drift tube apparatus. The kinetic energy dependence of their data is in good agreement with the current data at low energies but disagrees above 0.2 eV. The explanation for the discrepancy is presumably that the ion mobilities in the drift tube are not adequately characterized at elevated electric fields. The data indicate that mean kinetic energies above ~ 0.15 eV are not reached in the FD experiments. Note that this can help explain their observation (discussed above) that the total reaction rate does not change appreciably in the FD experiments. The ICR data at elevated energies of RPB[12] differ in a similar manner from the present data, i.e. they are consistent only if they really for lower kinetic energies. This possibility is noted by RPB,[12] who state that their non-thermal kinetic energies are upper limits with

uncertainties of about 50%. Indeed, their measurements are in reasonable agreement with the present data at the lower limits of their estimated energies, Figure 4-4.

The present results may also serve to clarify the anomalous branching ratios listed in Table 4-I. The tandem ICR results of Anicich *et al.*[11] have long been suspected of having an inverted product distribution because of kinetic excitation.[12,21] The current results support this view and show that the effective kinetic energy in the TICR system was ~ 0.5 eV. This is lower than the 1.6 ± 0.5 eV estimate arrived at by RPB[12] based on their branching ratio results. However, an energy of 0.5 eV is consistent with the fact that Anicich *et al.* formed C^+ by using reaction (4.4),[1]

$$He^+ + CO \rightarrow C^+(^2P) + O(^4S) \qquad \Delta H^\circ = -2.2 \text{ eV} \qquad (4.4)$$

which is known to produce C^+ ions with 1.1 eV of translational energy.[22] In reaction with O_2, this laboratory energy is equivalent to 0.8 eV of kinetic energy in the center of mass frame. The present result clearly suggests that these ions were incompletely thermalized in the TICR study.

There is also some question about the results of Tichy *et al.*[9] who attribute their 53:47 branching ratio to the presence of 10% $C^+(^4P)$ excited ions in their experiment. As pointed out by RPB,[12] this is inconsistent with the results of Miller *et al.*,[8] who obtain a branching ratio of 62:38 but form C^+ in a way which should yield appreciable amounts of $C^+(^4P)$, ~ 65%.[23] As discussed by RPB, one possible explanation is that the excited ions in the study of Miller *et al.* are efficiently deactivated in the source. Another possibility is that when $C^+(^4P)$ is deactivated, it yields translationally hot $C^+(^2P)$, which then forms relatively more CO^+ than thermal

$C^+(^2P)$. The extent of this kinetic excitation would depend critically on the experimental conditions in the drift tube. For instance, Tichy *et al.*'s result could be explained by ions with an average kinetic energy of only 0.1 eV.

4.3.3 $O_2^+ + C$

As discussed above, the formation of O_2^+ has a pronounced pressure dependence. This is illustrated in Figure 4-2 by a comparison of the cross section measured at $P(O_2) = 0.22$ mTorr to that obtained from an extrapolation to $P(O_2) = 0$. The difference between these measurements is due to the secondary reaction (4.2). The zero pressure cross section is the true cross section for reaction (4.1c), charge transfer to give $O_2^+ + C$. It exhibits an onset near 0.6 eV and then rises rapidly to a plateau of ~ 0.6 Å^2. There are some oscillations in the data in this plateau region. These are attributed to variations in the collection efficiency of the charge transfer product, which may be formed with little forward velocity in the laboratory frame. Because 100% product collection cannot be ensured in these cases, the magnitude of the cross section for reaction (4.1c) may not be completely reliable at high energies.

The only other measurement of process (4.1c) in this energy range is that of Koski and coworkers,[15] who obtain a much smaller cross section ($\sigma = 0.17$ Å^2 at 36 eV) with a much higher onset ($\sigma = 0.01$ Å^2 at 3.6 eV). This large discrepancy is probably due to the difficulty of quantitatively collecting the slow charge transfer product. Moran and Wilcox[16] have measured the charge transfer cross section at much higher kinetic energies (500 - 1,800 eV c.m.) and find that the cross section

rises from ~ 8 to 16 Å^2 over this energy range. These results can be smoothly extrapolated to the present data.

The presence of O_2^+ product before the 0.81 eV thermodynamic threshold of reaction (4.1c) is due to energy broadening effects from the distribution of ion kinetic energies in the ion beam and the random thermal motion of the O_2 reactant gas. In order to determine the true cross section behavior in the threshold region, an appropriate model for the true cross section is convoluted over the experimental distributions of ion and neutral energies.[24] The convoluted form of the trial cross section is then compared directly to the experimentally observed cross section. Finally, the parameters of the trial function are adjusted using non-linear least squares procedures to obtain the best possible fit to the actual data.

For the case of reaction (4.1c), it is possible to accurately reproduce the behavior of the experimental cross section with the line-of-centers model,[25]

$$\sigma(E) = \sigma_0(1 - E_T/E) \qquad \text{if } E > E_T \tag{4.5a}$$

$$\sigma(E) = 0 \qquad \text{if } E < E_T \tag{4.5b}$$

where $\sigma(E)$ is the true cross section and E is the relative kinetic energy of the reactants. E_T, the threshold energy, and σ_0 are treated as adjustable parameters. The best fit between the experimental data and the model is obtained when E_T = 0.82 eV (in excellent agreement with the calculated thermochemistry) and σ_0 = 0.63 Å^2. The unconvoluted and convoluted forms of this cross section are shown in Figure 4-5, and can be seen to reproduce the data well throughout the energy range shown.

4.3.4 $CO^+ + O$: High Energies

At energies above ~ 5 eV, the cross section for reaction (4.1a) declines rapidly, causing the total cross section to fall until it is dominated by the charge transfer process, reaction (4.1c). For reaction (4.1a), the cross section decline in the region $7 \leq E_0 \leq 35$ eV can be reproduced by $\sigma(E_0) = (308 \pm 218)\ E_0^{-2.7 \pm 0.5}\ \text{Å}^2$. The rapid fall-off of the CO^+ product is easily explained as being due to dissociation of the CO^+ product via reactions (4.6a) and (4.6b).[1]

$$C^+(^2P) + O_2 \rightarrow C^+ + O + O \qquad \Delta H^\circ = 5.12\ \text{eV} \qquad (4.6a)$$

$$\rightarrow O^+ + O + C \qquad \Delta H^\circ = 7.47\ \text{eV} \qquad (4.6b)$$

Direct evidence for the occurrence of reaction (4.6b) is the increase in production of O^+ at energies above about 12 eV. This rise in O^+ appears to correlate with a slight downward break in the CO^+ cross section also at ~ 12 eV. Reaction (4.6a) cannot be observed directly since the ionic product is the same as the reactant ion. However, it can be seen that the beginning of the cross section decline in reaction (4.1a) is very close to the thermodynamic threshold for reaction (4.6a). Furthermore, the increase in $\sigma(O^+)$ is much too small to fully account for the decline in the CO^+ cross section.

The only previous measurement of reaction (4.1a) at elevated energies is that of Koski and coworkers.[15] They attempted to evaluate the reaction cross sections for both $C^+(^2P)$ and $C^+(^4P)$ between 3.6 and 145 eV (5 to 200 eV lab). For ground state C^+, they found a cross section for reaction (4.1a) in reasonable agreement with the present one at their lowest energies (3.6 to 6 eV), although their cross section *increases* from low to high energy. Above 6 eV, their cross section falls precipi-

tously to about 0.1 $Å^2$ at 7.3 eV (10 eV lab), while the present measurement falls off more gradually. These discrepancies can be attributed to difficulties in collection efficiency and in accurately separating the reactivities of the different states of C^+ in the older study.

The high energy behavior of σ(4.1a) can be analyzed in somewhat more detail by using a previously discussed statistical model for dissociation.[26] A dissociation onset of 5.2 $\pm$ 0.5 eV is obtained,[27] in good agreement with the 5.1 eV thermodynamic threshold for reaction (4.6a). This implies that reaction (4.1a) has a strong statistical component. This type of behavior is consistent with the kinetic energy distribution measured by Sonnenfroh and Farrar (SF)[17] at 0.57 eV but disagrees with the ICR results of RPB[12] at thermal energies. However, the fall-off behavior of the present data is not inconsistent with significant contributions of more direct reaction mechanisms. For instance, if reaction (4.1a) were occurring via the nonstatistical spectator stripping model,[28] product dissociation would be delayed only until E_S = 6.5 eV.

4.3.5 O^+ + CO: High Energies

For reaction (4.1b), the cross section decline over the range $6 \leq E_0 \leq 11$ eV can be reproduced by $\sigma(E_0) = (45 \pm 40)\ E_0^{-3.0 \pm 1.0}\ Å^2$. This decline is an interesting phenomenon since the O^+ product clearly cannot dissociate. It is possible that competition with the O_2^+ + C reaction channel is responsible, but reaction (4.1c) begins well before the sharp decline in reaction (4.1b) and, as discussed above, reaction (4.1c) appears to compete primarily with reaction (4.1a). A more likely

explanation is competition with reaction (4.6a), direct collision induced dissociation of O_2 by C^+.

At slightly higher energies, the decline in the O^+ cross section is reversed, and formation of O^+ increases. This increase must be due to reaction (4.6b) and could result from dissociation of CO^+ or from dissociative charge transfer, i.e. dissociation of O_2^+. The production of O^+ in this energy range can be further analyzed by subtracting the numerical fit given above for the decline of the cross section between 6 and 11 eV from the data and then analyzing the result in a similar manner as the threshold for $O_2^+ + C$. Again, the line-of-centers form, equation (4.5), reproduces the data very nicely. The threshold energy obtained from this analysis is 10.8 ± 0.8 eV. This is considerably above the thermodynamic threshold for process (4.6b). This could be because this process occurs via formation of CO^+ in a stripping-type mechanism such that dissociation is predicted to be delayed until $E_s = 9.5$ eV, equation (2.12). Another possibility is that the CO^+ or O_2^+ precursor to the O^+ product is formed in an excited state which decomposes with the release of kinetic energy. For example, $O_2^+(B^2\Sigma_g^-)$, 8.23 eV above the ground state,[29] can be formed beginning at a kinetic energy of 9.04 eV and is known to predissociate from photo-ionization studies.[30] A final mechanism is that the products corresponding to the observed reaction are not ground state species. Indeed, production of $C(^3P) + O(^3P) + O^+(^2D)$ has a thermodynamic threshold of 10.80 eV, in good agreement with the apparent experimental threshold.

4.4 DISCUSSION

One of the more interesting and controversial aspects of reaction (4.1) is the reaction mechanism. Based on their crossed beam results for reaction (4.1a) at a collision energy of 0.57 eV, Sonnenfroh and Farrar (SF)[17] hypothesize the existence of a long-lived CO_2^+ intermediate formed by C^+ insertion into O_2. They conclude that the CO_2^+ reaction intermediate has a lifetime of ~ 0.5 ps, somewhat shorter than a rotational period. In contrast, Rincon, Pearson, and Bowers (RPB)[12] conclude that both reaction (4.1a) and (4.1b) are nonstatistical based on their kinetic energy release measurements. To explain their results, both SF and RPB utilize adiabatic state correlation diagrams; however, SF utilize a diagram derived from C_{2v} symmetry (which leads to ground state carbon dioxide ions), while RPB prefer a near-collinear geometry reaction. In the discussion which follows, the state-specific reactions involved in process (4.1) are first identified. Statistical theories are then evaluated to see if they can reproduce the observed results. Finally, the potential energy surfaces for both types of reaction geometries are examined in detail.

The state-specific reactions

$$C^+(^2P_u) + O_2(X^3\Sigma_g^-) \rightarrow CO^+(X^2\Sigma^+) + O(^3P_g) \qquad \Delta H^\circ = -3.24 \text{ eV} \qquad (4.1a)$$

$$\rightarrow O^+(^4S_u) + CO(X^1\Sigma^+) \qquad \Delta H^\circ = -3.64 \text{ eV} \qquad (4.1b)$$

$$\rightarrow O_2^+(X^2\Pi_g) + C(^3P_g) \qquad \Delta H^\circ = +0.81 \text{ eV} \qquad (4.1c)$$

$$\rightarrow CO^+(X^2\Sigma^+) + O(^1D_g) \qquad \Delta H^\circ = -1.27 \text{ eV} \qquad (4.1d)$$

$$\rightarrow CO^+(A^2\Pi) + O(^3P_g) \qquad \Delta H^\circ = -0.67 \text{ eV} \qquad (4.1e)$$

$$\rightarrow O^+(^2D_u) + CO(X^1\Sigma^+), \qquad \Delta H^\circ = -0.32 \text{ eV} \qquad (4.1f)$$

are the lowest energy product channels for process (4.1).[1,29] Emission from $CO^+(A^2\Pi)$ has been observed at thermal energy by Tsuji *et al.*[4] and at elevated energies (3.6 eV) by Ottinger and Simonis;[13] however, Ottinger and Simonis have estimated that the cross section for $CO^+(A^2\Pi)$ formation is only ~ 0.01 $Å^2$ at 3.6 eV, while the present total CO^+ cross section at this energy is ~ 2.5 $Å^2$. This is consistent with the study of RPB who find no evidence for excited state products and place upper limits of 5, 2 and 1% for reactions (4.1d), (4.1e), and (4.1f), respectively. Thus, all available evidence indicates that formation of electronically excited products are minor processes. The discussion which follows is therefore restricted to the state-specific reactions (4.1a), (4.1b) and, to a lesser extent, (4.1c).

4.4.1 Phase Space Calculations

In order to determine if the energy dependencies of reactions (4.1a) - (4.1c) are due to statistical effects, atom-diatom phase space theory (PST) calculations[31] were carried out using modified versions of computer programs originally developed by Chesnavich and Bowers.[32] For reaction (4.1a), the calculated cross sections display the same $E^{-0.5}$ energy dependence as do σ(4.1a) and σ_{LGS}, i.e. the energy dependence of reaction (4.1a) is reasonably well described by PST up to the dissociation limit. This is consistent with the observation that dissociation of the CO^+ product begins at the thermodynamic limit for reaction (4.6a) and with the conclusions of SF that this reaction occurs via a long-lived collision complex. The magnitude of the PST results are much larger than the experimental cross section if all of the potential energy surfaces associated with the reactants are presumed to lead to efficient formation of

products. For the $C^+(^2P) + O_2(^3\Sigma_g^-)$ reactant channel, there exist 18 total surfaces (3 doublets and 3 quartets). The best reproduction of the $CO^+ + O$ cross section is obtained if only 4 out of the 18 surfaces (4/18 = 0.22) are assumed to lead to reaction (4.1a). This is consistent with the fact that the magnitude of the experimental cross section is $(0.23 \pm 0.03)\sigma_{LGS}$.

The PST cross section for reaction (4.1b) also behaves as $E^{-0.5}$, in contrast to the E^{-1} behavior observed experimentally. This makes it clear that reaction (4.1b) is not statistically behaved, in keeping with the conclusions of RPB. One possible explanation for this type of energy dependence is that the reaction occurs via a curve crossing, along the lines of what was observed for $O^+ + N_2$ in Chapter 3.[33] The E^{-1} energy dependence results from multiplying the $E^{-0.5}$ energy dependence of the LGS collision cross section[19] by an approximate $E^{-0.5}$ energy dependence for the Landau-Zener probability of a transition between two potential energy surfaces.[34] (An exact $E^{-0.5}$ transition probability occurs only if the potential energy at the crossing point is zero.) In the case of the $O^+ + N_2$ system, the crossing is spin-forbidden and consequently quite inefficient (<0.3% of the collision rate at thermal energies).[33] The large magnitude of the $O^+ + CO$ cross section at low energies indicates that if a surface crossing is involved, then the surfaces are much more strongly coupled than in the $O^+ + N_2$ system. It is therefore unlikely that a spin-changing reaction plays a significant role here.

For reaction (4.1c), the PST cross section rises more slowly than the data, Figure 4-5. This suggests that the charge transfer reaction occurs preferentially in a

direct, large impact parameter process rather than via a long-lived intermediate. As can be seen in Figure 4-5, the magnitude of the PST cross section can reproduce the experimental result at higher energies. To obtain this calculated magnitude, it is necessary to assume that 12 of the 36 potential energy surfaces evolving from $O_2^+(^2\Pi)$ + $C(^3P)$ are reactive.

4.4.2 Electronic State Correlations

To explain the results for reaction (4.1), it is necessary to have an appreciation for the potential energy surfaces involved. Unfortunately, this is a reasonably complex system involving many surfaces and surface crossings. Calculations are available for the surfaces of CO_2^+ (carbon dioxide ion) and its dissociation to $[CO + O]^+$,[35,36] but not for its dissociation to $[C + O_2]^+$. As RPB have pointed out, entrance channel effects may be very important in this reaction. These effects shall now be qualitatively explored.

As noted above, 3 doublet and 3 quartet surfaces evolve as the reactants approach. For a collision having $C_{\infty v}$ (C_{2v}, C_s) symmetry, there will be $^{2,4}\Sigma^-$ (B_1, A"), $^{2,4}\Pi$ (A_2, A"), and $^{2,4}\Pi$ (A_1, A') surfaces. One of these quartet surfaces evolves adiabatically to the single quartet surface which correlates with O^+ + CO products, $^4\Sigma^-$ (B_1, A"). The other 2 quartet surfaces and the 3 doublet surfaces correlate adiabatically with the products of reaction (4.1a). This simple adiabatic correlation scheme has been given by Tsuji *et al.*[4] and RPB.[12] Note that the CO^+ + O product channel is highly favored in terms of the number of adiabatic surface correlations. This is in stark contrast to the experimentally observed branching ratio at thermal

energies. To explain this discrepancy, it is necessary to consider the potential energy surfaces of the reaction in more detail.

To provide qualitative information concerning the attractiveness or repulsiveness of the surfaces at long range, consider first the diabatic surface correlations. Although no calculations are available on this region, qualitative molecular orbital (MO) ideas can be used to help elucidate the surface characteristics. These ideas have been previously discussed in detail for the analogous $C^+ + H_2$ reaction.[37] The Appendix provides a detailed account of the present case and the results are shown in Figure 4-6. The characteristics of the surfaces change depending on whether the $C^+(2p)$ orbital occupied is the p_x, p_y, or p_z (the convention used here is that the z axis is along the direction of approach, the x axis is in the plane of the three atoms, and the y axis is perpendicular to the plane). These atomic orbitals lead to the $^{2,4}\Pi$ (A_2, A"), $^{2,4}\Pi$ (A_1, A'), and $^{2,4}\Sigma^-$ (B_1, A") surfaces, respectively.

4.4.3 Doublet Surfaces

It can be seen that for a C_{2v} approach on the doublet surfaces, Figures 4-6a and 4-6b, the $^2A_1$ and $^2B_1$ surfaces are expected to be repulsive at long range, while the $^2A_2$ surface is initially attractive. This latter surface correlates with ground state $CO_2^+(X^2\Pi_g)$ and then on to ground state products, $CO^+(X^2\Sigma^+) + O(^3P)$. Note that even if the symmetry of the reaction is reduced to C_s [i.e., crossings between A' (A_1 and B_2) or A" (B_1 and A_2) surfaces become avoided], only 1 of the 3 doublet surfaces leads to products without an appreciable activation barrier. In $C_{\infty v}$ symmetry, however, only the $^2\Sigma^-$ surface is repulsive. The $^2\Pi$ surfaces lead diabatically to

excited state products, $O^+(^2D) + CO(X^1\Sigma^+)$, exothermic by 0.32 eV. These surfaces have avoided crossings with the $^2\Pi$ surfaces evolving from $CO^+(X^2\Sigma^+) + O(^3P)$ such that there is a low energy pathway to form ground state $CO^+ + O$ products on 2 of the 3 doublet surfaces.

The nature of the $^2\Pi$ surfaces is an attractive explanation for several experimental observations. These surfaces provide an efficient path for reaction (4.1a) on 4 out of the 18 surfaces evolving from reactants, consistent with the PST results. On one of these doublet surfaces, the reaction can easily gain access to ground state CO_2^+, and even if $C_{\infty v}$ symmetry is maintained, there may be a potential well for the intermediates. This could explain the appreciable forward - backward scattering symmetry in the beam experiments of SF. The fact that the forward scattered component dominates may be a reflection that reaction on the $^2\Pi$ ($^2A_1$) surface is more direct than reaction on the $^2\Pi$ ($^2A_2$) surface. Also, the qualitative character of the collinear $^2\Pi$ surfaces shows that kinetic energy could be released as the $[C\text{-}O\text{-}O]^+$ intermediate decomposes to $CO^+ + O$. This could explain the observation of RPB that the vibrational distributions of the CO^+ product appear somewhat non-statistical at thermal energies. This observation contrasts with the observation by SF of a statistical kinetic energy distribution at higher reactant energies.

4.4.4 Quartet Surfaces

To explain reaction (4.1b), it is necessary to consider the quartet surfaces, Figure 4-6c, especially since spin-changing reactions are discounted. For a C_{2v} approach on the quartet surfaces, the interaction is probably repulsive in the entrance

channel for all three surfaces. While this is probably the most likely scenario, it is possible that the ion-induced dipole attraction is sufficient to overcome this repulsion for the $^4A_2$ surface, the least repulsive approach. This surface crosses the $^4B_1$ surface (a crossing which becomes avoided in C_s symmetry) which in turn leads to CO_2^+ ($^4B_1$, $a^4\Pi_u$), the lowest lying quartet state of CO_2^+. This state correlates adiabatically to $CO^+(X^2\Sigma^+) + O(^3P)$ in $C_{\infty v}$ symmetry, but in C_s symmetry, the crossing between the $a^4\Pi_u$ ($^4A''$) and $^4\Sigma_g^-$ ($^4A''$) surfaces becomes avoided such that $O^+(^4S) + CO(X^1\Sigma^+)$ products should be produced. Indeed, Lorquet and coworkers[35] have examined this crossing carefully and verify that the lowest energy pathway to form $O^+ + CO$ products is in C_s symmetry. (The calculated energy of this crossing in $C_{\infty v}$ symmetry is correctly indicated in Figure 4-6c.)

A more likely pathway for producing $O^+ + CO$ is a collinear reaction geometry. As with the doublet surfaces, the $^4\Sigma^-$ surface should be strongly repulsive. The $^4\Pi$ surfaces should be somewhat attractive (although not as attractive as the $^2\Pi$ surfaces), but they correlate with highly excited product states. Consequently, it is anticipated that the $^4\Pi$ surfaces become repulsive at short range before they cross the $^4\Pi$ surfaces evolving from $CO^+ + O$. However, the $^4\Pi$ ($^4A''$) surface should cross the $^4\Sigma^-$ ($^4A''$) surface evolving from $O^+(^4S) + CO(X)$. In C_s symmetry, this crossing becomes avoided such that a low energy pathway for reaction (4.1b) is provided on a single quartet surface.

This qualitative surface can be used to explain several experimental observations. The approach of the C^+ and O_2 molecules is most attractive in $C_{\infty v}$

symmetry and probably fairly repulsive if the C^+ and O_2 approach is too far off collinear. However, the $^4\Pi$ - $^4\Sigma^-$ surface crossing demands C_s symmetry if it is to be an avoided crossing. Thus, the most favorable reaction geometry is highly restricted and involves a surface crossing. This combination is probably sufficient to explain the observed E^{-1} energy dependence of reaction (4.1b). Note that this process occurs on surfaces which are distinct from those for reaction (4.1a). This can explain why no direct competition between the two reactions is observed. Also, the character of the reactive $^4A''$ surface is consistent with the conclusion of RPB that the reaction is non-statistical.

4.4.5 Branching Ratio and Reaction Efficiency

Finally, consider the ability of these surfaces to explain the observed branching ratio, 60:40, and the overall reaction probability, 0.76 ± 0.23 at 300 K. As outlined above, reaction (4.1a) can occur on 2 doublet surfaces while reaction (4.1b) occurs on 1 quartet surface. Statistically, this predicts a branching ratio of 50:50 and a reaction probability of $8/18 = 0.44$. It is interesting to note that this situation actually exists at $\sim$ 0.15 eV. The failure of this prediction at thermal energies suggests that additional surfaces couple to the reactive ones at the lowest kinetic energies. For example, if the repulsive $^4\Sigma^-$ ($^4A''$) surface couples to the attractive $^4\Pi$ ($^4A''$) surface as the C^+ and O_2 approach, and likewise, the $^2\Sigma^-$ ($^2A''$) surface couples to the $^2\Pi$ ($^2A''$) surface, then the overall reaction probability can climb to $14/18 = 0.78$ and the branching ratio goes to 57:43 in favor of the $O^+ + CO$ channel (assuming the 2 quartet surfaces lead to $O^+ + CO$ and the 3 doublet surfaces lead to $CO^+ + O$). In

this scenario, only the $^4A'$ surface is unreactive at the lowest energies. This hypothesis is supported by a close examination of the reaction efficiency for process (4.1a). As noted above, the efficiency is 0.23 over the energy range of 0.1 to 1.0 eV (and up to 4 eV if reaction (4.1c) is included). However, it rises to 0.31, Figure 4-3, at the lowest energies, consistent with the prediction of 6/18 = 0.33. If this hypothesis is correct, then the low energy behavior of reaction (4.1a) suggests that the coupling between the $^2\Sigma^-$ and $^2\Pi$ surfaces decreases rapidly with increasing kinetic energy.

4.5 CONCLUSION

Guided ion beam mass spectrometry has been used to examine the kinetic energy dependence of the reaction of ground state atomic carbon ion with molecular oxygen from thermal energies to 35 eV. The total cross section is found to approach to within 75% of the prediction of the Langevin-Gioumousis-Stevenson model[19] at the lowest energy examined, 0.05 eV, but it falls more rapidly than LGS model as the energy is increased. At thermal energies, the observed branching ratio is 60% (O^+ + CO) and 40% (CO^+ + O), in excellent agreement with previous studies. This branching ratio declines steadily with increasing energy such that above 0.14 eV, CO^+ + O is the preferred product channel. Thermal rate constants obtained from integration of the total cross section results give results slightly lower than most previous measurements, although within experimental error. The small discrepancies may be due to reactions of excited state ions in the earlier studies. Analysis of the

endothermic O_2^+ + C channel using a simple, line-of-centers model results in a threshold energy of 0.82 eV, in excellent agreement with the known thermochemistry.

Agreement between the experimental cross sections and those predicted by phase space theory is good for the CO^+ + O reaction, reasonable at elevated energies for the O_2^+ + C channel, and very poor for the O^+ + CO process. Experimental evidence suggests that the first two channels are coupled with one another while the latter channel appears to be almost completely decoupled. The potential energy surfaces for this reaction are qualitatively described and used to rationalize the behavior observed in this and other experiments. This analysis suggests that reaction (4.1a) occurs at most kinetic energies via a stable intermediate which can be accessed on 2 doublet surfaces. Reaction (4.1b), in contrast, occurs primarily on a single quartet surface via a restricted collinear approach. At the lowest kinetic energies, additional doublet and quartet surfaces may couple to the reactive ones. Accurate theoretical calculations on these surfaces are needed to provide a test of the mechanism proposed here and should yield additional insight into this reaction.

4.6 APPENDIX: Molecular Orbital Correlations and Potential Energy Surfaces

In order to characterize the potential energy surfaces of reaction (4.1), it is useful to consider the molecular orbital (MO) correlation diagram shown in Figure 4-7. Energies for $[C + O_2]^+$, $[CO + O]^+$, and OCO^+ are taken from experimental results on these species and their excited states.[1,29] The energies for bent OCO^+ are derived from the calculations of Praet *et al.*[35] for an angle of 120°. The relative energies shown for the molecular orbitals of linear vs. bent OCO^+ are consistent with qualitative expectations (Walsh's rules).[38] The most significant of these changes are the strongly attractive nature of the $3a_1$ orbital and the strongly repulsive nature of the $4a_1$ orbital as the molecule is bent. In considering the progression from reactants to intermediates along the C_{2v} pathway, two striking results are the diabatic correlation of C(2s) with $CO_2^+(4a_1)$ and that of $C^+(2p_x)$ with $CO_2^+(1b_2)$. These show that $C^+(^2P)$ + $O_2(^3\Sigma^-)$ diabatically correlates with a very highly excited state of CO_2^+ no matter what the $C^+(2p)$ occupancy is. Note that the situation is no better in $C_{\infty v}$ symmetry since the $C^+(2p_\sigma)$ orbital diabatically correlates with $CO(\sigma^*)$, leading again to excited states of the products. Clearly, adiabatic surface crossings must exist for reaction (4.1) to occur. The corresponding avoided crossings in the MO correlation diagram are indicated in Figure 4-7. One such interaction is that between $CO(\sigma)$ and $O(2p_\sigma)$, which lie close in energy. Because of the proximity of these orbitals, all further discussion assumes that they are highly mixed.

Even when the adiabatic MO correlations are considered, the C_{2v} approach leads to highly excited CO_2^+ intermediates for two reasons: one of the $O_2(\pi_u)$

molecular orbitals correlates with $CO_2^+(3a_1, \pi_u^*)$ leading to *double* occupancy of an antibonding MO, and the *singly* occupied $O_2(\pi_g)$ MO correlates with $CO_2^+(1b_2, \sigma_u)$, a strongly bonding MO. Overall, the attractiveness of the surfaces are probably somewhat better in $C_{\infty v}$ symmetry since the $O_2(\pi_u)$ MO correlates directly with $CO(\pi)$ and $O_2(\pi_g)$ correlates with $O(2p_\pi)$.

4.6.1 C_{2v} Symmetry: Doublet Surfaces

Now consider the occupancy of the $C^+(2p)$ orbital. In C_{2v} symmetry, if the $C^+(2p)$ electron is in the p_x orbital, a $^2A_2$ surface will be generated, Figure 4-6a. In the entrance channel, the $C^+(2p_x)$ electron interacts with the singly occupied in-plane antibonding π_g MO of O_2 since these both have b_2 symmetry. This interaction leads to a doubly occupied $CO_2^+(1b_2)$ orbital and therefore the surface should be initially attractive. At closer distances, this surface probably becomes repulsive since the $CO_2^+(3a_1, \pi_u^*)$ orbital is doubly occupied. However, this surface must interact with another $^2A_2$ surface evolving from $CO_2^+(X^2\Pi_g)$, 8.9 eV below reactants. This interaction corresponds to moving the 2 electrons in the $3a_1$ MO into the $2b_2$ MO. These surfaces presumably avoid one another such that, adiabatically, a low energy pathway from reactants to $CO_2^+(X)$ is formed. In the exit channel, $CO_2^+(X)$ correlates directly with $CO^+(X) + O(^3P)$ products in all symmetries.

The $C^+(2p_y)$ electron interacts with the doubly occupied out-of-plane π_u bonding MO of O_2 (b_1 symmetry). This leads to a moderately repulsive $^2A_1$ surface in the entrance channel, Figure 4-6b. Note that this surface may cross another of the same symmetry which evolves from $O_2^+(^2\Pi) + C(^3P)$. This interaction corresponds

to moving the electron in the $O_2(\pi_g, b_2)$ MO into the $C(2p_x, b_2)$ orbital. This is presumably one low energy pathway for reaction (4.1c). Eventually, the $^2A_1$ surface evolving from reactants leads to adiabatic formation of $CO_2^+(A^2\Pi_u)$, 3.5 eV higher than $CO_2^+(X)$. In the product channel, $CO_2^+(A)$ correlates with excited state products, $CO^+(X) + O(^1D)$, in all symmetries. Note, however, that the $^2A_1$ surface crosses the $^2B_2$ surface evolving from $CO_2^+(X)$. This crossing can be avoided in C_s symmetry such that access to $CO_2^+(X)$ may be possible on this surface for some reaction geometries.

If the $C^+(2p)$ electron is in the p_z orbital, it interacts with the doubly occupied in-plane π_u MO of O_2 (a_1 symmetry). This yields a very repulsive $^2B_1$ surface at long range, Figure 4-6a. This surface may also cross another of the same symmetry evolving from $O_2^+(^2\Pi) + C(^3P)$, again an $O_2(\pi_g)$ - $C(2p_x)$ interaction, yielding another low energy pathway for reaction (4.1c). This $^2B_1$ surface eventually correlates with $CO_2^+(A^2\Pi_u)$. Note that if symmetry is reduced to C_s in the entrance channel, the $^2B_1$ and $^2A_2$ surfaces can interact. However, since they cross twice, the overall correlations are not changed. In the product channel, $CO_2^+(A)$ correlates with excited state products, $CO^+(X) + O(^1D)$, in $C_{\infty v}$ symmetry; but if symmetry is reduced to C_s in the exit channel, there can be an avoided crossing with a $^2\Sigma^-$ surface evolving from $CO^+(X) + O(^3P)$.

4.6.2 C_{2v} Symmetry: Quartet Surfaces

Using similar considerations to those for the doublet surfaces, $^4B_1$, $^4A_1$, and $^4A_2$ surfaces are found to evolve from reactants, Figure 4-6c. The $^4A_2$ surface

[corresponding to $C^+(2p_x)$] is expected to be the least repulsive of the three, but since there is no covalent bonding interaction between C^+ and O_2 (the $1b_2$ and $2b_2$ MOs are singly occupied), this surface is probably repulsive at long range. Since the $^4A_2$ surface has not been identified in any previous calculations, it presumably lies at high energies. This surface must eventually correlate adiabatically with a $^4\Sigma^-$ surface evolving from $CO^+(X) + O(^3P)$. The $^4B_1$ and $^4A_1$ surfaces should be repulsive at long range and adiabatically correlate to a $CO_2^+(a^4\Pi_u)$ intermediate, calculated to be 6.9 eV above $CO_2^+(X)$.[35] These calculations also indicate that the $^4A_1$ surface lies higher in energy than the reactants as the C^+ approaches (~ 1 eV higher when the O-C-O angle is 100° and the CO distances are fixed at 1.16 Å). In contrast, the $^4B_1$ surface is bound more strongly at intermediate C^+ - O_2 distances than collinear $CO_2^+(a)$ (~ 2.5 eV lower when the O-C-O angle is 120° and the CO distances are fixed at 1.16 Å). In $C_{\infty v}$ symmetry, the $CO_2^+(a)$ intermediate correlates with $CO^+(X)$ + $O(^3P)$. However, this surface crosses the $^4\Sigma^-$ surface evolving from $O^+(^4S)$ + $CO(X^1\Sigma^+)$. In C_s symmetry, the $^4\Pi(A")$ - $^4\Sigma^-(A")$ crossing becomes avoided such that there is a low energy pathway from $CO_2^+(a)$ to O^+ + CO.

4.6.3 $C_{\infty v}$ Symmetry

In $C_{\infty v}$ symmetry, the p_x and p_y orbitals (π symmetry) will interact with the singly occupied $O_2(\pi_g)$ molecular orbitals. If doublet coupled, this interaction should be attractive. According to the MO correlation diagram, these $^2\Pi$ surfaces correlate with excited products, $O^+(^2D)$ + CO(X); however, they should have an avoided crossing with the $^2\Pi$ surfaces evolving from $CO^+(X) + O(^3P)$. If quartet coupled, the

$C^+ + O_2$ interaction will be less attractive, although at long range, the ion-induced dipole forces should predominate. At short range, the $^4\Pi$ surfaces must be repulsive since they lead to occupation of the $CO(\pi^*)$ MO, Figure 4-7. These surfaces should also have an avoided crossing with surfaces evolving from $CO^+(X) + O(^3P)$.

If the p_z orbital (σ symmetry) is occupied, the interaction with O_2 should be very repulsive since the p_z orbital diabatically correlates with the $CO(\sigma^*)$ MO, Figure 4-7. The $^2\Sigma^-$ and $^4\Sigma^-$ surfaces will have avoided crossings with surfaces evolving from $CO^+(X) + O(^3P)$ and $O^+(^4S) + CO(X)$, respectively. If $C_{\infty v}$ symmetry is broken, the doublet and quartet $\Sigma^-(A")$ surfaces can interact with the doublet and quartet $\Pi(A")$ surfaces. The energies at which the Σ^- and Π surfaces cross are unknown.

4.7 REFERENCES

1. Reaction enthalpies correspond to formation of products in their ground electronic states at T = 0 K and are based on tabulated heats of formation [M. W. Chase, Jr., C. A. Davies, J. R. Downey, Jr., D. J. Frurip, R. A. McDonald, and A. N. Syverud, J. Phys. Chem. Ref. Data **14**, Supp. 1 (1985); H. M. Rosenstock, K. Draxl, B. W. Steiner, and J. T. Herron, J. Phys. Chem. Ref. Data **6**, Suppl. 1 (1977)].
2. F. C. Fehsenfeld, A. L. Schmeltekopf, and E. E. Ferguson, J. Chem. Phys. **45**, 23 (1966).
3. A. B. Rakshit, H. M. P. Stock, D. P. Wareing, and N. D. Twiddy, J. Phys. B: Atom. Molec. Phys. **11**, 4237 (1978).
4. M. Tsuji, T. Susuki, M. Endoh, and Y. Nishimura, Chem. Phys. Lett. **86**, 411 (1982).
5. St. Niccolini, D. Bassi, S. Iannotta, H. Villinger, R. Richter, A. Saxer, and W. Lindinger, Contributions to the Symposium on Atomic and Surface Physics, Salzburg, Austria, February 1982 (Universitat Innsbruck, Innsbruck, 1982), p. 291.
6. N. G. Adams and D. Smith, J. Phys. B: Atom. Molec. Phys. **9**, 1439 (1976).
7. D. Smith and N. G. Adams, Int. J. Mass Spectrom. Ion Phys. **23**, 123 (1977).
8. T. M. Miller, R. E. Wetterskog, and J. F. Paulson, J. Chem. Phys. **80**, 4922 (1984).

9. M. Tichy, A. B. Rakshit, D. G. Lister, N. D. Twiddy, N. G. Adams, and D. Smith, Int. J. Mass Spectrom. Ion Phys. **29**, 231 (1979).

10. S. Barlow and V. M. Bierbaum, private communication.

11. V. G. Anicich, W. T. Huntress, Jr., and J. H. Futrell, Chem. Phys. Lett. **40**, 233 (1976).

12. M. Rincon, J. Pearson, and M. T. Bowers, Int. J. Mass Spectrom. Ion Proc., in press.

13. C. Ottinger and J. Simonis, Phys. Rev. Lett. **35**, 924 (1975).

14. J. J. Leventhal, J. Chem. Phys. **55**, 4654 (1971).

15. R. C. C. Lao, R. W. Rozett, and W. S. Koski, J. Chem. Phys. **49**, 4202 (1968).

16. T. F. Moran and J. B. Wilcox, J. Chem. Phys. **68**, 2855 (1978).

17. D. M. Sonnenfroh and J. M. Farrar, Chem. Phys. Lett. **125**, 123 (1986).

18. R. S. Hemsworth, R. C. Bolden, M. J. Shaw, and N. D. Twiddy, Chem. Phys. Lett. **5**, 237 (1970). V. P. Warneck, Berichte Der Bunsen-Gesellschaft, **76**, 413 (1972). N. G. Adams, D. Smith, and D. Grief, Int. J. Mass Spectrom. Ion Phys. **26**, 405 (1978).

19. G. Gioumousis and D. P. Stevenson, J. Chem. Phys. **29**, 294 (1958).

20. J. O. Hirschfelder, C. R. Curtiss, and R. B. Bird, Molecular Theory of Gases and Liquids (John Wiley and Sons, New York, 1954), p. 950.

21. P. R. Kemper and M. T. Bowers, Int. J. Mass Spectrom. Ion. Proc. **52**, 1 (1983).

22. R. Derai, M. Mencik, G. Mauclaire, and R. Marx, Lecture Notes in Chemistry **31**, 272 (1982).

23. M. McEwan as reported in reference 12.

24. K. M. Ervin and P. B. Armentrout, J. Chem. Phys. **83**, 166 (1985).

25. R. D. Levine and R. B. Bernstein, Molecular Reaction Dynamics (Oxford University, New York, 1974), p. 46.

26. M. E. Weber, J. L. Elkind, and P. B. Armentrout, J. Chem. Phys. **84**, 1521 (1986).

27. The best fit between the present cross section data and the fall-off model presented in reference 26 corresponds to D = 5.2 $\pm$ 0.5 eV, f = 1.0, and p = 1.0. The parameters D = 6.0 $\pm$ 0.5 eV, f = 1.0, and p = 2.0 also provide a reasonable fit to the data.

28. A. Henglein and K. Lacmann, Adv. Mass Spectrom. **3**, 331 (1966); A. Henglein, in Ion - Molecule Reactions in the Gas Phase, edited by P. J. Ausloos (American Chemical Society, Washington, D.C., 1966), p. 63; A. Ding, K. Lacmann, and A. Henglein, Ber. Bunsenges. Phys. Chem. **71**, 596 (1967).

29. K. P. Huber and G. Herzberg, Constants of Diatomic Molecules (Van Nostrand Reinhold, New York, 1979).

30. J. Berkowitz, Photoabsorption, Photoionization, and Photoelectron Spectroscopy, (Academic Press, New York, 1979).

31. Phase space calculations on this system have been carried out previously [D. C. Fullerton and T. F. Moran, Int. J. Mass Spectrom. Ion Phys. **9**, 15 (1972).] Unfortunately, direct comparison of the present PST calculations to these earlier efforts is hampered because the results are plotted in a way which makes them difficult to read in the energy regions of interest here. In addition, they do not allow for any non-reactive surfaces. Therefore, no effort is made at the present time to compare the two sets of PST results.

32. W. J. Chesnavich and M. T. Bowers, J. Chem. Phys. **68**, 901 (1978).

33. J. D. Burley, K. M. Ervin, and P. B. Armentrout, J. Chem. Phys. **86**, 1944 (1987).

34. L. D. Landau, Phys. Z. Sowjetunion **2**, 46 (1932). C. Zener, Proc. R. Soc. London Ser. A **137**, 696 (1932).

35. M. T. Praet, J. C. Lorquet, and G. Raseev, J. Chem. Phys. **77**, 4611 (1982).

36. W. B. England, J. Chem. Phys. **77**, 6099 (1982). F. A. Grimm and M. Larsson, Physica Scripta **29**, 337 (1984). P. Roy, I. Nenner, P. Millie, P. Morin, and D. Roy, J. Chem. Phys. **84**, 2050 (1986).

37. K. M. Ervin and P. B. Armentrout, J. Chem. Phys. **84**, 6750 (1986).

38. C. J. Ballhausen and H. B. Gray, Molecular Orbital Theory, (Benjamin/Cummings, Reading, 1964).

TABLE 4-I

Thermal rate constants and branching ratios for reaction (4.1)

technique[a]	C^+ source	rate constant[b]	branching ratio[c]	reference
GIB	d(GS)	7.6 ± 2.3	60 : 40	this work
FA	e	11.0 ± 3.3	not reported	2
FA	f(GS)	9.0 ± 1.8	not reported	3
FD	g	7.5	65 : 35	5
SIFT	h	9.9	62 : 38	6
SIFT	i(>0.9 GS)	9.9 ± 2.0	62 : 38	7
SIFT	j(0.35 GS)	9.3 ± 2.3	62 : 38	8
SIFT	k(>0.9 GS)	7.4[m]	53 : 47	9
SIFT	f(GS)	not reported	60 : 40	10
TICR	f,n(GS)	12.2 ± 1.0	36 : 64	11
TICR	f(GS)	6.0	60 : 40	12
LGS		10.0		19

[a]GIB - guided ion beam; FA - flowing afterglow; FD - flow/drift tube; SIFT - selected ion flow tube; TICR - tandem ion cyclotron resonance; LGS - Langevin-Gioumousis-Stevenson model, equation (2.8).
[b]k(300) for reaction (4.1, total) in units of 10^{-10} cm^3 s^{-1}.
[c]Percentage ratio at thermal energies expressed in terms of $(O^+ + CO):(CO^+ + O)$.
[d]Electron impact/drift cell, yields 100% ground state (GS) ions.
[e]Microwave discharge into He/CO.
[f]Electron impact on He/CO, should yield 100% GS ions.
[g]Electron impact on He/CH_4.
[h]Microwave discharge into unspecified gas.
[i]Electron impact on CH_4, yields >90% $C^+(^2P)$, reference 23.
[j]Electron impact on CO_2, yields ~ 35% $C^+(^2P)$, reference 23.
[k]Electron impact on CO, yields >90% $C^+(^2P)$, references 9 and 23.
[m]Rate constant corrected for excited states.
[n]Kinetically hot ions.

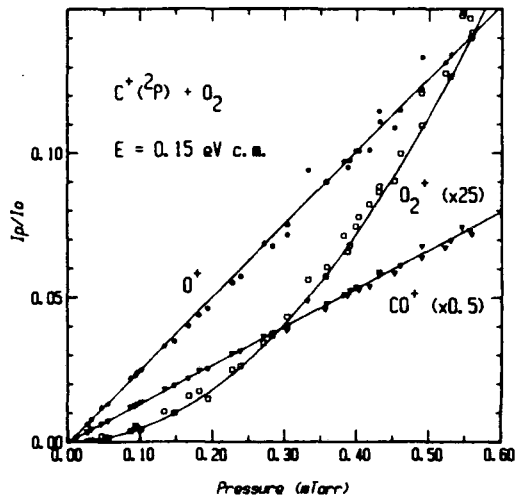

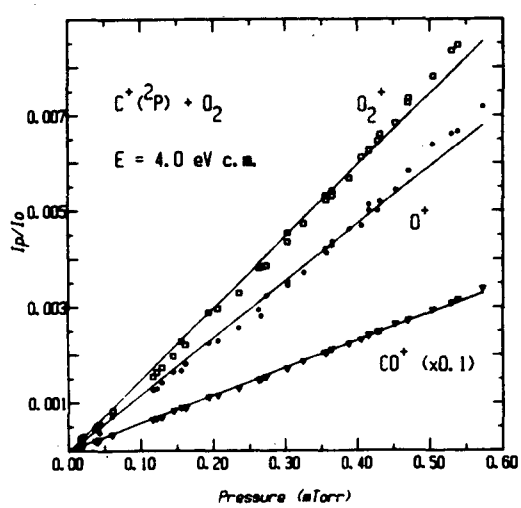

Figure 4-1. Ratio of product ion intensity to incident ion intensity, I_P/I_0, as a function of the gas cell pressure for reactions (4.1a, open triangles), (4.1b, filled circles), and (4.1c, open squares). In part a, the measurement is made at an interaction energy of 0.15 eV c.m.. The lines through the O^+ and CO^+ data are linear least squares fits. The line through the O_2^+ data is a quadratic fit. In part b, the measurement is made at an interaction energy of 4.0 eV c.m.. The lines are linear least squares fits to the data.

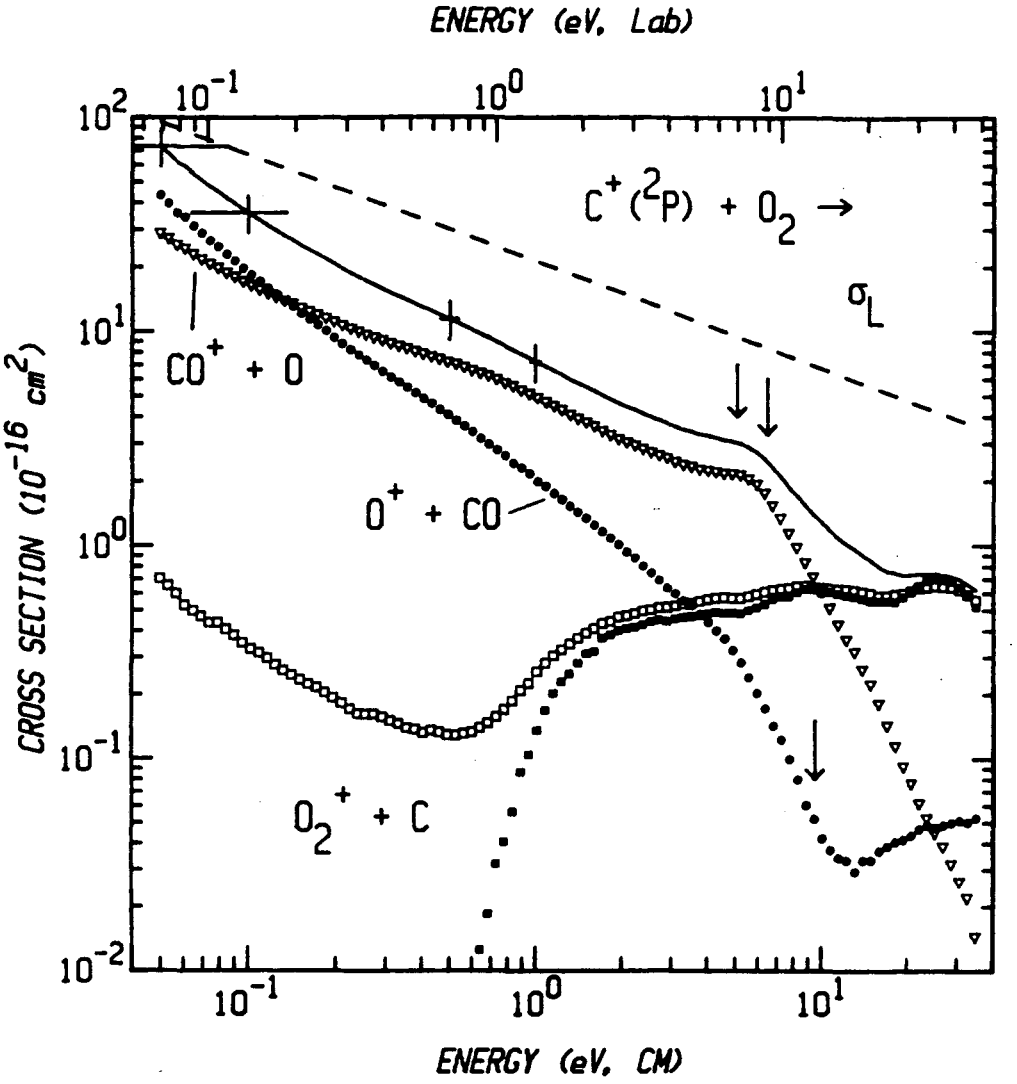

Figure 4-2. Cross sections for reactions (4.1a) - (4.1c) as a function of relative translational energy (lower scale) and laboratory energy (upper scale). The open triangles show the cross section for reaction (4.1a), and the filled circles show the cross section for reaction (4.1b). The cross sections for reaction (4.1c) are shown for an O_2 pressure of 0.22 mTorr (open squares) and for an extrapolated pressure of 0.0 mTorr (filled squares). The solid line indicates the total reaction cross section and the dashed line shows the LGS collision cross section. Error bars for both energy ($\pm$0.036 eV) and absolute magnitude ($\pm$20%) are given for the total cross section at selected energies. Arrows indicate the thermodynamic onset for dissociation of CO^+ at 5.1 eV, and the critical spectator stripping energy, E_s, for production of C^+ at 6.5 eV and of O^+ at 9.5 eV.

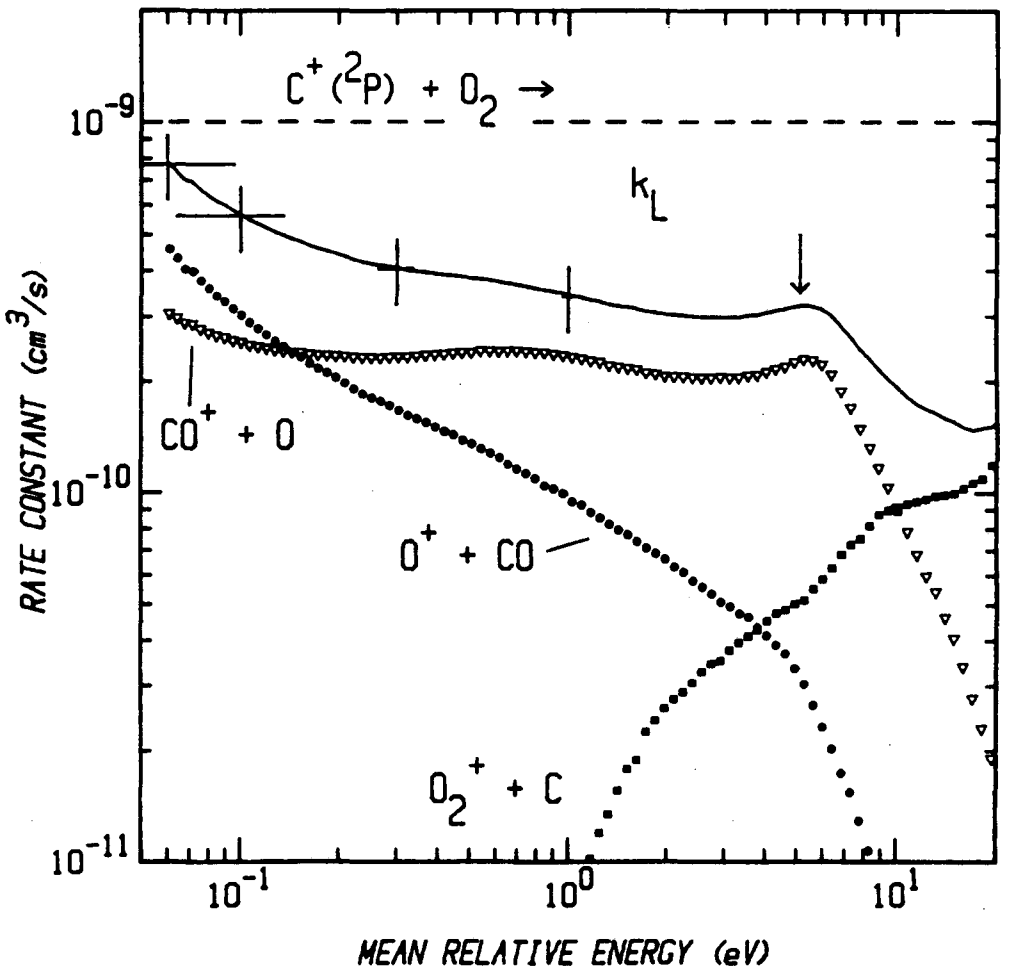

Figure 4-3. Phenomenological rate constants for reactions (4.1a) - (4.1c) as a function of the mean relative energy of the reactants, <E>. The data are derived from the cross sections of Figure 4-2 through the use of equation (2.7). Symbols are the same as for Figure 4-2. The LGS rate constant, equation (2.8), is given by the dashed line. Error bars for both energy ($\pm$0.036 eV) and absolute magnitude ($\pm$20%) are given for the total rate constant at selected energies. The arrow indicates the thermodynamic onset for dissociation of CO^+ at 5.1 eV.

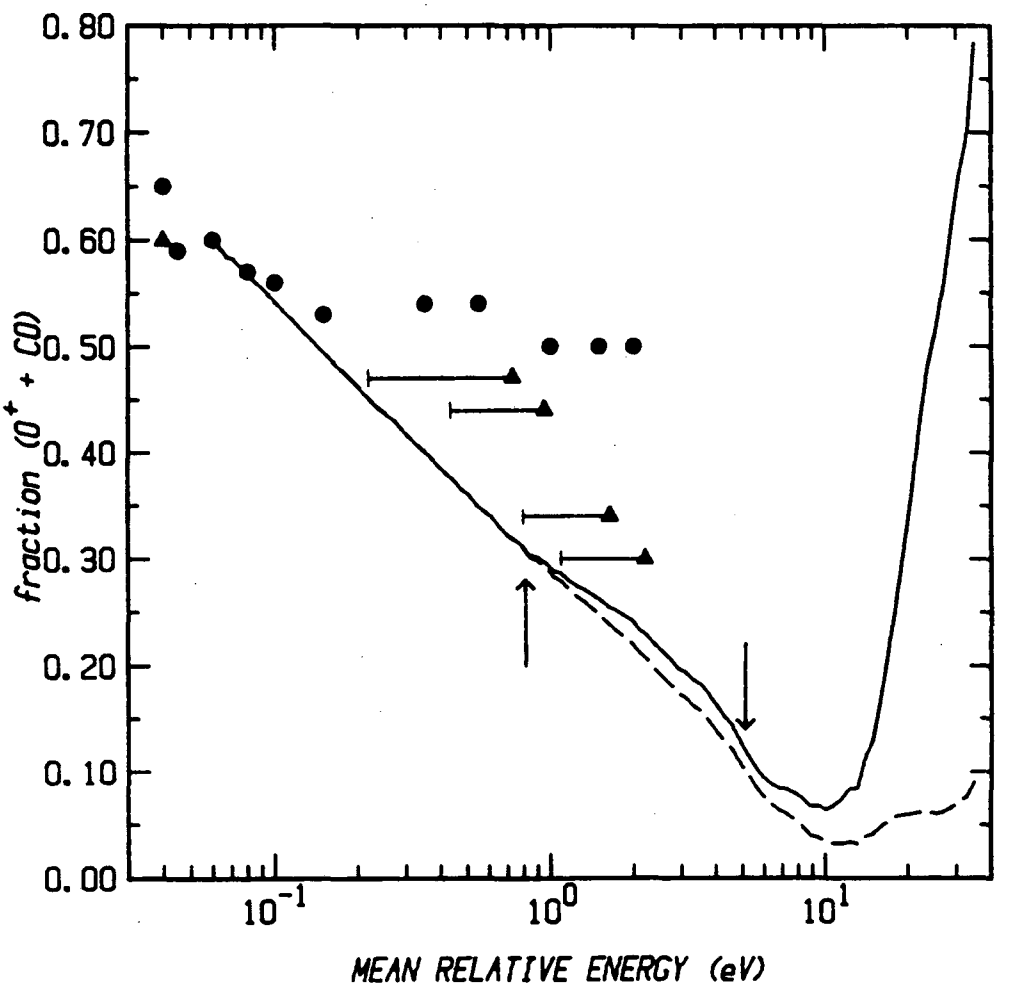

Figure 4-4. Branching ratio for reaction (4.1) as a function of the mean relative translational energy. The solid line shows the present results in terms of $\sigma(4.1b)/[\sigma(4.1b) + \sigma(4.1a)]$ and the dashed line shows $\sigma(4.1b)/\sigma(4.1, \text{total})$. Results of St. Niccolini *et al.* (reference 5) and Rincon, Pearson, and Bowers (reference 12) are shown by circles and triangles, respectively. Arrows indicate the threshold for reaction (4.1c) at 0.8 eV and for dissociation of CO^+ at 5.1 eV.

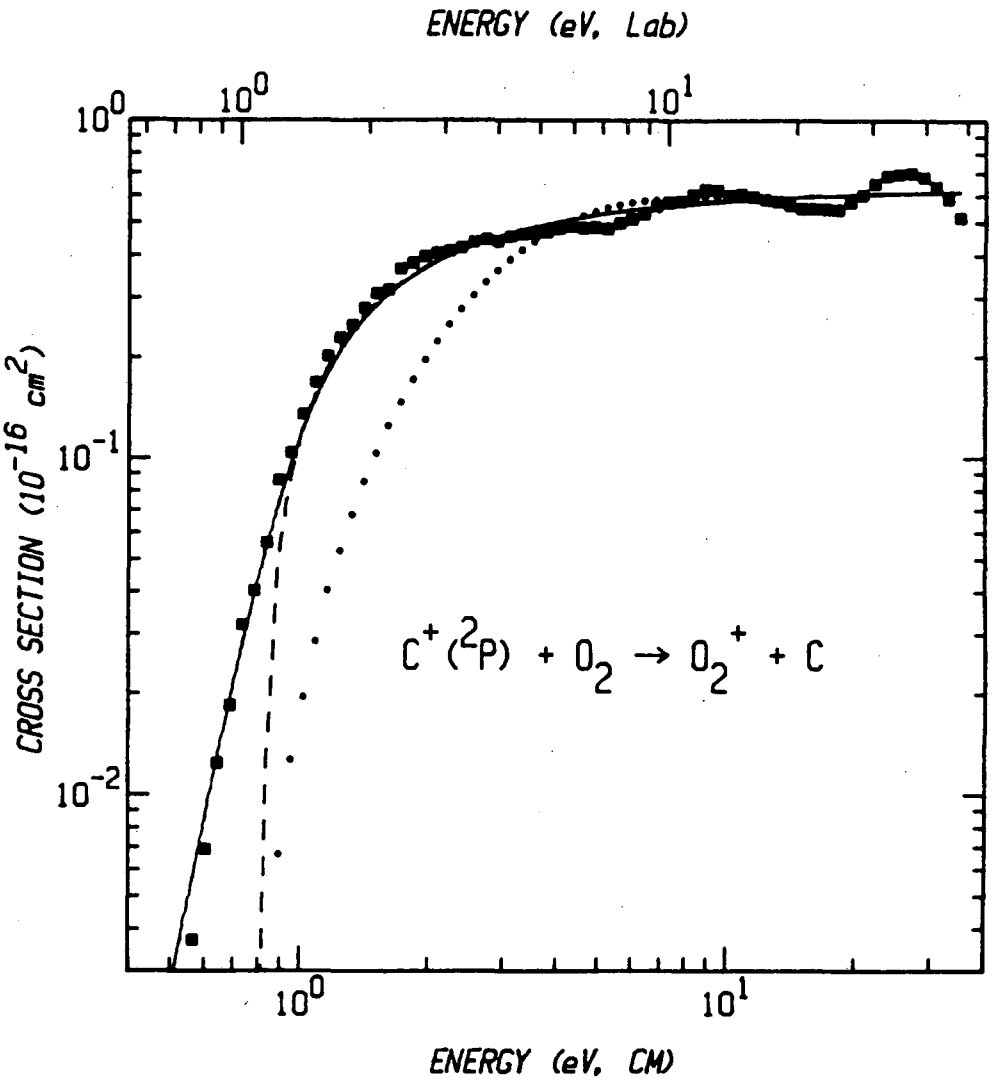

Figure 4-5. Cross sections for the charge transfer process, reaction (4.1c), as a function of the relative translational energy (lower scale) and the laboratory energy (upper scale). The data (filled squares) are the same as in Figure 4-2 (zero pressure extrapolation). The line-of-centers model discussed in the text is shown by the dashed line. The solid line shows this model convoluted over the experimental energy distributions. The cross section predicted by phase space theory is denoted by the dotted line.

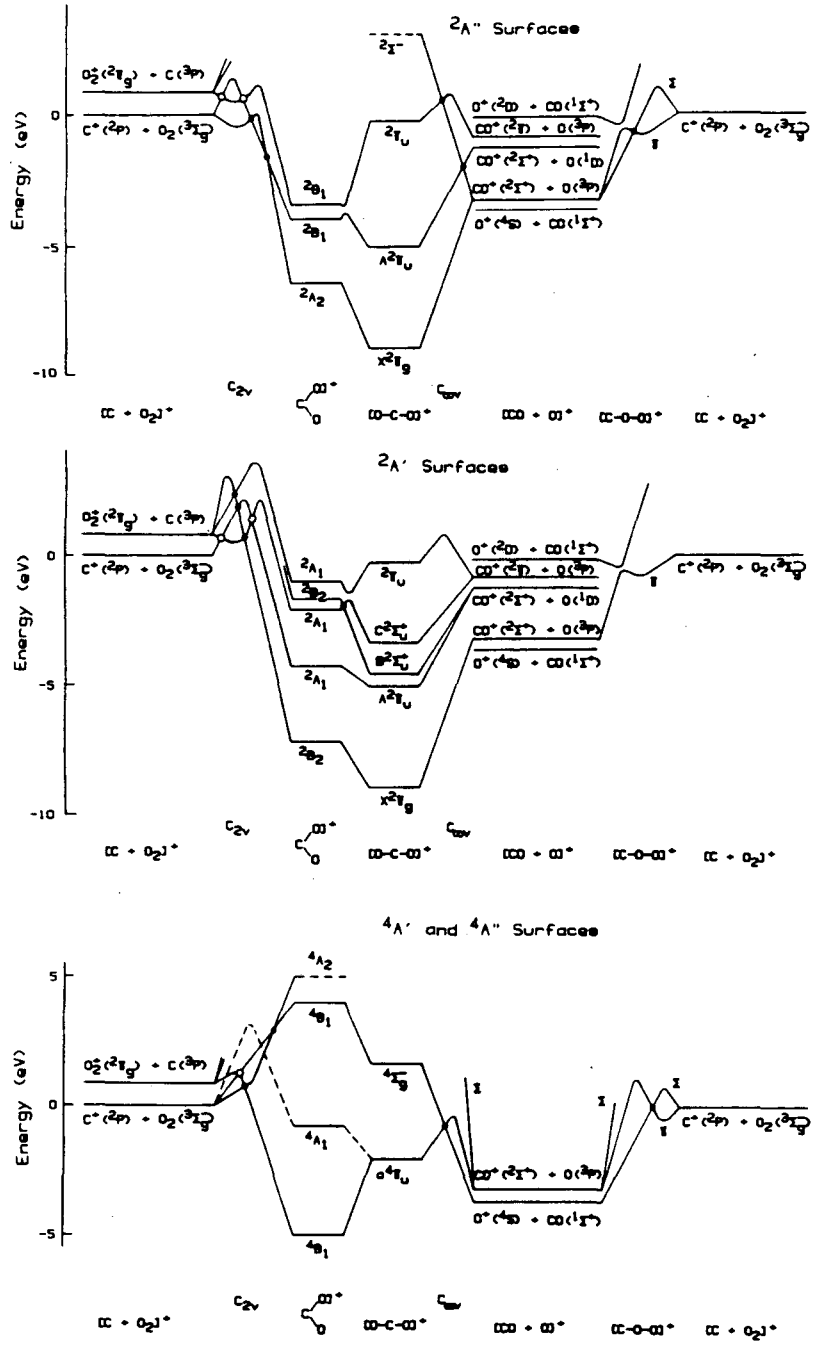

Figure 4-6. Semiquantitative electronic state correlation diagram for the $(C\text{-}O\text{-}O)^+$ system. Perpendicular approaches of C^+ and O_2 (C_{2v} symmetry) are shown on the left side and collinear approaches ($C_{\infty v}$ symmetry) are shown on the right. Parts a and b show doublet surfaces of A" and A' symmetry, respectively. Part c shows quartet surfaces of A" symmetry as solid lines and those of A' symmetry as dashed lines. Surface crossings which can become avoided in C_s symmetry are indicated by filled circles. Open circles indicate crossings between surfaces of the same symmetry evolving from $[C^+ + O_2]$ and from $[C + O_2^+]$.

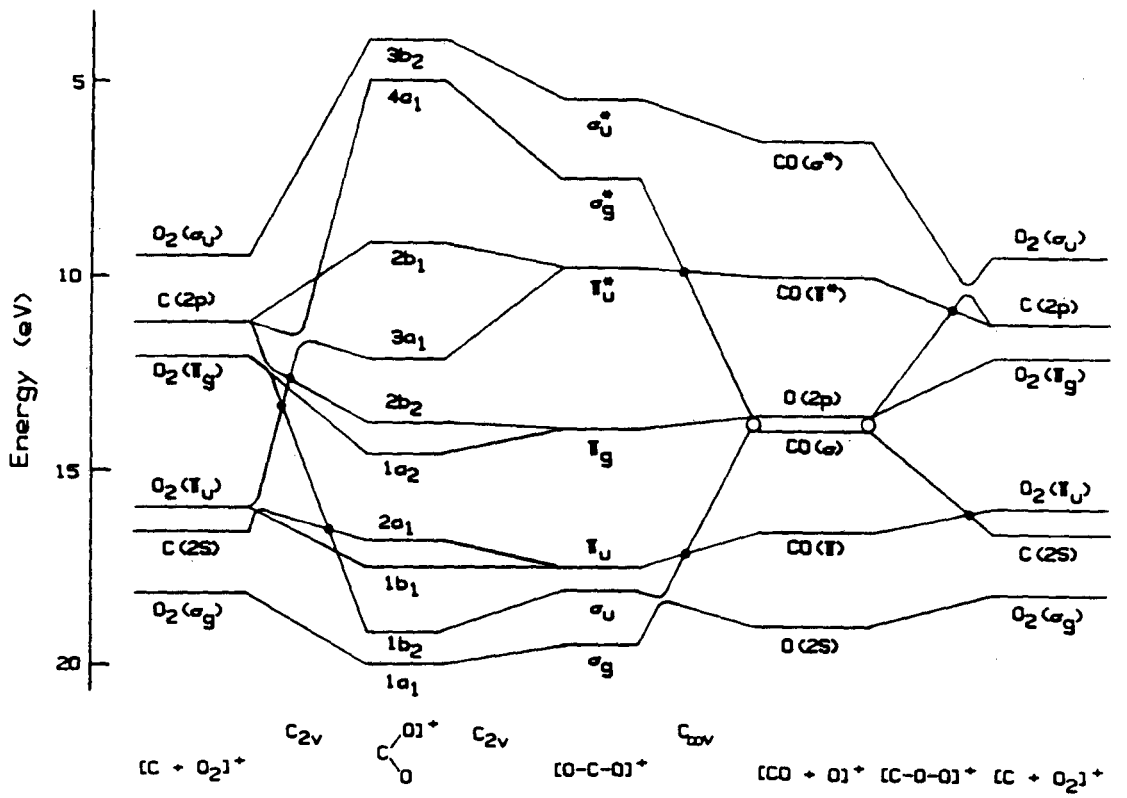

Figure 4-7. Semiquantitative molecular orbital correlation diagram for the $[C\text{-}O\text{-}O]^+$ system. A perpendicular approach of C^+ and O_2 (C_{2v} symmetry) is shown on the left side and a collinear approach ($C_{\infty v}$ symmetry) is shown on the right. Crossings which can become avoided in C_s symmetry are indicated by filled circles. Open circles indicate the close interaction between the $O(2p_\sigma)$ and $CO(\sigma)$ orbitals.

Chapter Five

Kinetic Energy Dependence of $C^+(^2P) + N_2$

5.1 INTRODUCTION

The reaction of atomic carbon ion with molecular nitrogen has three primary reaction channels: simple charge transfer, process (5.1a); atom abstraction, process (5.1b); and abstraction-charge transfer, process (5.1c).

$$C^+(^2P_u) + N_2(^1\Sigma_g{}^+) \rightarrow N_2{}^+(^2\Sigma_g{}^+) + C(^3P_g) \qquad \Delta H^\circ_0 = 4.32 \pm 0.01 \text{ eV} \qquad (5.1a)$$

$$\rightarrow CN^+(^1\Sigma^+, ^3\Pi) + N(^4S_u) \qquad \Delta H^\circ_0 = 4.83 \pm 0.13 \text{ eV} \qquad (5.1b)$$

$$\rightarrow N^+(^3P_g) + CN(^2\Sigma^+) \qquad \Delta H^\circ_0 = 5.26 \pm 0.10 \text{ eV} \qquad (5.1c)$$

This system is somewhat unusual in the world of ion - molecule chemistry because all three reaction channels have similar thermodynamic thresholds that are fairly high in energy[1] (although the precise heat of formation of CN is still uncertain, as discussed below). Competition between these channels should be influenced by several factors. For instance, reaction (5.1a) is parity-forbidden while reactions (5.1b) and (5.1c) have no parity restrictions. The dynamics of the processes may differ substantially since processes (5.1b) and (5.1c) require intimate collisions to occur while reaction (5.1a) can proceed via long-range electron transfer. Spin is conserved in reactions (5.1a), (5.1c), and (5.1b) if $CN^+(^3\Pi)$ is formed but not if $CN^+(^1\Sigma^+)$ is the product. As for the isoelectronic C_2 molecule,[2] these states of CN^+ are likely to be nearly degenerate. Presently, it is experimentally unknown which of these states is the ground state of

CN^+,[3] and theory is divided.[4-10] The most extensive calculations suggest that the zero point energy of the $^1\Sigma^+$ state is lower than that of the $^3\Pi$ state by 0.08 $\pm$ 0.03 eV.[8]

In contrast to reactions of C^+ with H_2[11] and O_2,[12] relatively little work has been performed on the reaction of C^+ with N_2. The available literature consists of early ion beam studies of Koski and coworkers,[13] kinetic energy measurements of Leventhal,[14] studies at high energies by Moran and Mathur[15] and Ottinger and Simonis,[16] and phase space calculations of Fullerton and Moran.[17]

In the present chapter, the kinetic energy dependencies of reactions (5.1a) - (5.1c) from threshold to 28 eV are investigated through the use of guided ion beam mass spectrometry. Total reaction cross sections and product branching ratios are compared to previous experimental results[13-16] and to the predictions of phase space theory (PST).[17] Thermochemistry for CN and CN^+ is derived, and reaction mechanisms and electronic state correlations for these processes are discussed.

5.1.1 Thermochemistry

An interesting aspect of this reaction system is the thermochemistry of CN. This is a particularly important problem in astrophysical chemistry as recently reviewed by Costes *et al.*.[18] These authors measure a 0 K bond dissociation energy of $D^\circ_0(CN)$ = 7.77 $\pm$ 0.05 eV by laser-induced fluorescence studies. They list other experimental determinations dating from 1973 that include spectroscopic studies of Engleman and Rouse, 7.66 $\pm$ 0.05 eV,[19] and shock tube studies of Colket, 7.92 $\pm$ 0.07 eV,[20] and of Arnold and Nicholls, 7.89 $\pm$ 0.13 eV.[21] In earlier work, Dibeler and Liston obtain an average value of 7.83 $\pm$ 0.08 eV from photoionization threshold

measurements of four molecules.[22] Davis and Okabe obtain an average value of 7.81 ± 0.10 eV from photodissociation measurements of five molecules.[23] Setser and Steadman obtain a lower limit of 7.78 eV,[24] while Berkowitz *et al.* find 7.68 ± 0.09 eV.[25] The latest *ab initio* calculations find 7.53 eV which is scaled to 7.65 ± 0.06 eV based on equivalent calculations for the N_2 molecule.[26] Thus, reasonable values for D°_0(CN) range from 7.6 to 8.0 eV. The average of all these determinations is 7.78 ± 0.10 eV, identical with the value adopted in the JANAF Tables, 7.78 ± 0.11 eV.[1]

The ionization energy, IE, of the CN molecule is also not rigorously established. IE(CN) has not been measured directly. Indirect measurements include a value of 14.20 ± 0.03 eV from Dibeler and Liston,[22] and a value of 14.03 ± 0.02 eV from Berkowitz *et al.*.[25] The JANAF Tables choose the average of these two values, 14.11 ± 0.09 eV,[1] while Lias *et al.* report 14.09 eV from an unspecified source.[27]

5.2 EXPERIMENTAL

In the present system, the absolute cross section magnitudes were quite sensitive to the cleanliness of the octopole. This lead to spurious observations of anomalously large cross sections for reactions (5.1a) and (5.1b) due to mass discrimination against the low mass C^+ and N^+ species. The absolute magnitudes presented here were reproduced on at least four separate occasions spanning six years

and two octopole configurations.[28,29] The reproducibility of the cross section magnitudes among these data sets is about $\pm 20\%$.

One minor experimental consideration is the purity of the N_2 reactant, particularly with regard to O_2 contamination. It is known (Chapter 4) that reaction of $C^+(^2P)$ with O_2 forms CO^+ very efficiently in an exothermic reaction.[12] Since CO^+ has the same nominal mass as N_2^+, the presence of even small amounts of O_2 can obscure the threshold for the N_2^+ product. The data presented here are free from this problem.

5.3 RESULTS

5.3.1 Cross Sections

Representative experimental results for reactions (5.1a) - (5.1c) are shown in Figure 5-1. The threshold regions of these three products are shown in Figure 5-2. All three channels display apparent thresholds near 5 eV, as expected from the known thermochemistry. The cross section for CN^+ is the dominant product at low energies and reaches a maximum near 10 eV. Twelve independent data sets yield an average maximum cross section of 0.67 ± 0.10 Å^2. At higher energies, $\sigma(CN^+)$ falls off rapidly. This decline in the cross section corresponds to the thermodynamic threshold for dissociation of the CN^+ product to $C^+ + N$, reaction (5.2). These observations

$$C^+(^2P_u) + N_2(^1\Sigma_g^+) \rightarrow C^+(^2P_u) + 2\,N(^4S_u) \qquad \Delta H^\circ_0 = 9.76 \text{ eV} \qquad (5.2)$$

suggest that the CN^+ formed in reaction (5.1b) is primarily in the $^3\Pi$ state since it seems unlikely that the spin-forbidden production of $CN^+(^1\Sigma^+) + N(^4S_u)$ would

compete effectively with the spin-allowed reactions (5.1a) and (5.1c). Furthermore, while $CN^+(^3\Pi)$ can dissociate to the ground state $C^+(^2P_u)$ + $N(^4S_u)$ atoms of reaction (5.2), $CN^+(^1\Sigma^+)$ dissociates to an excited state asymptote, $C^+(^2P_u)$ + $N(^2D_u)$,[7] 2.38 eV higher in energy such that ΔH°_0 = 12.14 eV. Thus, the sharp decline in the CN^+ cross section observed at the threshold for reaction (5.2) is evidence for the presence of $CN^+(^3\Pi)$ since efficient dissociation of $CN^+(^1\Sigma^+)$ at this limit is not expected. While not obvious in Figure 5-1, $\sigma(CN^+)$ does begin to decline more rapidly at about 12 eV. This behavior could be due to the presence of $CN^+(^1\Sigma^+)$ or to a secondary dissociation channel for $CN^+(^3\Pi)$.

As expected from the thermochemistry, the cross section for N^+ has a somewhat later onset than reaction (5.1b). $\sigma(N^+)$ reaches a maximum value of 0.21 $\pm$ 0.05 $Å^2$ (average of 12 data sets) over the range of 8 - 10 eV. This product cross section also declines above 10 eV, a result that cannot be due to dissociation. The decline may be caused by competition with the direct, collision-induced dissociation process, reaction (5.2). The decrease in $\sigma(N^+)$ slows as the energy is increased further until the cross section begins to increase slowly at energies above ~ 20 eV. This increase in N^+ production must be due to dissociation of the N_2^+ (and possibly the CN^+) reaction products. The overall reaction corresponds to process (5.3), and has a ΔH°_0 value of 13.03 $\pm$ 0.01 eV:

$$C^+(^2P_u) + N_2(^1\Sigma_g^+) \rightarrow N^+(^3P_g) + N(^4S_u) + C(^3P_g). \qquad (5.3)$$

The N_2^+ charge transfer product has the lowest thermodynamic threshold of the three reactions (5.1a) - (5.1c); however, $\sigma(N_2^+)$ rises more slowly than $\sigma(CN^+)$

and has an apparent threshold that is nearly the same. The cross section for N_2^+ is dominant above ~ 7 eV and attains a maximum value of 0.85 ± 0.15 Å^2 (average of 12 data sets) near 13 eV before declining gradually at higher energies. This energy corresponds to dissociation of the N_2^+ product, process (5.3), although the increase in $\sigma(N^+)$ does not fully account for the observed decrease in $\sigma(N_2^+)$. It is possible that the cross sections for reactions (5.1a) and (5.3) may be small at these higher energies because of inefficient collection of the products. As discussed previously,[30] charge transfer products may be particularly susceptible to losses because they can be formed via long-range electron transfer resulting in little forward velocity in the laboratory frame.

5.3.2 Comparison with Other Studies

The only previous low energy cross section measurements for reactions (5.1a) - (5.1c) are those of Koski and coworkers.[13] They attempted to measure the reaction cross sections for both $C^+(^2P)$ and $C^+(^4P)$ between 3.5 and 140 eV (5 to 200 eV lab). For formation of CN^+ and N^+ from $C^+(^2P)$, their cross sections lie below the present measurements by a factor of ~ 10, and have markedly different energy dependencies than the present data. For N_2^+ formation, their cross section increases smoothly from a value of 0.01 Å^2 at 3.5 eV to a value of 0.20 Å^2 at 140 eV. This is lower than the present results by a factor of ~ 20 in the threshold region and a factor of ~ 5 at 28 eV.

The severe differences in both energy dependence and absolute magnitude between the present data and those of Koski *et al.*[13] are attributable to deficiencies in

the collection efficiency (especially at low kinetic energies) in the latter experiments. Those experiments utilized an experimental geometry that extracts product ions at right angles to the incident ion beam. This configuration discriminates against product ions formed with any forward velocity in the laboratory frame. In order to reduce this discrimination, strong repeller voltages were used to help extract the product ions from the interaction region. This introduces a substantial, but unknown, spread in the energy of the primary ion beam. In the present work, the use of the octopole ion guide helps ensure efficient collection of all primary and secondary ions at all kinetic energies, without the use of repeller fields.

In addition to the work of Koski *et al.*,[13] a limited number of other experimental studies have been published. The kinetic energy measurements of Leventhal[14] suggest that CN^+ formation occurs via a direct, stripping-type mechanism and that the CN^+ product is internally excited by large amounts even at energies near the threshold. It is unknown whether these results are representative of the bulk of the CN^+ product ions since only those ions scattered very close to 0° are collected in this experiment. Comparisons of the present results to those of Moran and Mathur[15] and Ottinger and Simonis[16] are not possible since these studies examined reaction (5.1) at much higher kinetic energies (700 to 2,500 eV lab and 1,000 eV lab, respectively).

5.4 DISCUSSION

As noted in the introduction, one of the more interesting features of reaction (5.1) is the competition between the three possible reaction channels. To understand

this competition, the cross sections are first fit to empirical models to extract thermochemical and dynamical information. Next, the electronic state correlation diagram associated with reaction (5.1) is examined. Finally, statistical theories are evaluated to see if they can reproduce the observed results.

5.4.1 Reaction Thresholds

Careful examination of the threshold region for processes (5.1a) - (5.1c), Figure 5-2, reveals that formation of the CN^+ and N^+ products occurs at energies slightly below the known thermodynamic thresholds. This effect is due to energy broadening arising from the distribution of ion kinetic energies in the ion beam and the random thermal motion of the N_2 reactant gas. In order to determine the true cross section behavior in the threshold region, an empirical model for the true cross section is convoluted over the experimental distributions of ion and neutral energies.[28] The convoluted form of the trial cross section is then compared directly to the experimentally observed cross section. Finally, the parameters of the trial function are adjusted by using non-linear least squares procedures to obtain the best possible fit to the actual data.

For the case of reactions (5.1a) - (5.1c), the model used to fit the data is

$$\sigma(E) = \sigma_0(E - E_T)^n/E, \tag{5.4}$$

where $\sigma(E)$ is the true cross section, E is the relative kinetic energy of the reactants, σ_0 is a scaling factor, and E_T is the threshold energy. E_T, σ_0, and n are treated as adjustable parameters. In order to compare the experimentally determined threshold energies to the literature values given in equation (5.1) the thresholds must be

corrected to 0 K. While the analysis procedure explicitly accounts for all kinetic energy effects, it does not include the internal energy of the reactants. The N_2 reactant possesses k_BT (= 0.026 eV at 305 K) of rotational energy but no vibrational energy, while the $C^+(^2P)$ reactant contains 5 meV of energy if the spin-orbit states of the $C^+(^2P)$ reactant are assumed to be statistically populated. Thus, the 0 K threshold, $E_{T,0K}$, equals E_T + 0.03 eV.

Formation of N^+ and CN^+. The model in equation (5.4) is used to analyze between 8 and 14 independent data sets. For reaction (1b), the optimum parameters are found to be $\sigma_0 = 0.96 \pm 0.20$, $n = 1.38 \pm 0.15$, and $E_{T,0K} = 4.72 \pm 0.12$ eV. For the directly competitive reaction (5.1c), the optimum value of n is similar, 1.26 $\pm$ 0.10, while the scaling factor is about one-half that for reaction (5.1b), $\sigma_0 = 0.55$ $\pm$ 0.11. The optimum threshold is $E_{T,0K} = 5.21 \pm 0.14$ eV. Figure 5-3 shows that, when convoluted over the known experimental kinetic energy distributions, these models accurately reproduce the data for reactions (5.1b) and (5.1c).

The 0 K threshold values derived are in reasonable agreement with the thermodynamic values calculated from the literature,[1] 4.83 $\pm$ 0.13 eV and 5.26 $\pm$ 0.10 eV, respectively. Alternatively, the measured threshold for reaction (5.1c) can be combined with the heats of formation[1] for C^+, N_2, and N to determine $\Delta_f H^\circ_0(CN)$ = 102 $\pm$ 3 kcal mol^{-1} and $D^\circ_0(CN)$ = 7.82 $\pm$ 0.14 eV. These values are in excellent agreement with most previous results[18-26] and with the value chosen by the JANAF Tables.[1] Unfortunately, the precision of the present measurement is insufficient to resolve the discrepancies between the previous determinations.

A different way of viewing these results is to note that the difference between the thresholds for reactions (5.1b) and (5.1c) is just the difference between the ionization energies (IE) of N and CN. The difference between the average thresholds for reactions (5.1b) and (5.1c) is 0.49 $\pm$ 0.18 eV. A slightly more precise value is obtained by comparing the relative thresholds for individual data sets. The average of these differences is taken to be the best determination of the relative thresholds and the difference between IE(N) and IE(CN), 0.51 $\pm$ 0.14 eV. Since IE(N) = 14.534 eV is known very precisely,[1] this difference yields IE(CN) = 14.02 $\pm$ 0.14 eV, in much better agreement with the value derived by Berkowitz *et al.*, 14.03 $\pm$ 0.02 eV,[25] than with that by Dibeler and Liston, 14.20 $\pm$ 0.03 eV.[22] The agreement between the present value and the literature values suggests that the $^3\Pi$ state of CN^+ formed in reaction (5.1b) is either the ground electronic state or is within experimental error of a $^1\Sigma^+$ ground state. This latter conclusion is in agreement with the quantitative ordering of these states calculated by Bruna *et al.*.[8]

Formation of N_2^+. Analysis of the data for reaction (5.1a), formation of N_2^+, is not so straightforward. Simple application of equation (5.4) did not permit the data to be reproduced well over the entire threshold region. In essence, the cross section rises slowly at first, and then more rapidly. This behavior cannot be accommodated by equation (5.4) Careful examination of the data near threshold indicates that the cross section for formation of N_2^+ becomes nonzero beginning near 4.3 eV. Indeed, as shown in Figure 5-4, this threshold region can be reproduced nicely by using σ_0 = 0.22, n = 1.3 (a value near those used for the other reaction channels), and $E_{T,0K}$ =

4.32 eV, the thermodynamic threshold for $N_2^+(^2\Sigma_g^+)$. The data deviate from this model beginning near 5.3 eV. This energy is near the threshold for formation of the $N_2^+(^2\Pi_u)$ first excited state at 5.43 eV.[1] This suggests that the odd behavior of the N_2^+ cross section is due to inefficient formation of the $N_2^+(^2\Sigma_g^+)$ ground state, and relatively efficient production of $N_2^+(^2\Pi_u)$. Given this assumption, the data can be reproduced very precisely with $n = 1.3$ and $\sigma_0(^2\Pi_u) = 1.19$, a factor of five larger than the scaling constant for formation of the $^2\Sigma_g^+$ state. This is also shown in Figure 5-4.

The inefficiency of the $N_2^+(^2\Sigma_g^+) + C(^3P_g)$ product channel may be a reflection that this reaction is parity-forbidden, as noted in the introduction. Since formation of $N_2^+(^2\Pi_u) + C(^3P_g)$ is parity-allowed, this reaction should occur much more readily. An alternate rationale for the observed behavior is that electron transfer from the $3\sigma_g$ orbital of N_2, which forms the $N_2^+(^2\Sigma_g^+)$ state, would occur most efficiently for collinear collisions between C^+ and N_2. This may be relatively improbable compared to off-collinear collisions that result in more extensive interaction of C^+ with the $1\pi_u$ orbitals of N_2, and lead to generation of the $^2\Pi_u$ state of N_2^+.

5.4.2 Electronic State Correlation Diagram

To understand the results for reaction (5.1), the potential energy surfaces involved should be characterized. Unfortunately, this is a reasonably complex system involving many surfaces and surface crossings, and no theoretical calculations are available for the surfaces of CN_2^+. However, the key features in this reaction system

can be obtained qualitatively by using simple correlation rules.[31] This leads to the electronic state correlation diagram for reaction (5.1) in $C_{\infty v}$ symmetry shown in Figure 5-5. This diagram only includes doublet surfaces since it seems unlikely that spin-forbidden reactions are involved in any of the reactions, as discussed above. The various states and energies of the CN_2^+ intermediate are assumed to be similar to those of the isoelectronic CCN species (except for the upper $^2\Pi$ state which is unknown).[32] A more detailed analysis utilizing semiquantitative molecular orbital considerations and explicitly considering reactions in C_{2v} symmetry was also carried out and yielded comparable correlations.[33]

As $C^+(^2P_u)$ approaches the $N_2(^1\Sigma_g^+)$ molecule, three doublet surfaces evolve. For collisions having $C_{\infty v}$ (C_{2v}, C_s) symmetry, these three surfaces are $^2\Sigma^+$ (A_1, A'), $^2\Pi$ (B_1, A"), and $^2\Pi$ (B_2, A'). The $^2\Pi$ (B_2, A') surface corresponds to the occupied 2p orbital of C^+ oriented perpendicular to the line of the collision but in the plane defined by the three atoms, and the $^2\Pi$ (B_1, A") surface corresponds to the occupied 2p orbital perpendicular to this plane. The $^2\Pi$ surfaces correlate directly with the $^2\Pi$ ground state of the CN_2^+ intermediate. Since the interaction of C^+ and N_2 should be slightly attractive, an energy slightly below that of the ground state reactants is assigned to this state. The $CN_2^+(^2\Pi)$ intermediate leads directly to the $CN^+(^3\Pi)$ + $N(^4S_u)$ products, accounting for the relatively efficient formation of this product channel. No correlations from reactants to the $CN^+(^1\Sigma^+)$ + $N(^4S_u)$ product channel, which evolves along a $^4\Sigma^-$(A") surface, are possible without *both* a reduction in symmetry from $C_{\infty v}$ to C_s and a change in spin.

Based on the correlations shown in Figure 5-5, the $^2\Sigma^+$ (A_1, A') surface evolving from the reactants should account for the remainder of the reactivity observed in this system. This surface corresponds to approaches of the reactants with the occupied 2p orbital of C^+ oriented along the line of the collision, an interaction that should be quite repulsive. Indeed, this surface correlates to the third excited state of CN_2^+, and then on to an excited state asymptote for reaction (5.1c), $N^+(^3P_g)$ + $CN(^2\Pi)$. Note that this $^2\Sigma^+$ (A') surface cannot interact with the $^2\Sigma^-$ (A") surface evolving from the ground-state products of reaction (5.1a), $N_2^+(^2\Sigma_g^+)$ + $C(^3P_g)$, even in C_s symmetry. This is a direct consequence of the parity forbidden character of this reaction. However, there will be an avoided crossing in C_{2v} and C_s symmetry between the $^2\Sigma^+$ (A_1, A') surface and the $^2\Delta$ (A_1, A') surface evolving from the excited state asymptote, $N_2^+(^2\Pi_u)$ + $C(^3P_g)$. This may provide a reasonably efficient pathway for formation of this product channel. A possible pathway for forming the ground state $N_2^+(^2\Sigma_g^+)$ + $C(^3P_g)$ products also involves this same avoided crossing, $^2\Sigma^+$ to $^2\Delta$, but the $CN_2^+(^2\Delta)$ intermediate must then pass through the collinear geometry where the Δ (A_1, A') and Δ (A_2, A") surfaces become degenerate. The intermediate would then cross to the $^2\Sigma^-$ (A_2, A") surface evolving from the desired products in either C_{2v} or C_s symmetry. Such a pathway could account for the inefficient formation of this product channel at the thermodynamic threshold.

Formation of the $N^+(^3P_g)$ + $CN(^2\Sigma^+)$ products can conceivably proceed in two ways. The reactants begin along the $^2\Sigma^+$ surface and cross to the $^2\Delta$ (A_1, A') state of CN_2^+ in C_{2v} or C_s symmetry. This species must then pass through the collinear

geometry where the Δ (A_1, A') and Δ (A_2, A") surfaces become degenerate, before crossing to the $^2\Sigma^-$ (A_2, A") surface evolving from $N^+(^3P_g)$ + $CN(^2\Sigma^+)$ in C_{2v} or C_s symmetry. A more likely pathway passes through the $CN_2^+(^2\Sigma^+)$ state and then undergoes an avoided crossing in C_s symmetry with a $^2\Pi$ (A') surface evolving from the desired products. This pathway should be a fairly efficient means of forming these products if the energy of the presumed $CN_2^+(^2\Pi)$ excited state (which must exist) lies below that of the product asymptote.

The qualitative considerations discussed above suggest that reaction (5.1b) can occur efficiently along 4 of the 6 surfaces evolving from the reactants, while the other 2 surfaces can lead to reactions (5.1a) and (5.1c). This offers an appealingly simple explanation for the 2:1 ratio observed for the cross sections of the directly competitive reactions (5.1b) vs. (5.1c). Additional insight into this system would undoubtedly be derived from a theoretical examination of the potential energy surfaces involved with this reaction.

5.4.3 Phase Space Calculations

In order to determine if the energy dependencies of reactions (5.1a) - (5.1c) can be explained by statistical effects, atom-diatom phase space theory (PST) calculations were carried out using modified versions of computer programs originally developed by Chesnavich and Bowers.[34] These calculations contain no explicitly adjustable parameters, although it is possible to exert indirect control over the absolute and relative magnitudes of the calculated cross sections by changing the number of potential energy surfaces associated with each reaction channel. For the

present calculations, the number of surfaces was based on the analysis of the electronic state correlations performed above. Thus, all 6 surfaces evolving from the $C^+(^2P_u) + N_2(^1\Sigma_g{}^+)$ reactants were assumed to lead to products. Four of these (the $^2\Pi$ surfaces) lead exclusively to reaction (5.1b), $CN^+(^3\Pi) + N(^4S_u)$, and the other two (the $^2\Sigma^+$ surface) can lead to $N_2{}^+(^2\Sigma_g{}^+) + C(^3P_g)$, $N_2{}^+(^2\Pi_u) + C(^3P_g)$, and $N^+(^3P_g) + CN(^2\Sigma^+)$. The results of these calculations are shown in Figure 5-6 along with the experimental data. The PST calculations are not extended to energies for which product dissociation is possible, since phase space theory does not address the possibility of product dissociation.

Figure 5-6 shows that the total cross section calculated by PST is in good agreement with the experimentally determined cross sections up to ~ 7 eV. This suggests that reaction (5.1) may behave more statistically near threshold than might otherwise have been expected for reactions that are very endothermic. However, the calculations fail to predict the energy dependence of the individual product channels very well, although the absolute magnitudes of the PST results are in qualitative accord with the data. For both N^+ and CN^+, the data show an earlier apparent onset and rise more rapidly than the phase space predictions. For $N_2{}^+$, the PST cross section displays an earlier onset than the data, rises more rapidly at first and less rapidly at higher energies.

The comparisons between the PST results and the present data are consistent with several observations made above. Since PST puts no restrictions on the parity forbidden reaction (5.1a), the calculated cross section for $N_2{}^+$ formation is too large

near threshold. This in turn may suppress the calculated probability of forming CN^+ and N^+ near their respective thresholds, causing their PST cross sections to rise too slowly. The failure of PST to reproduce the rapid rise in the N_2^+ cross section at higher energies suggests that PST underestimates the production of $N_2^+(^2\Pi_u)$. Further, if this reaction channel were to compete with formation of CN^+, this could suppress the calculated probability for forming CN^+ at higher energies, thus bringing the calculated results into better agreement with the data.

Phase space calculations have also been carried out for this system by Fullerton and Moran.[17] Unfortunately, direct comparison of the present PST results to these earlier calculations is difficult. For the N_2^+ channel, they show no results for formation of the X or A states below 28 eV. For the N^+, they consider only dissociative charge transfer to form $N^+ + N + C$ and hence no results are shown below 13 eV. For CN^+, their results are similar in shape and about half the size of the calculated cross section for this channel in Figure 5-6. Thus, their calculated cross sections for this process agree with the magnitude of the present data in the threshold region but again rise more slowly than the data. At energies above the onset for reaction (5.2), their calculations are considerably larger than the experimental data although the shape of the cross section is qualitatively reproduced.

5.5 CONCLUSION

Guided ion beam mass spectrometry has been used to examine the kinetic energy dependence of the reaction of ground-state atomic carbon ion with molecular

nitrogen from threshold energies to 28 eV. Cross section behavior in the threshold region is found to be consistent with literature thermochemistry for formation of CN^+ + N, N^+ + CN, and N_2^+ + C. Specifically, the thresholds measured here lead to the thermochemistry: $\Delta_f H^\circ_0(CN) = 102 \pm 3$ kcal mol^{-1}, $D^\circ_0(CN) = 7.82 \pm 0.14$ eV, and IE(CN) = 14.02 ± 0.14 eV. Formation of CN^+ is observed to be relatively efficient, suggesting that the $^3\Pi$ state of CN^+ (which can be formed in a spin-allowed process) is either the ground state or within 0.14 eV of a $^1\Sigma^+$ ground state (a species that cannot be formed in a spin-allowed process from ground state reactants). The cross section for N_2^+ formation has a complicated energy dependence which suggests that N_2^+ is formed preferentially in its $A^2\Pi$ first excited state rather than the $X^2\Sigma_g^+$ ground state. Electronic state correlations for reaction (5.1) suggest that $CN^+(^3\Pi)$ is formed along 4 of the 6 surfaces evolving from the reactants, while the other 2 surfaces can lead to generation of N^+ and N_2^+. Phase space calculations are in good agreement with the total experimental reaction cross section, but not with the cross sections for individual product channels.

5.6 REFERENCES

1. Reaction enthalpies correspond to formation of products in their ground electronic states at 0 K and are based on tabulated heats of formation from the JANAF Tables: M. W. Chase, Jr., C. A. Davies, J. R. Downey, Jr., D. J. Frurip, R. A. McDonald, and A. N. Syverud, J. Phys. Chem. Ref. Data **14**, Supp. 1 (1985). The listing for $\Delta_f H°$(CN, 0 K) on page 163 of this reference is confusing since a value of 436.8 $\pm$ 10 kJ mol^{-1} is listed at the top of the page but the text cites adoption of a median value of 103.2 $\pm$ 2.5 kcal mol^{-1} (431.8 $\pm$ 10 kJ mol^{-1}). This latter value is consistent with the discussion on page 614 and hence is used here.
2. E. A. Ballik and D. A. Ramsay, Astrophys. J. **137**, 61, 84 (1963).
3. K. P. Huber and G. Herzberg, Constants of Diatomic Molecules, (Van Nostrand Reinhold, New York, 1979). These authors list no information regarding the $CN^+(^3\Pi)$ state.
4. A. A. Wu, Chem. Phys. **21**, 173 (1977); Chem. Phys. Lett. **59**, 457 (1978).
5. D. M. Hirst, Chem. Phys. Lett. **65**, 181 (1979).
6. T. K. Ha, Chem. Phys. Lett. **66**, 317 (1979).
7. J. N. Murrell, A. Al-Derzi, J. Tennyson, and M. F. Guest, Molec. Phys. **38**, 1755 (1979).
8. P. J. Bruna, S. D. Peyerimhoff, and R. J. Buenker, J. Chem. Phys. **72**, 5437 (1980); Chem. Phys. Lett. **72**, 278 (1980).

9. B. O. Roos, P. Linse, P. E. M. Siegbahn, and M. R. A. Blomberg, Chem. Phys. **66**, 197 (1982).

10. S. Evangelisti, J. P. Daudey, and J. P. Malrieu, Chem. Phys. **75**, 91 (1983).

11. K. M. Ervin and P. B. Armentrout, J. Chem. Phys. **84**, 6738 (1986).

12. J. D. Burley and P. B. Armentrout, Int. J. Mass Spectrom. Ion Proc. **84**, 157 (1988).

13. W. S. Koski, Rec. Chem. Prog. **31**, 155 (1970); R. C. C. Lao, R. W. Rozett, and W. S. Koski, J. Chem. Phys. **49**, 4202 (1968).

14. J. J. Leventhal, J. Chem. Phys. **55**, 4654 (1971).

15. T. F. Moran and B. P. Mathur, Phys. Rev. A **21**, 1051 (1980).

16. C. Ottinger and J. Simonis, Chem. Phys. **28**, 97 (1978).

17. D. C. Fullerton and T. F. Moran, Int. J. Mass Spectrom. Ion Phys. **9**, 15 (1972).

18. M. Costes, C. Naulin, and G. Dorthe, Astron. Astrophys. **232**, 270 (1990).

19. R. Engleman and P. E. Rouse, J. Quant. Spectrosc. Radiat. Transfer **15**, 831 (1975).

20. M. B. Colket, J. Quant. Spectrosc. Radiat. Transfer **31**, 7 (1984).

21. J. O. Arnold and R. W. Nicholls, J. Quant. Spectrosc. Radiat. Transfer **12**, 1435 (1972).

22. V. H. Dibeler and S. K. Liston, J. Chem. Phys. **47**, 4548 (1967); **48**, 4765 (1968).

23. D. D. Davis and H. Okabe, J. Chem. Phys. **49**, 5526 (1968).

24. D. W. Setser and D. H. Steadman, J. Chem. Phys. **49**, 467 (1968).

25. J. Berkowitz, W. A. Chupka, and T. A. Walter, J. Chem. Phys. **50**, 1497 (1969).

26. C. W. Bauschlichter, R. S. Langhoff, and P. R. Taylor, Astrophys. J. **332**, 531 (1988).

27. S. G. Lias, J. E. Bartmess, J. F. Liebman, J. L. Holmes, R. D. Levin, and W. G. Mallard, J. Phys. Chem. Ref. Data **17**, Supp. 1 (1988).

28. K. M. Ervin and P. B. Armentrout, J. Chem. Phys. **83**, 166 (1985).

29. L. S. Sunderlin and P. B. Armentrout, Chem. Phys. Lett. **167**, 188 (1990).

30. M. E. Weber and P. B. Armentrout, J. Chem. Phys. **90**, 2213 (1989). E. R. Fisher, M. E. Weber, and P. B. Armentrout, J. Chem. Phys. **92**, 2296 (1990).

31. K. E. Shuler, J. Chem. Phys. **21**, 624 (1953).

32. G. Herzberg, Molecular Spectra and Molecular Structure: III. Electronic Spectra and Electronic Structure of Polyatomic Molecules, (Van Nostrand Reinhold, New York, 1966), p. 591.

33. See reference 12 (and Chapter 4 of the present dissertation) for an analogous treatment of the $C^+ + O_2$ system.

34. W. J. Chesnavich and M. T. Bowers, J. Chem. Phys. **68**, 901 (1978).

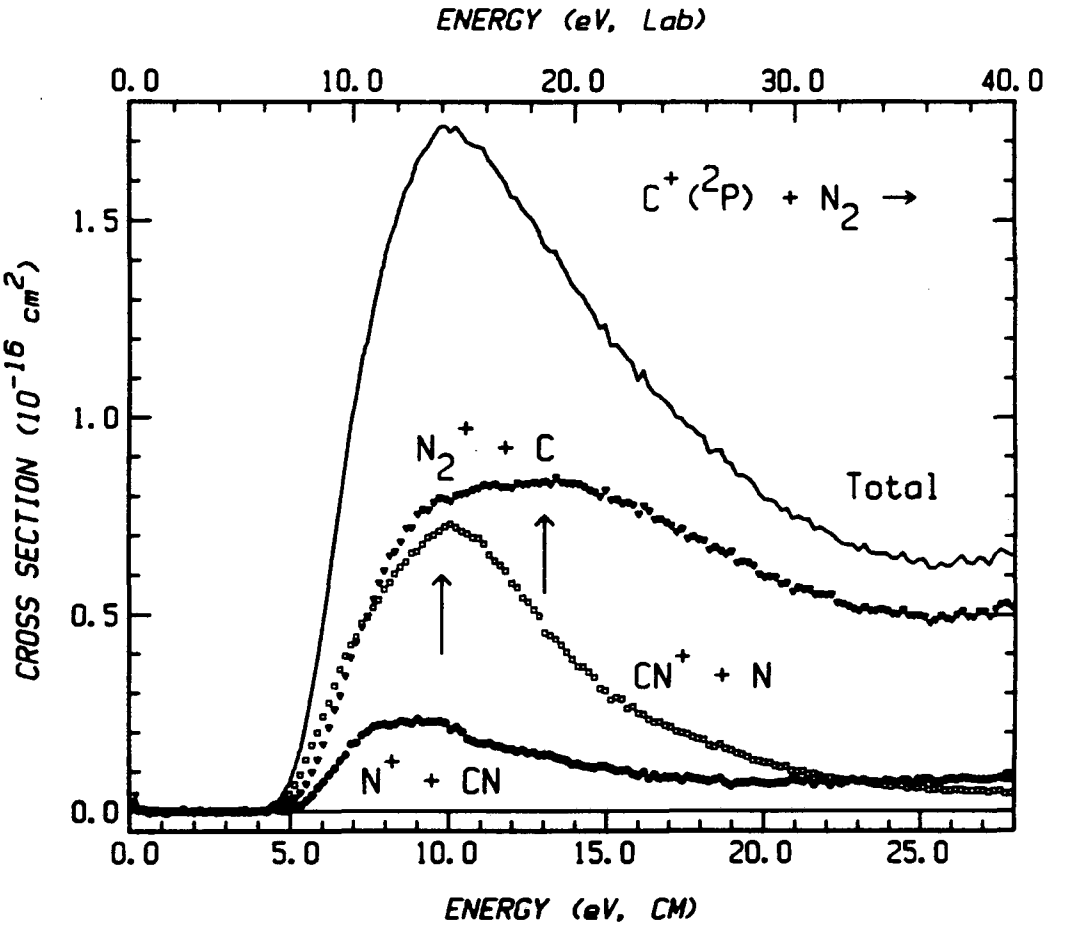

Figure 5-1. Cross sections for reactions (5.1a) - (5.1c) and their total as a function of relative translational energy (lower scale) and laboratory energy (upper scale). Representative results are shown for the cross sections of reaction (5.1a), filled triangles; reaction (5.1b), open squares; reaction (5.1c), filled circles; and the total reaction cross section, solid line. Arrows indicate the thresholds for reaction (5.2) at 9.76 eV and reaction (5.3) at 13.03 eV.

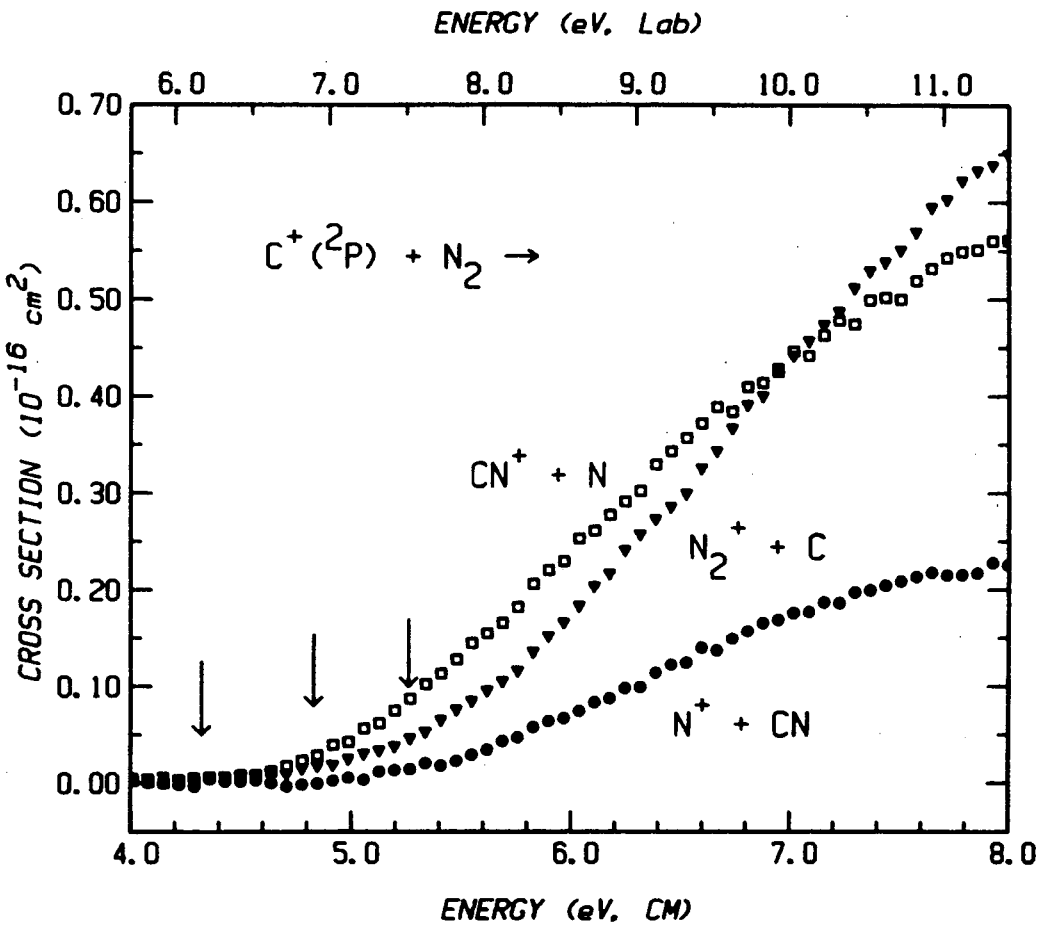

Figure 5-2. Cross sections for reactions (5.1a) - (5.1c) in the threshold region as a function of relative translational energy (lower scale) and laboratory energy (upper scale). Representative results are shown by the same symbols used in Figure 5-1. Arrows indicate the expected thermodynamic thresholds for reactions (5.1a) - (5.1c) at 4.32, 4.83, and 5.26 eV, respectively.

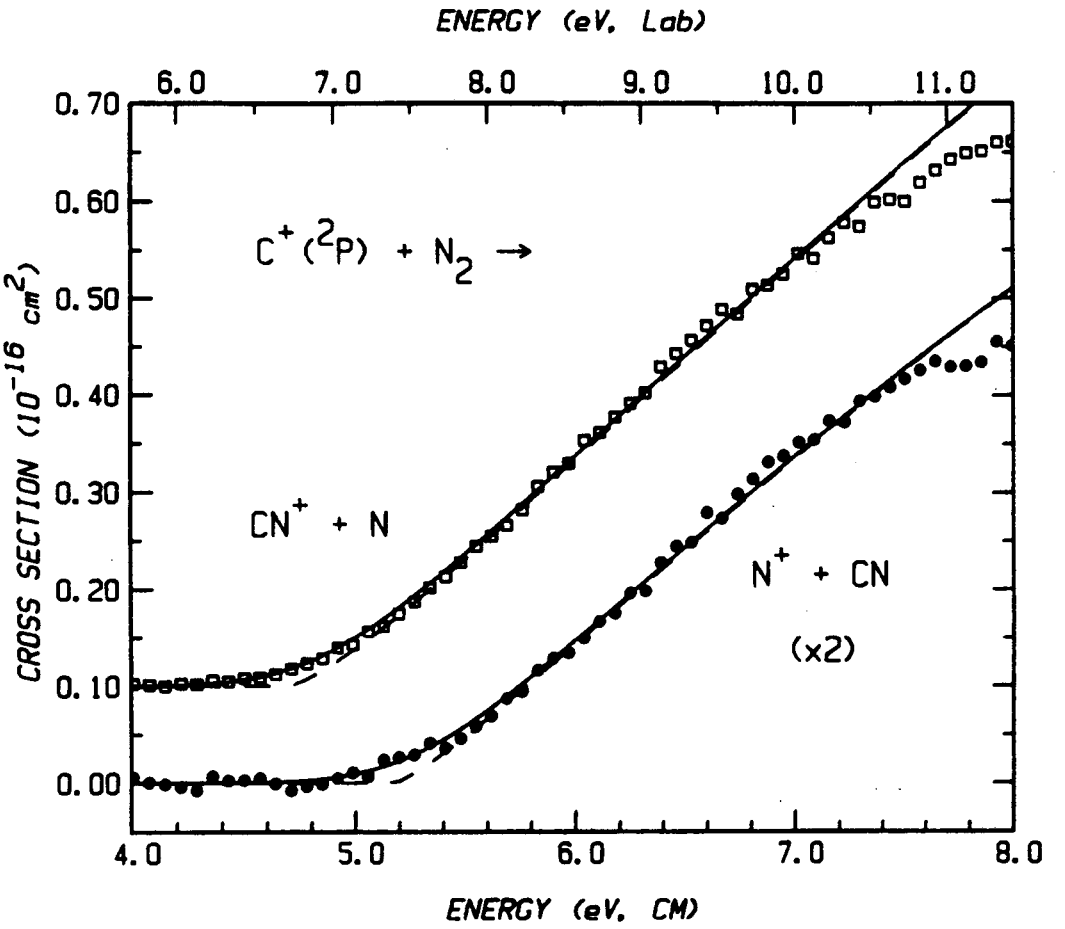

Figure 5-3. Comparison of the cross sections for reactions (5.1b) and (5.1c) with the empirical models discussed in the text as a function of relative translational energy (lower scale) and laboratory energy (upper scale). The zero of the cross section for reaction (5.1b) is shifted to 0.1 Å^2 and the cross section for reaction (5.1c) is multiplied by a factor of two. The unconvoluted and convoluted forms of the empirical models are designated by the dashed and solid lines, respectively.

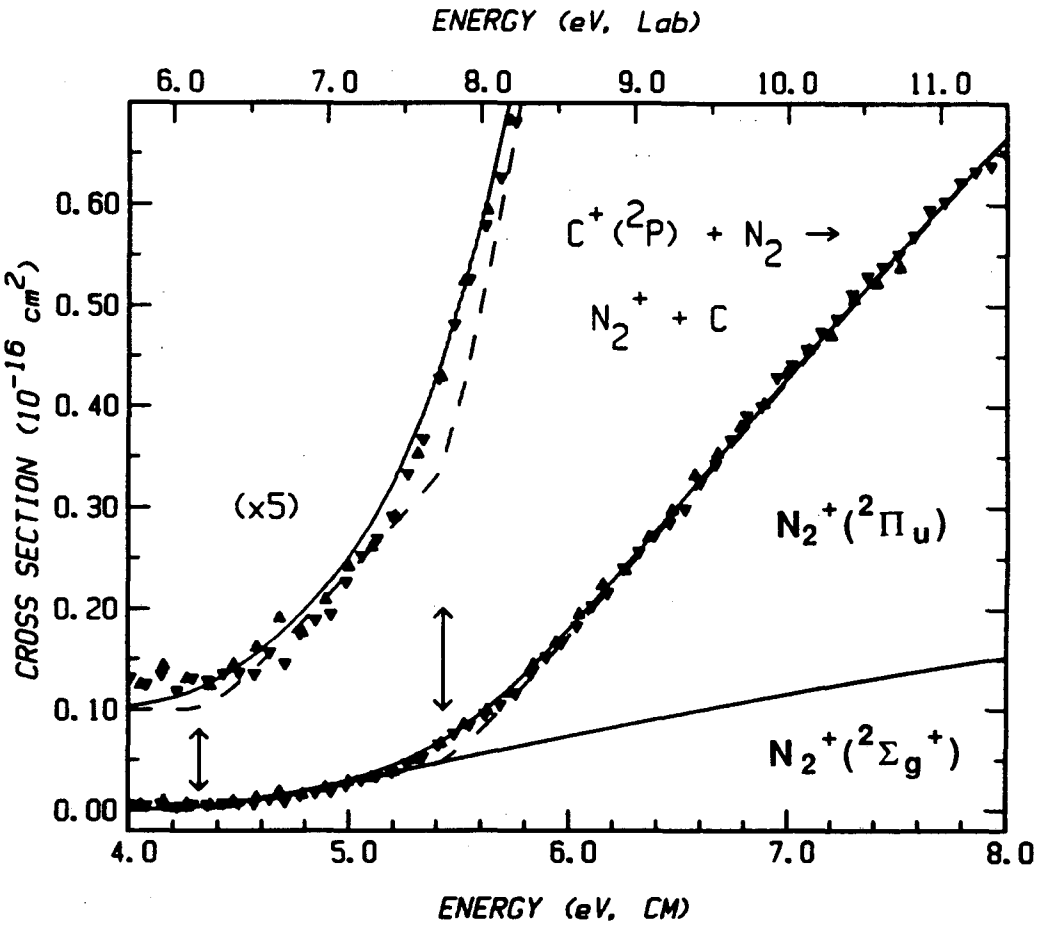

Figure 5-4. Comparison of the cross section for reaction (5.1a) with the empirical models discussed in the text as a function of relative translational energy (lower scale) and laboratory energy (upper scale). Results of two independent data sets are shown by the inverted and upright triangles. The inset shows the data and models increased by a factor of five. Arrows indicate the thermodynamic thresholds for production of N_2^+ in the $^2\Sigma_g^+$ state at 4.32 eV and the $^2\Pi_u$ state at 5.43 eV. The unconvoluted and convoluted forms of empirical models for contributions from both N_2^+ states are designated by the dashed and solid lines, respectively.

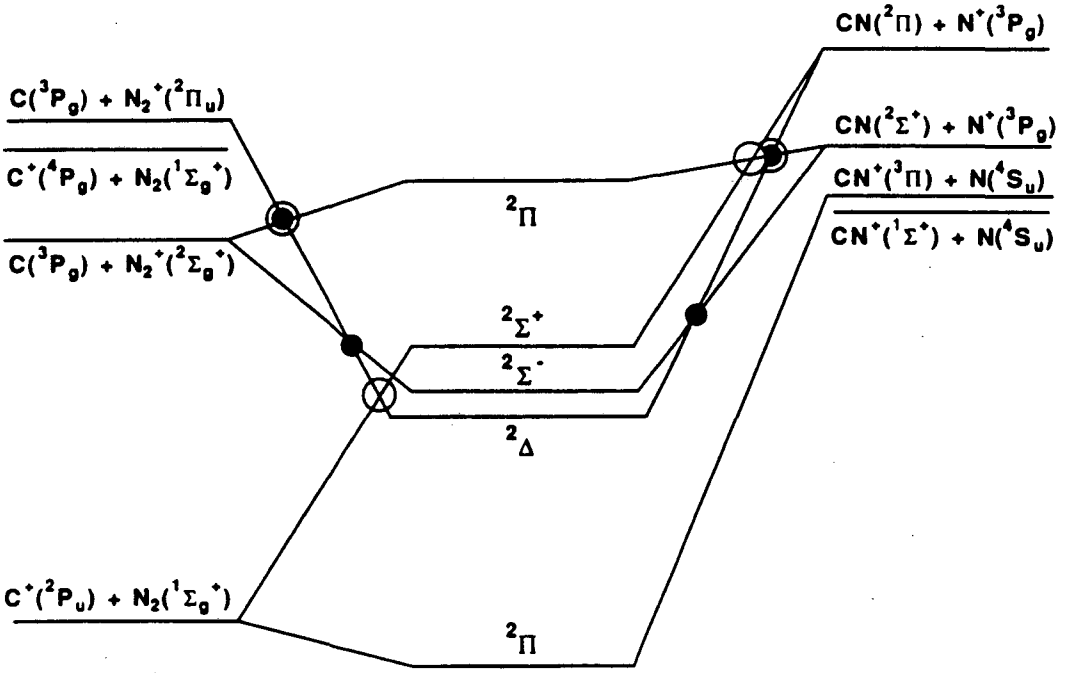

Figure 5-5. Electronic state correlation diagram for reaction (5.1) in $C_{\infty v}$ symmetry along doublet surfaces only. Surface crossings that can become avoided in C_s symmetry are indicated by circles: open circles for surfaces of A' symmetry and filled circles for A" symmetry.

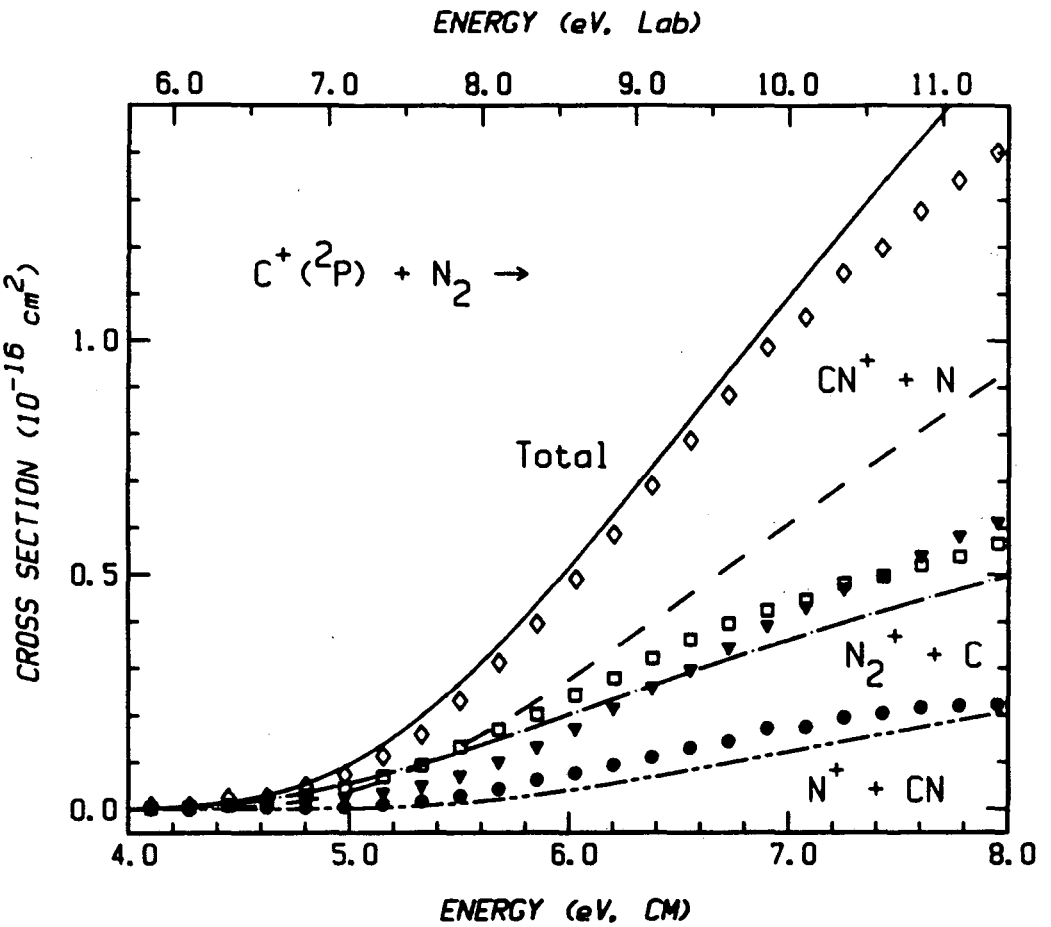

Figure 5-6. Phase space theory (PST) cross sections for reactions (5.1a) - (5.1c) and their total as a function of relative translational energy (lower scale) and laboratory energy (upper scale). The data are the same and use the same symbols as in Figure 5-1 except that the total is indicated by open diamonds. PST results for reaction (5.1a) are shown by the dash-dot line, those for reaction (5.1b) by the dashed line, those for reaction (5.1c) by the double-dash line, and those for the total cross section by the solid full line.

Chapter Six

Photoabsorption Cross Sections of $(FSO_3)_2$ and FSO_3

6.1 INTRODUCTION

Peroxydisulfuryl difluoride was first synthesized by Dudley and Cady.[1] It is a clear liquid that exists in equilibrium with the yellow-brown fluorosulfate radical according to:[2-4]

$$(FSO_3)_2 \rightleftarrows 2FSO_3. \tag{6.1}$$

Although this equilibrium is in many ways analogous to the well-studied[5] $N_2O_4 \rightleftarrows 2NO_2$ system, the O - O bond in $(FSO_3)_2$ (22.4 kcal/mol)[2] is significantly stronger than the N - N bond in N_2O_4 (13.7 kcal/mol).[5] At room temperature the equilibrium strongly favors the dimer,[2] so that a 100 Torr, 298 K sample consists of 0.025 Torr FSO_3 and 99.975 Torr $(FSO_3)_2$. (For comparison, a sample of N_2O_4 under the same conditions consists of 63.6 Torr NO_2 and 36.4 Torr N_2O_4.) To date, both the spectroscopy[6-14] and photoabsorption[15] of the radical have been investigated, and a number of temperature-dependent absorption measurements on dimer-radical mixtures have been performed.[2-4,6] Despite these efforts, the literature apparently contains very little *quantitative* photoabsorption information on the dimer; numerical cross section values have been reported only for 193 (σ = 4.14 x 10^{-18} cm^2) and 450 (σ = 7.64 $\pm$ 0.08 x 10^{-22} cm^2) nm.[4]

In the present chapter, photoabsorption cross sections are measured for $(FSO_3)_2$ from 180 to 450 nm and for FSO_3 from 340 to 450 nm. These measurements are

intended to (1) provide a comprehensive set of cross section data for the dimer, (2) confirm the radical cross sections previously measured by Croce,[15] and (3) lay the groundwork for future photochemical studies involving $(FSO_3)_2$ and FSO_3.

6.2 EXPERIMENTAL

6.2.1 Cary Spectrometer

All absorption measurements were made on a Cary 118-C spectrometer. According to the manufacturer's specifications, the absolute uncertainty in λ for this particular model is determined by the accuracy of the wavelength counter. For 180 to 300 nm, the counter accuracy is specified to be ± 0.3 nm; for 300 to 450 nm, it is specified to be ± 0.5 nm. Calibration checks with NO_2, CS_2 and SO_2 indicate that the actual uncertainty in λ for the instrument is within these limits. The cross section magnitudes measured for these calibration gases are in good agreement (typically $\pm 5\%$ or better) with literature values. Data acquisition on the Cary is controlled by an AT-type personal computer through direct interfaces to the monochromator stepping motor controller and signal output line.

For all FSO_3 and $(FSO_3)_2$ measurements reported here the slit width of the Cary is fixed at 0.10 mm, so that the spectral bandwidth increases with increasing wavelength. At wavelengths of 200, 250, 300, 350, 400 and 450 nm, the full spectral bandwidths are 0.08, 0.17, 0.32, 0.55, 0.88 and 1.3 nm, respectively.[16]

6.2.2 Temperature-Regulated Cell

The temperature-regulated cell used in the present study has been discussed previously by Selwyn.[17] The cell consists of a 2.2 x 10 cm quartz cylinder with fused Suprasil windows, which contains the gas. A quartz jacket envelops the inner cell; a water/ethylene glycol mix is flowed through this inner jacket. A second quartz jacket with Suprasil windows surrounds the entire assembly and is evacuated to a pressure of 5×10^{-6} Torr and sealed under vacuum. A Neslab RTE-4 thermostatted circulating bath is used to flow the water/ethylene glycol mix through the inner jacket. The temperature stability of this bath is stated by the manufacturer to be ± 0.01 °C.

In order to determine the temperature of the cell, the inlet and outlet temperatures of the water/ethylene glycol mix are measured by Teflon-encased thermistors (Omega Engineering part number 44107). Calibration of these thermistors has shown them to be accurate to ± 0.1 °C, somewhat better than the ± 0.2 °C guaranteed by the supplier. For temperatures near ambient (~ 23 °C), the temperature differential between the inlet and outlet is negligible. As the temperature setting of Neslab is increased, the temperature differential increases. At a Neslab setting of 50 °C, the temperature differential is 1.36 °C ($T_{inlet} = 49.09$, $T_{outlet} = 47.73$ °C), and at the maximum temperature setting utilized here, 75 °C, the differential is 2.69 °C ($T_{inlet} = 73.87$, $T_{outlet} = 71.18$ °C). In all cases, the effective cell temperature is taken as the average of the inlet and outlet temperatures.

6.2.3 Vacuum System

To facilitate sample handling, the cell is directly connected to a standard vacuum system consisting of a liquid nitrogen-cryotrapped glass diffusion pump backed by a small mechanical pump. Sample pressures are measured by a Texas Instruments model 145 quartz Bourdon gauge which is estimated to be accurate to $\pm 1.5\%$ as a result of calibration comparisons with 1 and 100 Torr Baratron capacitance manometers.

6.2.4 Sample

The sample was produced via the thermal decomposition of xenon(II) bisfluorosulfate, $Xe(FSO_3)_2$, a process described previously by Bartlett and coworkers.[18,19] In this synthetic scheme, $Xe(FSO_3)_2$ is initially formed by the reaction of xenon difluoride and fluorosulfuric acid at a temperature near -10 °C:

$$XeF_2\ (s) + 2\ HSO_3F\ (l) \rightarrow Xe(FSO_3)_2\ (s) + 2\ HF\ (l). \qquad (6.2)$$

After removal of the HF, the xenon(II) bisfluorosulfate is thermally decomposed at a temperature of approximately 40 °C to give the desired peroxydisulfuryl difluoride:

$$Xe(FSO_3)_2\ (s) \rightarrow Xe\ (g) + (FSO_3)_2\ (l). \qquad (6.3)$$

The $(FSO_3)_2$ product is then dried over KF to remove any remaining hydrofluoric acid. Infrared spectra showed the product to be free from contamination except for very small (less than 1%) amounts of SiF_4.

6.2.5 Experimental Procedure: Dimer Cross Sections, 180 - 360 nm

For the measurement of the $(FSO_3)_2$ cross sections at wavelengths less than 360 nm, the temperature of the cell was fixed at 25 °C, and the Cary was scanned in

1 nm steps from long to short wavelengths. A typical experimental sequence consisted of scans at five different sample pressures plus an empty cell. Wavelength intervals of different sequences were overlapped to allow for multiple checks on instrumental reproducibility.

6.2.6 Experimental Procedure: Radical and Dimer Cross Sections, 340 - 450 nm

For the measurement of FSO_3 and $(FSO_3)_2$ cross sections at wavelengths between 340 and 450 nm, the Cary step size was 5 nm. In these scans, 100 Torr of sample was initially admitted to the cell. Scans were then taken at Neslab intervals of approximately +5 °C from 30 °C to 75 °C, and then at -5 °C intervals from 72.5 °C to 27.5 °C. In order to verify that thermal equilibrium had been established before the start of each scan, the absorbance at 450 nm (primarily due to FSO_3 and therefore highly temperature dependent) was monitored as a function of time. Scans were initiated only after this absorbance had stabilized, suggesting that the new equilibrium had been reached. Under these temperature and pressure conditions, the concentration of $(FSO_3)_2$ in the cell remains essentially constant at 3.24×10^{18} molecules cm^{-3}. In contrast, the concentration of the FSO_3 radical varies by a factor of ~ 10, going from 9.17×10^{14} molecules cm^{-3} at 299.9 K to 9.74×10^{15} molecules cm^{-3} at 345.7 K.[2,3] To extract both radical and dimer cross sections from these temperature-dependent measurements, linear least-squares analysis is performed on plots of absorbance vs. FSO_3 concentration. Radical cross sections are determined from the slopes of these plots and dimer cross sections are determined from the y-intercepts.

6.3 RESULTS AND DISCUSSION

6.3.1 Dimer Cross Section Measurements at 298 K

Beer's Law plots for 298 K data at wavelengths of 200, 220 and 240 nm are shown in Figure 6-1; all wavelengths investigated at this temperature yield Beer's Law plots which are linear and pass through the origin. The absorption cross sections for $(FSO_3)_2$ resulting from the Beer's Law analyses of the 298 K data are plotted in Figure 6-2 and listed in Table 6-I, along with the dimer cross sections determined from the temperature-dependent measurements. (Also shown in Figure 6-2 are the measurements of Cobos *et al.*[4] at 193 and 450 nm.) The 298 K dimer cross sections in Figure 6-2 display no structure across the wavelength range under investigation, but instead drop smoothly and precipitously with increasing λ. Agreement between the 298 K and temperature dependent determinations is excellent at 340 nm; at longer wavelengths the 298 K cross sections are slightly high because they include absorption by the radical. The present result at 193 nm, $\sigma = 4.58 \pm 0.23 \times 10^{-18}$ cm^2, is in good agreement with that measured by Cobos *et al.*[4], $\sigma = 4.14 \times 10^{-18}$ cm^2. (Cobos and coworkers give no estimate of their experimental uncertainty at this wavelength.)

6.3.2 Temperature-Dependent Measurements

The temperature-dependent measurements of the present report yield raw data in the form of absorbances as a function of temperature for 23 wavelengths between 340 and 450 nm. In order to extract radical and dimer cross sections from these raw data, it is required that the equilibrium constant for reaction (6.1) be accurately known over the temperature range utilized here, roughly 298 - 348 K. Because of

this requirement, it is helpful to review what is known about the FSO_3 - $(FSO_3)_2$ equilibrium and explicitly consider how uncertainties in this quantity can affect the calculated cross section results.

The equilibrium constant for reaction (6.1) was first measured by Dudley and Cady,[2] who used a manometric method to obtain $K_p = 7.275 \times 10^{10}$ [exp (-11,018/T)] Torr for temperatures between 450 and 600 K. This initial result was later confirmed by Castellano and coworkers,[3] who utilized a similar technique and obtained $K_p = 6.5313 \times 10^{10}$ [exp(-10,983/T)] Torr for temperatures between 423 and 523 K. More recently, Cobos *et al.*[4] used a laser flash photolysis/absorption technique to examine forward and reverse reaction rates for reaction (6.1) between 293 and 381 K. From their data, they derived $K_c = 1.45 \times 10^{27}$ exp[-(10,730 $\pm$ 380)/T] molecules cm^{-3}. Expressed as K_p, this latter equation takes the form $K_p = 1.50 \times 10^8 \cdot T \cdot$[exp((-10,730 $\pm$ 380)/T)] Torr. Although the K_p from the first two manometric measurements[2,3] agrees with the flash photolysis K_c determination[4] to within experimental error, the slight variation between these different determinations has a substantial effect on the cross sections which are calculated from the raw data of the present report. As an example, consider the initial calculation of the FSO_3 radical concentrations for the temperature-dependent scans. If K_{eq} from reference 2 or 3 is used in the calculation, the radical concentrations in the cell take on values ranging from 9.17×10^{14} molecules cm^{-3} at 299.9 K to 9.74×10^{15} molecules cm^{-3} at 345.7 K. If K_{eq} from reference 4 is used, the calculated [FSO_3] values increase by an essentially constant factor of 1.28, and now range from 1.17×10^{15} to 1.25×10^{16} molecules

cm^{-3}. The net effect that this change has on the calculated radical cross sections is an across-the-board reduction of approximately 28%. (Note that the cross section magnitude is inversely related to the calculated $[FSO_3]$ values, so that larger radical concentrations correspond to smaller radical cross sections.) Cross section values for the dimer are affected in a less straightforward way. While those for wavelengths to the blue of 380 nm are relatively invariant with respect to which value of K_{eq} is used, those at longer wavelengths become increasingly dependent upon the choice of K_{eq}. At λ = 400 nm, the dimer cross section obtained through the use of K_{eq} from references 2 and 3 is ~ 6.5% smaller than that obtained if K_{eq} from reference 4 is used. Near λ = 430 nm, the difference is ~ 21% (Table 6-I).

Given the dependence of the calculated dimer and radical cross sections upon the choice of K_{eq}, two sets of calculations -- one corresponding to the K_{eq} from references 2 and 3, the other to the K_{eq} from reference 4 -- have been completed on the present data. (In general, the confirmed K_{eq} of references 2 and 3 should be preferred over the K_{eq} from Cobos[4] because the experimental uncertainty inherent in the manometric determinations should be less than that associated with the flash photolysis/absorption measurement.) As noted previously, these calculations consist of least-squares analysis of plots of absorbance vs. FSO_3 concentration; representative plots of this type corresponding to the use of K_{eq} from reference 2 on data for wavelengths of 380, 410 and 450 nm are shown in Figure 6-3. Cross sections for $(FSO_3)_2$ which result from analyses of the type portrayed in Figure 6-3 are listed in

Table I and plotted in Figure 6-2 while those for FSO_3 are listed in Table II and plotted in Figure 6-4, along with the previous measurements of Croce.[15]

6.3.3 Comparisons with Croce's Previous $\sigma(FSO_3)$ Measurements

The $\sigma(FSO_3)$ values of the present study are in reasonable agreement with those of Croce[15] if they are calculated with the same K_{eq}[4] used by Croce in her data analysis (Figure 6-4, Table 6-II). At wavelengths shorter than 400 nm, the present data are larger than Croce's somewhat noisier measurements by an average of 17%. This trend is inverted for wavelengths longer than 400 nm, however, and in this region the present data are, on average, 16% lower than those from reference 15. The most significant disagreements between the two sets of measurements are at 340 and 345 nm, where the present data are 56 and 69% larger than Croce's values. Although Croce[15] does not address how the use of the K_{eq} of references 2 and 3 would change her results, Cobos and coworkers[4] initially perform this calculation on their data at 450 nm and obtain the same radical cross section as is seen here, 4.2×10^{-18} cm^2. Since all of Croce's later cross section determinations are scaled relative to Cobos' initial measurement at 450 nm,[4,15] it should be roughly appropriate to scale the rest of Croce's cross section values up by a uniform factor of 4.2/3.64 = 1.15, where the 3.64 value in the denominator reflects the 450 nm cross section ultimately selected by Cobos *et al.*[4], 3.64×10^{-18} cm^2. $\sigma(FSO_3)$ results from reference 15 adjusted in this manner are in good agreement with the present results for wavelengths above 400 nm but deviate below the present data as the wavelength is decreased below this point.

6.3.4 Dimer Cross Section Measurements, 340 - 450 nm

Although the present results for the dimer are in reasonable agreement with those of Cobos *et al.*[4] at 193 nm, they disagree by a factor of eight at 450 nm. This disagreement is substantially larger than the estimated uncertainties for the two measurements at that wavelength (+300% and -75% for the current measurement, ±1% for reference 4). In order to gain insight into potential causes of this discrepancy, it is helpful to explicitly consider the experimental uncertainties which can play a role in the temperature-dependent cross section determinations.

Possible sources of error for the present set of measurements include: variations in sample composition (plus or minus a few percent), temperature (probably less than ±1 K), and pressure (±1.5%), as well as wavelength (±0.5 nm or less) and absorption (less than ±5%) uncertainties in the Cary spectrometer. Of these possibilities, the one which has the largest effect on the final, calculated dimer cross sections is the variation in the sample temperature. Although the absolute magnitude of this temperature uncertainty is relatively small, it can nonetheless produce significant changes in the y-intercepts (proportional to σ_{dimer}) of the plots of the type shown in Figure 6-3 -- while at the same time leaving the slopes (proportional to $\sigma_{radical}$) essentially unchanged. For example, an across-the-board temperature shift of -0.2 K in the sample temperatures used in the calculations at 450 nm will increase the calculated dimer cross section by almost 10%; the concurrent change in the radical cross section is only +1%. Further evidence of the temperature sensitivity of the dimer cross sections is provided by a small, systematic variation

displayed by data in Figure 6-3. Data corresponding to increasing Neslab temperatures are slightly low with respect to the best-fit, all-data line while those corresponding to decreasing Neslab temperatures are slightly high. This effect is observed at all wavelengths and is consistent with the hypothesis of a small temperature lag in the sample. In this scenario, the temperature of the sample lags slightly behind that of the Neslab and the cell, so that data corresponding to the increasing temperature sequence are plotted at $[FSO_3]$ values which are too large and those corresponding to the decreasing temperature sequence are plotted at $[FSO_3]$ values which are too small. While these variations are observed to have little effect on the slope of the plot -- and thus cannot be caused by time-dependent changes in the sample or the spectrometer -- they do yield different y-intercepts, depending on whether the line is fit to the increasing or decreasing temperature data. The net effect of these variations on a complete set of data is to cancel one another out, with the fit to the increasing (decreasing) temperature data providing a lower (upper) limit to the true dimer cross section. The present results for the dimer in the 340 - 450 nm range of Figure 6-2 include these upper and lower limits, which are shown as error bars. Although this analysis cannot by itself account for the disagreement between the present result at 450 nm and that from reference 4, it does indicate that the dimer cross section measurements are extremely sensitive to small variations in temperature. For this reason, the $\pm 1\%$ error estimated by Cobos[4] is probably unrealistically small, and may actually better reflect the *precision* of his least-squares regression rather than the overall *accuracy* of his cross section measurement.

6.4 CONCLUSION

Photoabsorption cross sections have been measured for peroxydisulfuryl difluoride, $(FSO_3)_2$, and for the fluorosulfate radical, FSO_3. For $(FSO_3)_2$, the cross sections measured at 298 K decline smoothly from 7.43 x 10^{-18} cm^2 at 180 nm to 1.27 x 10^{-21} cm^2 at 340 nm. At wavelengths in the range 340 - 450 nm, temperature-dependent measurements yield both dimer and radical cross sections. For this second set of measurements, calculated cross sections depend strongly upon the choice of K_{eq} for the dimer - radical equilibrium. If the results are calculated with the K_{eq} determined in references 2 and 3, dimer cross sections decline smoothly from 1.21 x 10^{-21} cm^2 at 340 nm to 5.42 x 10^{-23} cm^2 at 430 nm and then increase slightly to 9.31 x 10^{-23} cm^2 at 450 nm. For FSO_3, the cross sections increase from 5.51 x 10^{-19} cm^2 at 340 nm to 4.21 x 10^{-18} cm^2 at 450 nm. If the results are calculated with the K_{eq} from reference 4, the dimer cross sections decline smoothly from 1.21 x 10^{-21} cm^2 at 340 nm to 6.54 x 10^{-23} cm^2 at 430 nm and then increase slightly to 1.08 x 10^{-22} cm^2 at 450 nm. Radical cross sections increase from 4.30 x 10^{-19} cm^2 at 340 nm to 3.29 x 10^{-18} cm^2 at 450 nm. The present results are in good agreement with the previous $\sigma(FSO_3)$ measurements of Croce[15] and the 193 nm $\sigma(FSO_3)_2$ value from Cobos *et al.*,[4] but disagree markedly with the measurement of Cobos at 450 nm. Better characterization or confirmation of the $(FSO_3)_2 \rightleftarrows 2FSO_3$ equilibrium is required before more accurate $\sigma(FSO_3)$ values can be obtained from the current set of absorption data.

ACKNOWLEDGMENTS

This work was supported by the Director, Office of Energy Research, Office of Basic Energy Sciences, Division of Chemical Sciences, of the U. S. Department of Energy under Contract No. DE-AC03-76SF00098.

6.5 REFERENCES

1. F. B. Dudley and G. H. Cady, J. Am. Chem. Soc. **79**, 513 (1957).
2. F. B. Dudley and G. H. Cady, J. Am. Chem. Soc. **85**, 3375 (1963).
3. E. Castellano, R. Gatti, J. E. Sicre, and H. J. Schumacher, Z. Phys. Chem. N. F. **42**, 174 (1964).
4. C. J. Cobos, A. E. Croce de Cobos, H. Hippler, and E. Castellano, J. Phys. Chem. **93**, 3089 (1989).
5. J. Chao, R. C. Wilhoit, and B. J. Zwolinski, Thermochim. Acta **10**, 359 (1974), and references therein.
6. G. W. King, D. P. Santry, and C. H. Warren, J. Mol. Spectrosc. **32**, 108 (1969).
7. G. W. King, D. P. Santry, and C. H. Warren, J. Mol. Spectrosc. **32**, 121 (1969).
8. G. W. King, D. P. Santry, and C. H. Warren, J. Mol. Spectrosc. **32**, 138 (1969).
9. G. W. King, D. P. Santry, and C. H. Warren, J. Chem. Phys. **50**, 4565 (1969).
10. C. H. Warren, Chem. Phys. Lett. **53**, 509 (1978).
11. C. H. Warren, Chem. Phys. Lett. **68**, 407 (1979).
12. C. H. Warren, J. Mol. Spectrosc. **83**, 451 (1980).
13. C. H. Warren, J. Mol. Spectrosc. **84**, 102 (1980).
14. C. H. Warren, Chem. Phys. Lett. **72**, 233 (1980).

15. A. E. Croce, J. Photochem. Photobiol. A: Chem. **51**, 293 (1990).

16. Cary Model 118 Instruction Manual, section 5.3.

17. G. S. Selwyn and H. S. Johnston, J. Chem. Phys. **74**, 3791 (1981).

18. N. Bartlett, M. Wechsberg, F. O. Sladky, P. A. Bulliner, G. R. Jones, and R. D. Burbank, Chem. Commun. **1969**, 703 (1969).

19. M. Wechsberg, P. A. Bulliner, F. O. Sladky, R. Mews, and N. Bartlett, Inorg. Chem. **11**, 3063 (1972).

TABLE 6-I

Photoabsorption cross sections of $(FSO_3)_2$, 180 - 450 nm

λ (nm)	σ (cm^2 $molecule^{-1}$)[a]		
	298 K Measurement	Temperature Extrapolation [lower limit, upper limit]	
		K_p from ref's. 2,3	K_c from ref. 4
180	7.43 ± 0.37 (-18)		
190	5.19 ± 0.26 (-18)		
200	3.27 ± 0.16 (-18)		
210	1.90 ± 0.10 (-18)		
220	1.05 ± 0.05 (-18)		
230	5.67 ± 0.28 (-19)		
240	3.08 ± 0.15 (-19)		
250	1.59 ± 0.08 (-19)		
260	8.83 ± 0.44 (-20)		
270	5.13 ± 0.26 (-20)		
280	2.99 ± 0.15 (-20)		
290	1.76 ± 0.09 (-20)		
300	1.04 ± 0.05 (-20)		
310	6.14 ± 0.37 (-21)		
320	3.52 ± 0.25 (-21)		
330	2.09 ± 0.17 (-21)		
340	1.27 ± 0.13 (-21)	1.21 [1.07, 1.32]	1.21 [1.08, 1.32] (-21)
345	1.01 ± 0.11 (-21)	9.31 [8.05, 10.4]	9.31 [8.07, 10.4] (-22)
350	8.30 ± 1.04 (-22)	7.11 [5.88, 8.26]	7.13 [5.92, 8.28] (-22)
355	6.90 ± 0.95 (-22)	5.48 [4.28, 6.68]	5.50 [4.32, 6.69] (-22)
360	6.08 ± 0.91 (-22)	4.27 [3.12, 5.50]	4.30 [3.16, 5.50] (-22)
365		3.42 [2.31, 4.70]	3.45 [2.35, 4.70] (-22)
370		2.70 [1.66, 3.99]	2.73 [1.70, 3.99] (-22)
375		2.15 [1.17, 3.52]	2.19 [1.21, 3.52] (-22)
380		1.80 [0.86, 3.25]	1.84 [0.91, 3.23] (-22)
385		1.42 [0.56, 2.98]	1.46 [0.61, 2.95] (-22)
390		1.22 [0.41, 2.89]	1.27 [0.46, 2.83] (-22)
395		1.06 [0.31, 2.88]	1.12 [0.36, 2.77] (-22)

TABLE 6-I, continued

Photoabsorption cross sections of $(FSO_3)_2$, 180 - 450 nm

λ (nm)	σ (cm^2 $molecule^{-1}$)[a]	
	298 K Measurement	Temperature Extrapolation [lower limit, upper limit]
		K_p from ref's. 2,3 / K_c from ref. 4
400	9.38 [2.31, 28.8]	9.99 [2.81, 27.5] (-23)
405	8.46 [1.82, 29.1]	9.16 [2.34, 27.1] (-23)
410	8.10 [1.64, 28.7]	8.87 [2.19, 26.5] (-23)
415	7.03 [1.13, 29.9]	7.90 [1.67, 26.4] (-23)
420	6.56 [0.95, 29.8]	7.53 [1.51, 25.7] (-23)
425	6.60 [0.97, 29.2]	7.64 [1.61, 25.2] (-23)
430	5.42 [0.54, 32.6]	6.54 [1.06, 25.7] (-23)
435	8.03 [1.65, 27.2]	9.32 [2.59, 24.1] (-23)
440	6.56 [0.96, 28.2]	7.85 [1.76, 23.6] (-23)
445	7.18 [1.17, 28.4]	8.57 [2.08, 24.2] (-23)
450	9.31 [2.25, 27.1]	10.8 [3.50, 24.5] (-23)

****

[a]Cross sections for 180 - 360 nm are obtained from Beer's Law plots at 298 K while those for 340 - 450 nm result from temperature-dependent measurements; see the text for further details.

TABLE 6-II

Photoabsorption cross sections of FSO_3, 340 - 450 nm

λ (nm)	σ (10^{-19} cm^2 $molecule^{-1}$)[a]		
	K_p from ref's. 2, 3	K_c from ref. 4	Croce[b]
340	5.51 ± 0.28	4.30 ± 0.22	2.75 ± 0.41
345	5.62 ± 0.28	4.38 ± 0.22	2.59 ± 0.39
350	5.87 ± 0.29	4.58 ± 0.23	4.37 ± 0.66
355	6.32 ± 0.32	4.94 ± 0.25	5.82 ± 0.87
360	6.95 ± 0.35	5.42 ± 0.27	4.69 ± 0.70
365	7.73 ± 0.39	6.03 ± 0.30	4.69 ± 0.70
370	8.71 ± 0.44	6.80 ± 0.34	7.12 ± 1.07
375	9.90 ± 0.50	7.73 ± 0.39	6.79 ± 1.02
380	11.3 ± 0.6	8.80 ± 0.44	8.57 ± 1.29
385	12.8 ± 0.6	10.0 ± 0.5	9.67 ± 1.45
390	14.5 ± 0.7	11.3 ± 0.6	9.67 ± 1.45
395	16.3 ± 0.8	12.7 ± 0.6	11.5 ± 1.7
400	18.2 ± 0.9	14.2 ± 0.7	15.0 ± 2.3
405	20.3 ± 1.0	15.9 ± 0.8	19.6 ± 2.9
410	22.5 ± 1.1	17.6 ± 0.9	21.3 ± 3.2
415	24.6 ± 1.2	19.2 ± 1.0	23.4 ± 3.5
420	27.1 ± 1.4	21.2 ± 1.1	26.9 ± 4.0
425	29.5 ± 1.5	23.0 ± 1.2	27.5 ± 4.1
430	31.4 ± 1.6	24.5 ± 1.2	32.3 ± 4.9
435	35.3 ± 1.8	27.6 ± 1.4	32.3 ± 4.9
440	36.2 ± 1.8	28.2 ± 1.4	32.3 ± 4.9
445	38.8 ± 1.9	30.3 ± 1.5	34.0 ± 5.1
450	42.1 ± 2.1	32.9 ± 1.6	36.4 ± 5.5[c]

****

[a]Uncertainties quoted for the present values (±5%) do not include the contribution introduced by the uncertainty in K_{eq} for Equation (6.1).
[b]Croce (reference 15) scales her cross sections relative to the 450 nm cross section measured in reference 4 and estimates her values to be accurate to ±15%.
[c]From reference 4.

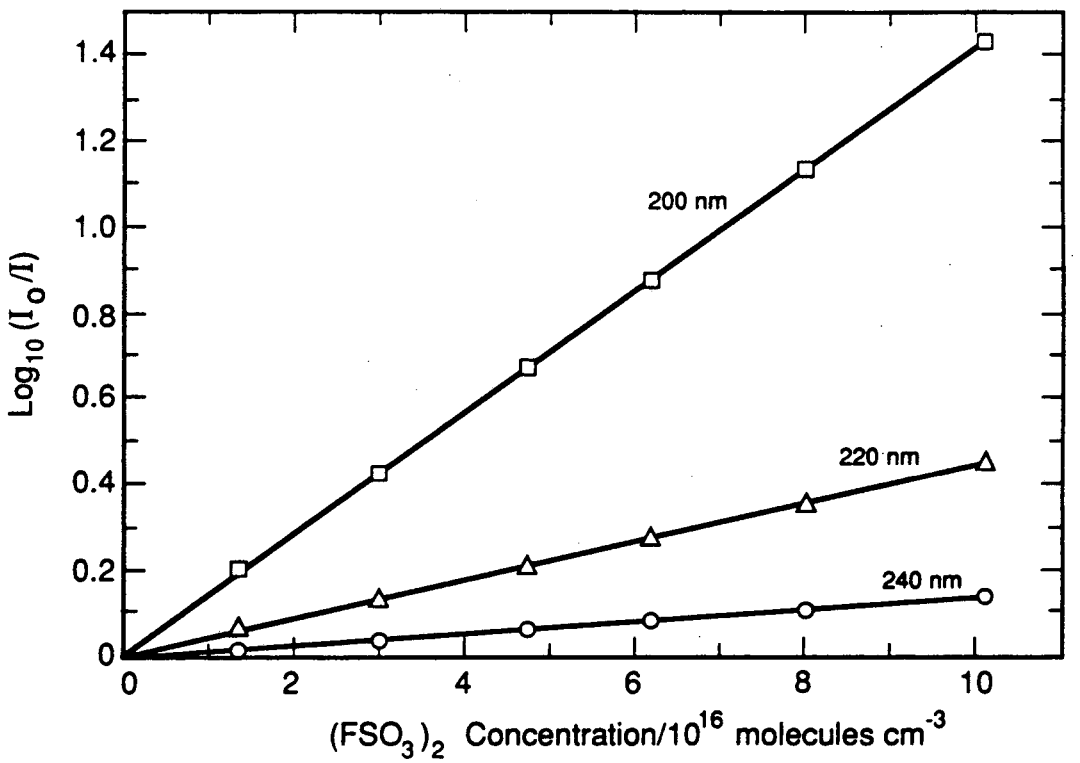

Figure 6-1. Beer's Law plots for $(FSO_3)_2$ photoabsorption at wavelengths of 200, 220 and 240 nm.

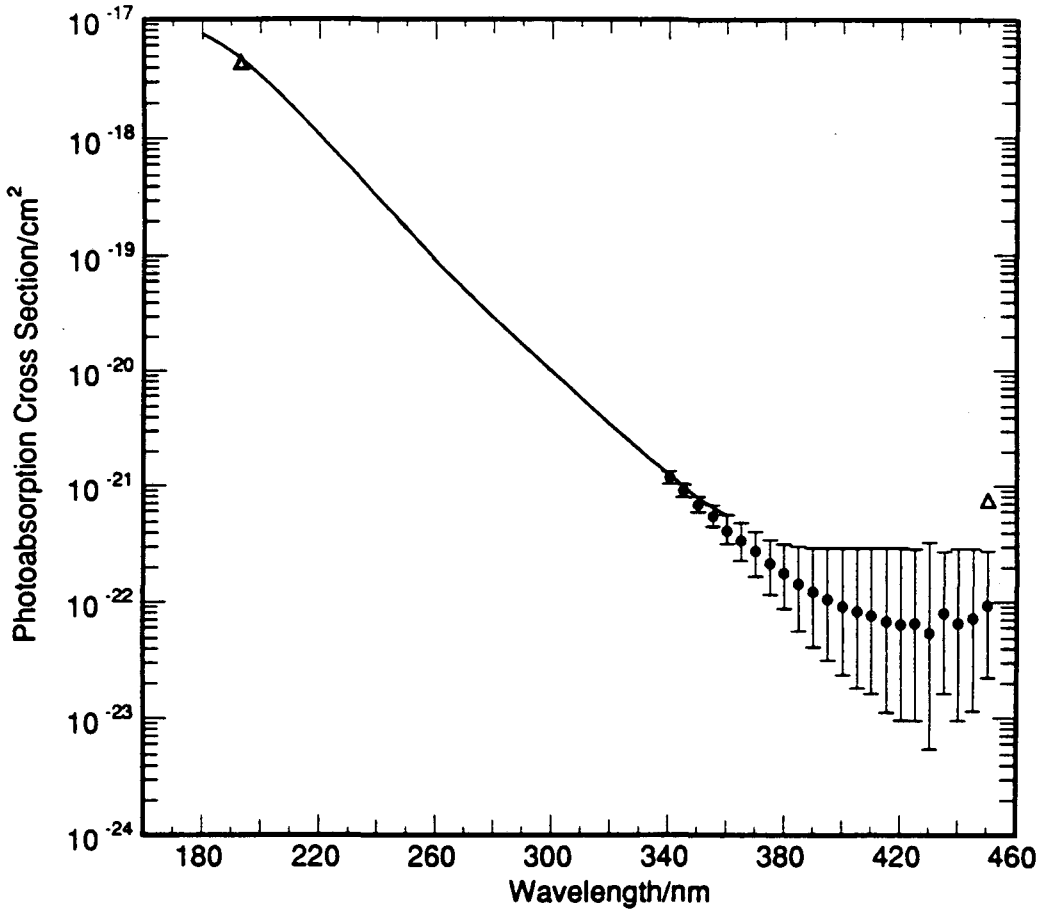

Figure 6-2. Photoabsorption cross sections for $(FSO_3)_2$. Cross sections correspond to $\sigma = [\ln(I_0/I)]/\ell c$, where ℓ is the path length of the cell (10 cm) and c is the concentration of $(FSO_3)_2$ in molecules cm^{-3}. The values obtained from Beer's Law calculations at 298 K are denoted by the solid line, while those obtained from temperature-dependent measurements using K_p from references 2 and 3 are given by the filled circles. Previous measurements at 193 and 450 nm by Cobos *et al.* (reference 4) are denoted by open triangles.

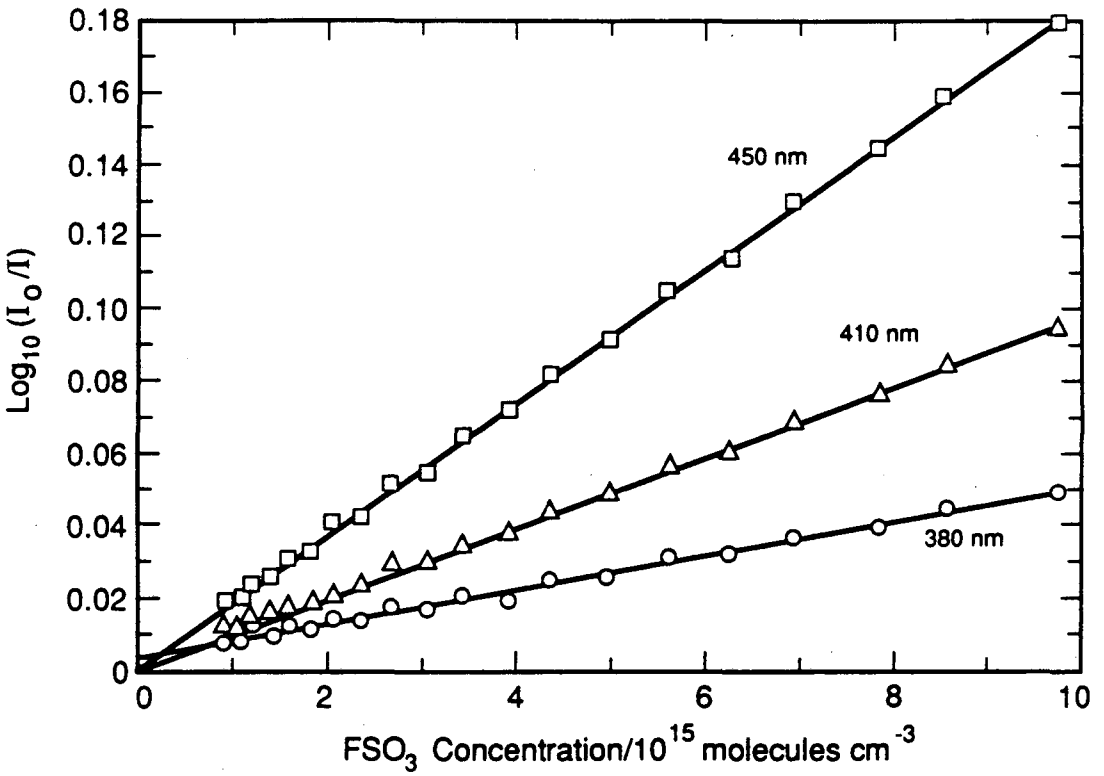

Figure 6-3. Absorbances of $(FSO_3)_2$ / FSO_3 equilibrium mixtures as a function of FSO_3 concentration for wavelengths of 380, 410 and 450 nm. For the data displayed here, the $(FSO_3)_2$ concentration remains essentially constant at 3.24 x 10^{18} molecules cm^{-3} and the temperature varies between 299.9 and 345.7 K. K_p from references 2 and 3 is used to calculate $[FSO_3]$.

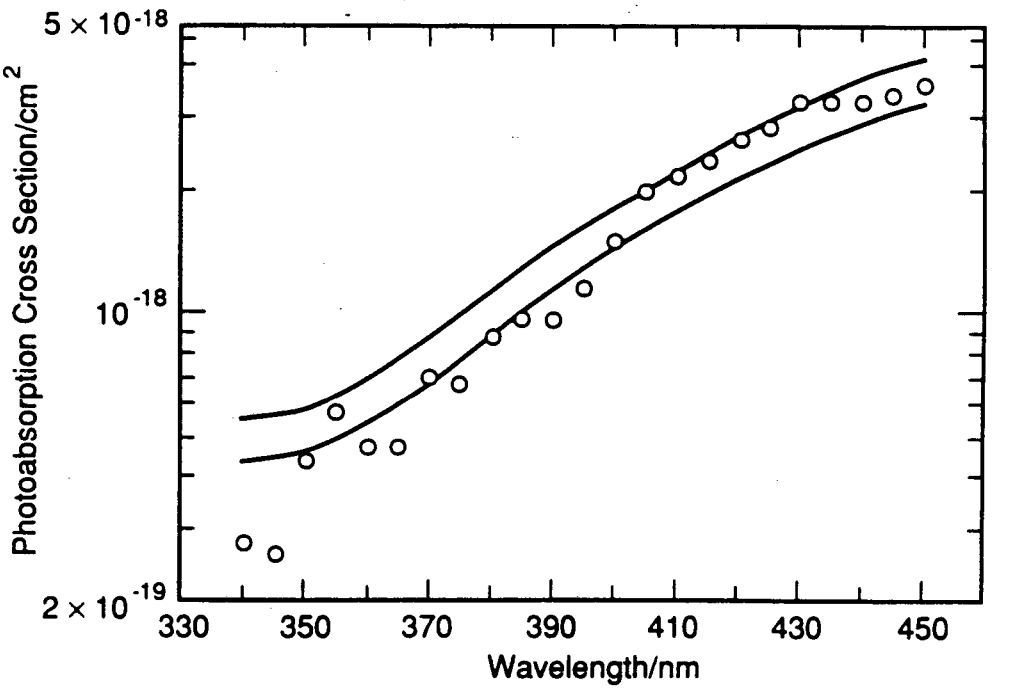

Figure 6-4. Photoabsorption cross sections for FSO_3. Cross sections correspond to $\sigma = [\ln(I_0/I)]/\ell c$, where ℓ is the path length of the cell (10 cm) and c is the concentration of FSO_3 in molecules cm^{-3}. The results obtained using the K_p from references 2 and 3 to calculate $[FSO_3]$ are indicated by the upper line; those obtained using the K_c from reference 4 are indicated by the lower line. Cross sections from Croce (reference 15) are denoted by the open circles.

Chapter Seven

Spectroscopy and Photoabsorption Cross Sections of FNO

7.1 INTRODUCTION

Nitrosyl fluoride is a colorless, highly reactive gas which was first synthesized by Ruff and Stauber in 1905.[1] Since that time its chemical and thermodynamic properties have been well studied, and a variety of synthetic schemes have been devised.[2] Spectroscopic measurements have been performed using microwave,[3-11] infrared,[4,12-21] CO laser Stark,[22] and photoelectron techniques,[23-25] and the kinetics and chemiluminescence of the $2NO + F_2 \rightleftarrows 2\ FNO$ reaction have been investigated.[26,27] These inquiries have provided detailed information about the equilibrium geometry, vibrational and rotational constants, and electronic structure of FNO, and have served as the impetus for a large number of theoretical studies.[28-52] Given the extensive amount of work on FNO in these experimental and computational areas, it is rather surprising that only *one* quantitative measurement[27] of the ultraviolet spectrum has been published.[53] In this initial UV study, Johnston and Bertin[27] (hereafter abbreviated as JB) observed a series of 18 vibronic bands over the range 340 - 260 nm. JB attributed the bulk of the spectrum to two progressions in ν_3', and obtained a value of 1,086 cm^{-1} for the ν_3' fundamental. For ν_1' and ν_2', they obtained values of 1,450 and 343 cm^{-1}. (According to the isotopic IR measurements and quadratic force field calculations of Jones *et al.*,[16] ν_1 is predominately the N=O stretching mode, ν_2 is mostly the FNO bending mode, and ν_3 is principally the N-F stretching mode. The

ground state fundamentals for these three modes are 1,844, 765, and 520 cm^{-1}, respectively.[16,21,22]) In addition to the assignment of the absorption spectrum, JB also measured quantitative absorption cross sections at a temperature of -78 °C and analyzed the visible emission spectrum of FNO^* produced via the reaction of F_2 with NO.

In the present chapter, the spectroscopy and photoabsorption of FNO are investigated in the range 350 - 180 nm. Four new spectral features not previously reported by JB are observed, along with a broad continuum absorption below 250 nm. The spectrum is assigned to a series of vibronic progressions that differs from that utilized in the earlier study but is consistent with spectroscopic analyses on the isoelectronic compound HONO. The present results are compared to the predictions of *ab initio* calculations, and to experimental and theoretical results for HONO.

7.2 EXPERIMENTAL

7.2.1 FNO Synthesis

All FNO samples used in the present investigation were formed by the direct gas phase addition of excess F_2 to a measured portion of NO in a well-passivated Monel bulb:[54]

$$F_2 + 2\ NO \rightarrow 2\ FNO. \qquad \Delta H^\circ_{298} = -74.8\ \text{kcal mol}^{-1} \qquad (7.1)$$

The FNO product formed via reaction (7.1) was then trapped out at a temperature of 77 K while the excess F_2 was pumped away. Repeated freeze-pump-thaw cycles at 77 K were then performed to insure complete removal of all unreacted F_2 and other

volatile impurities. The FNO formed via this process was found to be stable indefinitely if stored at room temperature in a thoroughly passivated Monel container.

Initially, extensive difficulties were encountered with respect to sample purity. NO_2, NO, and FNO_2 were the primary contaminants which were observed and were generally found to result from either incomplete passivation of the cell and vacuum line or NO_2 contamination of the initial NO reactant. In order to correct the latter problem, the line from the NO source bottle to the vacuum manifold was extensively purged and then passed through a liquid nitrogen\isopropanol - cooled trap to remove any remaining NO_2. (NO_2 impurities removed in this fashion will be trapped out as solid N_2O_3.) FNO samples prepared with these precautions on a well-passivated vacuum line were found to be free of the above contaminants, and gave consistent results across the full 350 - 180 nm spectral range.

7.2.2 Absorption Cell, Vacuum System

Because FNO is a highly reactive compound which attacks virtually all materials (including Pyrex, quartz, and most metals), a special absorption cell and vacuum system had to be constructed. The cell body consisted of a 10 cm length of 1.25 inch (o.d.) #304 stainless steel tubing. Two-inch diameter flanges were welded to the ends of the cell at the CaF_2 Brewster angle of 56°, and a third flange was attached to the midpoint of the cell at a 90° orientation to the main cell axis (the latter to serve as a perpendicular viewing port for future laser-based experiments). These flanges served as smooth surfaces upon which 0.25 inch thick CaF_2 windows were affixed with fluorine-resistant Techkits E-7 epoxy. The vacuum system was

constructed primarily of #304 and #316 stainless steel and consisted of a small manifold connected to a liquid nitrogen - cryotrapped mechanical pump. High vacuum Hoke bellows valves of either #316 stainless steel or Monel were utilized throughout the system, and manifold pressures were measured with a corrosion-resistant 100 Torr Baratron capacitance manometer. To permit easy attachment and removal of the cell and the FNO sample bulb, access points were equipped with #316 stainless steel Swagelok fittings. After initial passivation sequences with F_2 and FNO, both the cell and the manifold proved to be non-reactive with respect to the FNO sample.

7.2.3 Cary Spectrometer

All absorption measurements were made on a Cary 118-C spectrometer. According to the manufacturer's specifications,[55] the absolute uncertainty in λ for this particular model is determined by the accuracy of the wavelength counter. For 180 to 300 nm, the counter accuracy is specified to be ± 0.3 nm; for 300 to 350 nm it is specified to be ± 0.5 nm. Calibration checks with NO, NO_2, CS_2 and SO_2 indicate that the actual uncertainty in λ for the present instrument is within these limits. In cases where the wavelength readout of the spectrometer is observed to deviate in a consistent, reproducible manner from well-known SO_2 or NO_2 spectral features, small corrections have been applied to the data. Cross section magnitudes for these calibration gases are in good agreement (typically $\pm 5\%$ or better) with literature values. Data acquisition is controlled by an AT-type personal computer through direct interfaces to the monochromator stepping motor controller and signal output

line. For most of the scans contained in the present report the slit width of the spectrometer is fixed at 0.05 mm, so that the spectral bandwidth increases with increasing wavelength. At wavelengths of 200, 250, 300 and 350 nm the full spectral bandwidths are 0.06 nm (15 cm^{-1}), 0.12 nm (19 cm^{-1}), 0.19 nm (21 cm^{-1}) and 0.31 nm (25 cm^{-1}), respectively.[55]

For the measurement of quantitative absorption cross sections, the spectrometer step size is 0.20 nm. In these scans FNO pressures are varied between 5 and 25 Torr to check for compliance with Beer's Law, and the temperature of the sample is approximately 298 K. For the measurement of peak and shoulder locations between 350 and 250 nm the step size is 0.10 nm and FNO pressures range from 5 to 70 Torr.

7.3 RESULTS

7.3.1 Absorption Cross Sections, 350 - 180 nm

Quantitative absorption cross sections for 350 - 180 nm are given in Figure 7-1 at a resolution of 0.20 nm, and are tabulated in the Appendix in 1.0 nm intervals. The data correspond to an average of 9 representative scans, and the cross sections are estimated to be accurate to $\pm 10\%$. Cross section magnitudes are on average roughly 25% larger than those taken from the -78 °C measurement of JB,[27] with individual point-by-point comparisons displaying considerable variation about this average deviation. At wavelengths near 350, 340, 334, 311, 295, 270 and 265 nm the present results are approximately 75, 15, 5, 20, 30, 20 and 50% larger than those

from JB. (One possible explanation for the magnitude difference is the better spectral precision of the current experiment, which employs a 0.20 nm step size as opposed to 1.0 nm in JB.[27]) Qualitative agreement between the two studies with respect to peak shape and location is generally good, and the relative peak intensities in the two measurements are in approximate agreement across the full range available for comparison. This latter observation indicates that the features measured in the two studies are not hot band transitions from vibrationally excited ground state molecules. If such hot bands were present in the spectrum, their relative intensities in the present measurement (T $\approx$ 298 K) would be expected to be 3.8 (hot band from $\nu_3'' = 1$) or 7.1 (hot band from $\nu_2'' = 1$) times larger than those observed by JB at - 78°C.

At wavelengths below 250 nm the vibronic structure is replaced by a structureless, smoothly rising continuum absorption. Cross sections for this feature rise from $\sigma = 1.77 \times 10^{-20}$ cm^2 at 245 nm to 5.24×10^{-19} cm^2 at 180 nm. Since this is apparently the first experimental examination of this region of the FNO spectrum, comparisons with other measurements are not possible.

7.3.2 Vibronic Spectrum, 350 - 240 nm

A total of 22 spectral features (19 peaks and 3 well-defined shoulders) are resolved in the present report; these features are listed in Table 7-I along with the analogous measurements from Johnston and Bertin. The present data have an estimated uncertainty of ± 25 cm^{-1}, which is believed to result primarily from the inherent lack of rotational structure in the spectrum and the difficulty associated with locating the weaker spectral features (such as the shoulders), and partially from

instrumental limitations. Despite this limited resolution, the present data are in good agreement with those from JB. For the 18 features available for comparison, the average difference is -10 cm^{-1}, (i.e. the present measurements are slightly red shifted with respect to those from reference 27), and only three pairs of bands diasagree by more than 20 cm^{-1}: A5 at 35,144 cm^{-1} (low by 39 cm^{-1}), A6 at 36,153 cm^{-1} (low by 25 cm^{-1}) and A7 at 37,093 cm^{-1} (low by 50 cm^{-1}). The peak locations from JB are probably more accurate than those of the current report, given the higher resolution of their spectrometer and their better reproducibility ($\pm$15 cm^{-1}). The present measurement includes all of the peaks initially observed by JB as well as four new features: a well-defined shoulder at 36,627 cm^{-1}, and weak peaks at 38,696, 39,170, and 40,032 cm^{-1}.

Five empirical progressions in the data from Table 7-I are portrayed in Figure 7-2, where the absolute energies are plotted along the y axis and the number of active vibrational quanta (of the main mode in the progression) are plotted along the x axis. In this type of analysis, the slope of a given line indicates the excited state vibration which is active in the progression, and offsets between lines with similar slopes correspond to the presence of additional quanta of other bending or stretching modes. The five lines shown in Figure 7-2 all appear to correspond to the same vibrational progression in the excited state, with a fundamental mode of $\sim$ 1,100 cm^{-1}. Offsets of roughly 350, 480, 700 and 1,170 cm^{-1} are observed between the lowest lying progression and the four upper lines, suggesting that in addition to the $\sim$ 1,100 cm^{-1} mode, modes of 350 and 480 cm^{-1} are also active in the excited state FNO molecule.

According to this hypothesis, the 700 cm^{-1} offset results from two quanta in the 350 cm^{-1} mode, and the 1,170 cm^{-1} offset is a combination of (350 + 350 + 480) cm^{-1}. For the purposes of discussion, the five progressions will be given the labels A through E, in order of increasing energy. In this fashion the lowest progression receives the label A, and the progressions with offsets of 350, 480, 700 and 1,170 cm^{-1} are labeled B, C, D, and E, respectively.

In Table 7-II, the data from Figure 7-2 are presented according to their A - E labels, and are assigned to specific FNO transitions. Progression A is assigned to (n, 0, 0)' ← (0, 0, 0)", and progressions B through E are assigned to (n, 0, 1)' ← (0, 0, 0)", (n, 1, 0)' ← (0, 0, 0)", (n, 0, 2)' ← (0, 0, 0)", and (n, 1, 2)' ← (0, 0, 0)", respectively. These assignments differ from those proposed previously by JB,[27] who assigned the ~ 1,100 cm^{-1} mode to ν_3' and the ~ 350 cm^{-1} mode to ν_2', the excited state bend. (For ν_1', JB assigned a value of 1,450 cm^{-1} on the basis of what the current report would label (C4 - A3) and (C5 - A4).) The assignment of the ~ 1,100 cm^{-1} progression to ν_1' is supported by an analogous, carefully researched assignment in HONO[56-59] and by a number of *ab initio* calculations[37,38,40,41,44,45,49] on FNO. The assignments to ν_2' and ν_3' are less definite, but are consistent with the energetics of the ground state FNO vibrational modes[16,21,22] in that $\nu_1 > \nu_2 > \nu_3$. In addition, the assignment of ν_3' to the more active of the two lesser modes (i.e. to 350 cm^{-1} rather than to 480 cm^{-1}) is supported by a similar assignment in HONO. (In HONO, the analog to the FNO ν_3' stretch is more active in the absorption spectrum than the analog to the FNO ν_2' bend, which is apparently absent.[56-59] If the same qualitative

trends hold true for FNO, then the more active mode at 350 cm^{-1} should be assigned to ν_3'.)

In Table 7-III, successive differences down columns in Table 7-II are calculated and the resulting data are used to construct the Birge-Sponer plot shown in Figure 7-3. Linear regression analysis of the Birge-Sponer data yields a value of 1,096 cm^{-1} for the ν_1' fundamental and a slope of -25.1 cm^{-1} per quanta of ν_1'. This value for ν_1' is in good agreement with the analogous -- but differently assigned -- value from JB of ν_1' = 1,086 cm^{-1}.

In Table 7-IV, differences across rows in Table 7-II are calculated to provide estimates of ν_2' and ν_3'. Five independent estimates of ν_3' and three of $2\nu_3$' yield an average value of ν_3' = 349 cm^{-1}, in good agreement with the analogous value of 343 cm^{-1} assigned to ν_2' by JB.[27] For ν_2', three independent estimates result in an average value of 480 cm^{-1}. This value is in reasonable agreement with that obtained via reinterpretation of the data from JB according to the current assignments, 457 cm^{-1}.

7.4 DISCUSSION

7.4.1 Summary of Spectral Assignments

The present spectral assignments for FNO are summarized in Figures 7-4a and 7-4b. In Figure 7-4a, the spectrum is plotted for the range 29,000 - 35,000 cm^{-1}, and the assignments proposed in Tables 7-II through 7-IV are displayed along the lower x axis. In Figure 7-4b, the spectrum and assignments are plotted for 35,000 - 41,000 cm^{-1}. Examination of Figure 7-4a shows progressions A and B to be the dominant

features for n = 0 to n = 3, where n is the number of quanta in ν_1'. In this low energy part of the spectrum, progressions C and D appear as broad, unresolved shoulders. For the C progression, these shoulders become more intense with increasing n, so that by n = 4, the C shoulder is almost equal in intensity to the B4 peak. For the D progression, the features initially tend to decrease in intensity with incresing n. While D0 and D1 are evident as shoulders on the low energy side of the A1 and A2 peaks, D3 and D4 are unobserved. By n = 5 (Figure 7-4b), the A and B progressions have fallen off and the C peak is now the strongest of the four progressions. At this stage B is barely detectable as a very weak shoulder, and D is observed to be regaining intensity. For n = 6 to n = 8, the D progression becomes increasingly dominant, while the A and C progressions decline in intensity. Finally, at energies immediately proceeding the onset of the continuum absorption, two combination peaks corresponding to (8, 1, 2)' ← (0, 0, 0)" and (9, 1, 2)' ← (0, 0, 0)" are observed. According to the labeling scheme used here, these peaks are denoted E8 and E9, respectively.

As Figures 7-4a and 7-4b illustrate, all of the 22 spectral features contained in Table 7-I and approximately 10 additional, unresolved shoulders are consistent with five progressions in ν_1', which is calculated to have a fundamental frequency of 1,096 cm^{-1}. Some of the observed progressions involve simultaneous excitation of 1 or 2 quanta in ν_3', which is assigned a frequency of 349 cm^{-1}, and/or 1 quanta in ν_2', which is assigned a frequency of 480 cm^{-1}. None of the observed features appear to

be hot band transitions, and the spectrum is apparently fully resolved at a resolution of 0.10 nm (11 cm^{-1} at 300 nm).

7.4.2 Theoretical Studies

The first *ab initio* calculations involving electronically excited states of FNO were apparently performed by Ditchfield *et al.*[37,38], who used a minimal basis set SCF-CI technique. In their initial calculation,[37] Ditchfield and coworkers fixed the excited state FNO geometry at the ground state configuration. This method gave an energy of 3.03 eV for the vertical singlet $n_O \rightarrow \pi^*$ promotion corresponding to the $1^1A'' \leftarrow X^1A'$ transition.[37] In a later calculation,[38] Ditchfield *et al.* optimized both the ground and excited state geometries before calculating the transition energy. This method gave 0-0 transition energies of 2.84 eV and 1.46 eV for the lowest singlet and triplet states, respectively.

Although the initial, minimal basis set calculations in references 36 and 37 failed to produce energies in agreement with the observed spectrum (i.e. a vertical excitation energy of 3.98 eV and a 0-0 transition energy of 3.72 eV), later calculations employed larger basis sets and/or different computational methods which generally yielded more accurate results. Mrozek and Golebiewski[40] calculated the vertical excitation energies of the lowest lying $^{1,3}A''$ and $^{1,3}A'$ excited states via an SCF technique and obtained energies of 3.03, 1.77, 4.71 and 3.30 for the $^1A''$, $^3A''$, $^1A'$ and $^3A'$ states, respectively. In a subsequent studies,[44,45] they performed a limited CI calculation and obtained vertical excitation energies of 3.70 and 4.22 eV for the lowest lying $^1A''$ and $^1A'$ states. Vasudevan and Grein[41] carried out combined SCF

and CI calculations to determine the vertical excitation energies of 17 low lying electronic states of FNO. Their value for the first $^1A''$ state, 4.22 eV, was in good agreement with the experimentally observed 3.98 eV. Solgadi and Flament[49] calculated SCF-CI energies for the first 13 excited states and also determined potential curves along the N-F coordinate for these states. They obtained a vertical excitation energy of 4.06 eV for the lowest $^1A''$ state. This is apparently the best *ab initio* value (in terms of agreement with experiment) obtained to date.

Overall, the consensus of the theoretical studies which have been performed on electronically excited FNO is that the spectrum between 250 and 350 nm corresponds to a $1^1A'' \leftarrow X^1A'$ transition which is roughly describable in terms of an $n_O \rightarrow \pi^*$ electron promotion localized primarily on the NO entity. Excitation to the $1^1A''$ electronic state results in a 0.11 Å lengthening of the N=O bond[49] (from 1.13 Å in the ground state to 1.24 Å in the excited state). This increase in the N=O bond length is evident in the absorption spectrum in the form of lengthy progressions in ν_1' and a decrease in the ν_1 frequency from 1,844 cm^{-1} in the ground state to ~ 1,100 cm^{-1} in the excited state. The continuum absorption observed at wavelengths below 245 nm is less readily assigned, but probably consists of $2^1A'' \leftarrow X^1A'$ and $2^1A' \leftarrow X^1A'$ transitions which are predicted to occur at energies of 5.60 eV (221 nm, 45,168 cm^{-1}) and 6.00 eV (207 nm, 48,394 cm^{-1}), respectively.[49]

7.4.3 Comparisons with HONO

The vibronic structure displayed by FNO in the 350 - 250 nm region is very similar to that observed for the isoelectronic compound HONO from 400 to 300

nm.[56-59] For both molecules, progressions of broad vibronic bands are observed at intervals of ~ 1,100 cm^{-1}. Individual bands within these progressions display a striking, one-to-one correspondence to each another with respect to peak shape and intensity. (These similarities are readily demonstrated by a peak-by-peak comparison of the first four peaks of the main progression in HONO to their counterparts in the A progression in FNO [A0 through A3]. In both cases, the initial band is significantly broader and somewhat less intense than the next three peaks in the progression, while the third peak is observed to be the most intense. The fourth peak is sharper than the the first three, followed by the third and second peaks, respectively.) Quantitative absorption intensities[59] are also very similar, with both spectra displaying an absorption maximum of approximately 6×10^{-19} cm^2. The many spectral similarities suggest that the FNO and HONO absorption profiles are determined primarily by the NO entity, with minimal influence from the fluorine atom or hydroxyl group.

The photodissociation dynamics of trans-HONO have been extensively investigated via laser-induced fluoresence probing of both the OH[60-62] and NO[63] photofragments. These investigations have revealed that the OH fragments are produced translationally hot but rotationally and vibrationally cold, while the NO fragments are highly excited with respect to both rotational and vibrational motion. The photodissociation is known to proceed in the plane of the molecule, on a timescale of approximately 100 fs. Huber and coworkers[57,58] have calculated the potential energy surface for the excited state HONO complex and have concluded that the photodissociation proceeds by a rapid vibrational predissociation. They hypothesize the

presence of a low barrier along the dissociation pathway which prevents immediate dissociation of the excited state HONO complex; in order to surmount this barrier one or more quanta of energy must be transferred from the N=O stretch to the dissociative vibrational mode.

In the case of FNO a analogous picture is probably appropriate, with some minor changes. These changes must reflect the observation that while both ν_2' and ν_3' are apparently active in the FNO absorption spectrum (the latter one more so than the former), only the analog to ν_3' (ν_4' in HONO) is observed in the HONO spectrum. In addition, the few combination peaks which are observed in HONO occur with much less intensity than they do in FNO. These spectral differences suggest that although the excited state potential energy surfaces for FNO and HONO may be roughly similar to one another, differences probably exist with respect to the topography in the Franck-Condon region and in the vicinity of the photodissociation exit channel. While this conclusion that the FNO and HONO excited state surfaces are basically alike is consistent with the spectral assignments of the present report and with experimental and theoretical work on HONO,[56-59] it is apparently in conflict with two-dimensional calculations which indicate that the N-F coordinate in excited state FNO is completely dissociative.[49] A three-dimensional calculation of the FNO surface would undoubtedly prove helpful in in resolving this issue and would help to clarify the dynamics associated with FNO photoabsorption and photodissociation.

7.5 APPENDIX: FNO Photoabsorption Cross Sections, 350 - 180 nm

λ (nm)	σ (cm²)	λ (nm)	σ (cm²)	λ (nm)	σ (cm²)	λ (nm)	σ (cm²)
350.00	1.18E-20	307.00	1.56E-19	264.00	2.03E-20	221.00	8.85E-20
349.00	1.30E-20	306.00	1.18E-19	263.00	1.85E-20	220.00	9.35E-20
348.00	1.48E-20	305.00	1.04E-19	262.00	1.64E-20	219.00	1.00E-19
347.00	1.72E-20	304.00	8.85E-20	261.00	1.45E-20	218.00	1.07E-19
346.00	1.96E-20	303.00	1.04E-19	260.00	1.30E-20	217.00	1.16E-19
345.00	2.30E-20	302.00	2.54E-19	259.00	1.53E-20	216.00	1.23E-19
344.00	2.68E-20	301.00	2.31E-19	258.00	1.58E-20	215.00	1.30E-19
343.00	3.17E-20	300.00	1.56E-19	257.00	1.26E-20	214.00	1.39E-19
342.00	3.81E-20	299.00	2.31E-19	256.00	1.36E-20	213.00	1.48E-19
341.00	4.61E-20	298.00	2.20E-19	255.00	1.56E-20	212.00	1.58E-19
340.00	5.65E-20	297.00	1.41E-19	254.00	1.23E-20	211.00	1.66E-19
339.00	7.13E-20	296.00	9.15E-20	253.00	1.23E-20	210.00	1.76E-19
338.00	8.96E-20	295.00	6.75E-20	252.00	1.25E-20	209.00	1.87E-19
337.00	1.08E-19	294.00	7.11E-20	251.00	1.36E-20	208.00	1.99E-19
336.00	1.31E-19	293.00	1.81E-19	250.00	1.54E-20	207.00	2.10E-19
335.00	1.61E-19	292.00	1.19E-19	249.00	1.42E-20	206.00	2.22E-19
334.00	1.93E-19	291.00	1.13E-19	248.00	1.41E-20	205.00	2.35E-19
333.00	1.89E-19	290.00	1.70E-19	247.00	1.49E-20	204.00	2.48E-19
332.00	1.30E-19	289.00	1.66E-19	246.00	1.65E-20	203.00	2.59E-19
331.00	1.13E-19	288.00	1.04E-19	245.00	1.77E-20	202.00	2.77E-19
330.00	1.29E-19	287.00	5.78E-20	244.00	1.74E-20	201.00	2.90E-19
329.00	1.24E-19	286.00	5.17E-20	243.00	1.95E-20	200.00	3.05E-19
328.00	9.39E-20	285.00	7.45E-20	242.00	2.08E-20	199.00	3.23E-19
327.00	9.40E-20	284.00	7.26E-20	241.00	2.20E-20	198.00	3.38E-19
326.00	1.21E-19	283.00	6.59E-20	240.00	2.25E-20	197.00	3.54E-19
325.00	1.43E-19	282.00	7.58E-20	239.00	2.45E-20	196.00	3.73E-19
324.00	1.78E-19	281.00	1.01E-19	238.00	2.76E-20	195.00	3.87E-19
323.00	2.55E-19	280.00	8.26E-20	237.00	2.88E-20	194.00	4.00E-19
322.00	4.02E-19	279.00	5.03E-20	236.00	3.09E-20	193.00	4.13E-19
321.00	3.56E-19	278.00	3.41E-20	235.00	3.32E-20	192.00	4.27E-19
320.00	1.52E-19	277.00	4.44E-20	234.00	3.52E-20	191.00	4.37E-19
319.00	2.14E-19	276.00	4.24E-20	233.00	3.82E-20	190.00	4.51E-19
318.00	2.55E-19	275.00	3.77E-20	232.00	4.10E-20	189.00	4.64E-19
317.00	1.30E-19	274.00	3.97E-20	231.00	4.46E-20	188.00	4.75E-19
316.00	1.10E-19	273.00	4.30E-20	230.00	4.68E-20	187.00	4.85E-19
315.00	1.17E-19	272.00	4.47E-20	229.00	5.04E-20	186.00	4.94E-19
314.00	1.23E-19	271.00	3.06E-20	228.00	5.44E-20	185.00	5.01E-19
313.00	1.60E-19	270.00	2.81E-20	227.00	5.85E-20	184.00	5.07E-19
312.00	3.16E-19	269.00	2.66E-20	226.00	6.30E-20	183.00	5.12E-19
311.00	5.42E-19	268.00	2.10E-20	225.00	6.70E-20	182.00	5.17E-19
310.00	1.55E-19	267.00	1.99E-20	224.00	7.22E-20	181.00	5.21E-19
309.00	2.18E-19	266.00	1.96E-20	223.00	7.67E-20	180.00	5.24E-19
308.00	3.22E-19	265.00	2.67E-20	222.00	8.32E-20		

7.6 REFERENCES

1. O. Ruff and K. Stauber, Z. anorg. allg. Chem. **47**, 190 (1905).
2. For a review of FNO preparations, reactions, and physical and chemical properties, see: C. J. Hoffman and R. G. Neville, Chem. Reviews **62**, 1 (1962); C. Woolf, Advances Fluorine Chem. **5**, 1 (1965); and R. Schmutzler, Angew. Chem. Internat. Edit. **7**, 440 (1968).
3. D. W. Magnuson, J. Chem. Phys. **19**, 1071 (1951).
4. D. W. Magnuson, Phys. Rev. A **83**, 485 (1951).
5. R. L. Cook, J. Chem. Phys. **42**, 2927 (1965).
6. A. Guarnieri, G. Zuliani and P. G. Favero, Nuovo Cimento B **45**, 84 (1966).
7. K. S. Buckton, A. C. Legon and D. J. Millen, Trans. Far. Soc. **65**, 1975 (1969).
8. F. Rohwer and A. Guarnieri, Z. Naturforsch. A **35**, 336 (1980).
9. G. Cazzoli, C. Degli Esposti and P. G. Favero, Chem. Phys. Lett. **96**, 664 (1983).
10. G. Cazzoli, C. Degli Esposti, P. G. Favero and P. Palmieri, Nuovo Cimento D **3**, 627 (1984).
11. C. Degli Esposti, G. Cazzoli and P. G. Favero, J. Mol. Spectry. **109**, 229 (1985).
12. E. A. Jones and P. J. H. Woltz, J. Chem. Phys. **18**, 1516 (1950).
13. P. J. H. Woltz, E. A. Jones and A. H. Nielsen, J. Chem. Phys. **20**, 378 (1952).

14. D. W. Magnuson, J. Chem. Phys. **20**, 380 (1952).

15. J. R. Durig and R. C. Lord, Spectrochim. Acta **19**, 421 (1963).

16. L. H. Jones, L. B. Asprey and R. B. Ryan, J. Chem. Phys. **47**, 3371 (1967).

17. R. R. Smardzewski and W. B. Fox, J. Amer. Chem. Soc. **96**, 304 (1974).

18. R. R. Smardzewski and W. B. Fox, J. Chem. Soc. Chem. Comm., 241 (1974).

19. R. R. Smardzewski and W. B. Fox, J. Chem. Phys. **60**, 2104 (1974).

20. M. E. Jacox, J. Phys. Chem. **87**, 4940 (1983).

21. S. C. Foster and J. W. C. Johns, J. Mol. Spectry. **103**, 176 (1984).

22. M. Allegrini, J. W. C. Johns and A. R. W. McKellar, J. Mol. Spectry. **73**, 168 (1978).

23. D. C. Frost, S. T. Lee, C. A. McDowell and N. P. C. Westwood, J. Electron Spectry. Relat. Phenom. **7**, 331 (1975).

24. D. S. Alderdice and R. N. Dixon, J. Chem. Soc. Faraday Trans. II **73**, 245 (1977).

25. H. Bergmann, S. Elbel and R. Demuth, J. Chem. Soc. Dalton Trans., 401 (1977).

26. D. Rapp and H. S. Johnston, J. Chem. Phys. **33**, 695 (1960).

27. H. S. Johnston and H. J. Bertin, J. Mol. Spectry. **3**, 683 (1959).

28. J. P. Devlin and I. C. Hisatsune, Spectrochim. Acta **17**, 206 (1961).

29. W. Sawodny, A. Fadini and K. Ballein, Spectrochim. Acta **21**, 995 (1965).

30. S. D. Peyerimhoff and R. J. Buenker, Theoret. Chim. Acta **9**, 103 (1967).

31. C. Petrongolo, E. Scrocco and J. Tomasi, J. Chem. Phys. **48**, 407 (1968).

32. M. S. Gordon and J. A. Pople, J. Chem. Phys. **49**, 4643 (1968).

33. B. Tinland, J. Mol. Struct. **3**, 256 (1969).

34. R. D. Brown, F. R. Burden and G. R. Williams, Theoret. Chim. Acta **18**, 98 (1970).

35. J. Peslak, Jr., D. S. Klett and C. W. David, J. Amer. Chem. Soc. **93**, 5001 (1971).

36. P. S. Ganguli and H. A. McGee, Jr., Inorg. Chem. **11**, 3071 (1972).

37. R. Ditchfield, J. E. Del Bene and J. A. Pople, J. Amer. Chem. Soc. **94**, 703 (1972).

38. R. Ditchfield, J. E. Del Bene and J. A. Pople, J. Amer. Chem. Soc. **94**, 4806 (1972).

39. V. Spirko and G. K. Speirs, J. Mol. Spectry. **55**, 151 (1975).

40. J. Mrozek and A. Golebiewski, Int. J. Quantum Chem. **12**, 207 (1977).

41. K. Vasudevan and F. Grein, J. Mol. Spectry. **66**, 18 (1977).

42. L. J. Lawlor, K. Vasudevan and F. Grein, J. Amer. Chem. Soc. **100**, 8062 (1978).

43. M. J. S. Dewar and H. S. Rzepa, J. Amer. Chem. Soc. **100**, 58 (1978).

44. A. Golebiewski and J. Mrozek, Chem. Phys. Lett. **56**, 385 (1978).

45. J. Mrozek, Acta Physica Polonica A **53**, 311 (1978).

46. L. H. Jones and R. R. Ryan, J. Mol. Struct. **46**, 35 (1978).

47. G. Thyagarajan and M. K. Subhedar, Indian J. Pure Appl. Phys. **18**, 392 (1980).

48. J. S. P. Ebenezer, R. Srinivasamoorthy and G. A. Savariraj, Indian J. Pure Appl. Phys. **19**, 249 (1981).

49. D. Solgadi and J. P. Flament, Photophys. Photochem. Above 6 eV, 497 (1985).

50. L. A. Curtiss and V. A. Maroni, J. Phys. Chem. **90**, 56 (1986).

51. P. Siddarth and M. S. Gopinathan, J. Amer. Chem. Soc. **110**, 96 (1988).

52. V. Morris, G. A. Walker, P. Jones, Y. Cao, S. C. Bhatia and J. H. Hall, Jr., J. Phys. Chem. **93**, 7071 (1989).

53. Although a second UV spectrum was later published by Solgadi and Flament (reference 49) in conjunction with their *ab initio* calculations on FNO, quantitative bandhead locations and cross section magnitudes were not specified.

54. The ΔH°_{298} value for reaction (7.1) is taken from H. S. Johnston and H. J. Bertin, J. Amer. Chem. Soc. **81**, 6402 (1959).

55. Cary Model 118 Instruction Manual.

56. G. W. King and D. Moule, Can. J. Chem. **40**, 2057 (1962).

57. H. U. Suter and J. R. Huber, Chem. Phys. Lett. **155**, 203 (1989).

58. S. Hennig, A. Untch, R. Schinke, M. Nonella and J. R. Huber, Chem. Phys. **129**, 93 (1989).

59. A. Bongartz, J. Kames, F. Welter and U. Schurath, J. Phys. Chem. **95**, 1076 (1991).

60. R. Vasudev, R. N. Zare and R. N. Dixon, Chem. Phys. Lett. **96**, 399 (1983).

61. R. Vasudev, R. N. Zare and R. N. Dixon, J. Chem. Phys. **80**, 4863 (1984).

62. J. H. Shan and R. Vasudev, Chem. Phys. Lett. **141**, 472 (1987).

63. R. N. Dixon and H. Rieley, J. Chem. Phys. **91**, 2308 (1989).

TABLE 7-I

Peak Locations in the FNO Spectrum, cm^{-1}

this work[a]	Johnston and Bertin[b]	assignment[c]	label
30,010	30,011	(000)←(000)	A0
30,359	30,361	(001)←(000)	B0
31,086	31,090	(100)←(000)	A1
31,427	31,431	(101)←(000)	B1
31,645 sh	31,631	(110)←(000) ?	C1 ?
32,151	32,158	(200)←(000)	A2
32,487	32,490	(201)←(000)	B2
33,193	33,199	(300)←(000)	A3
33,547	33,537	(301)←(000)	B3
34,180	34,197	(400)←(000)	A4
34,545	34,552	(401)←(000)	B4
34,644 sh	34,630	(410)←(000)	C4
35,144	35,183	(500)←(000)	A5
35,646	35,665	(510)←(000)	C5
36,153	36,178	(600)←(000)	A6
36,627 sh		(610)←(000)	C6
36,861	36,880	(602)←(000)	D6
37,093	37,143	(700)←(000)	A7
37,787	37,798	(702)←(000)	D7
38,696		(802)←(000)	D8
39,170		(812)←(000)	E8
40,032		(912)←(000)	E9

****

[a]Present values are estimated to be accurate to ± 25 cm^{-1}. Shoulders are designated by "sh".

[b]Reference 27.

[c]Assignments correspond to $(\nu_1, \nu_2, \nu_3)' \leftarrow (0, 0, 0)''$, where double and single primes denote ground and excited state vibrational frequencies, respectively. For FNO, ν_1'' = 1,844 cm^{-1}, ν_2'' = 765 cm^{-1} and ν_3'' = 520 cm^{-1} (frequencies from references 16, 21 and 22); ν_1' = 1,096 cm^{-1}, ν_2' = 480 cm^{-1} and ν_3' = 349 cm^{-1} (data from the present report).

TABLE 7-II

Vibrational Progressions in the FNO Spectrum, cm^{-1}

	A	B	C	D	E
	(n,0,0)'	(n,0,1)'	(n,1,0)'	(n,0,2)'	(n,1,2)'
	↑	↑	↑	↑	↑
n	(0,0,0)"	(0,0,0)"	(0,0,0)"	(0,0,0)"	(0,0,0)"
0	30,010	30,359			
1	31,086	31,427			
2	32,151	32,487			
3	33,193	33,547			
4	34,180	34,545	34,644		
5	35,144		35,646		
6	36,153		36,627	36,861	
7	37,093			37,787	
8	(38,000)[a]			38,696	39,170
9					40,032

[a]Extrapolated; see Figure 7-2.

TABLE 7-III

Analysis of ν_1' Progressions, cm^{-1} (data from Table 7-II)

ν_1'	$A_n - A_{n-1}$	$B_n - B_{n-1}$	$C_n - C_{n-1}$	$D_n - D_{n-1}$	$E_n - E_{n-1}$
0					
	1,076	1,068			
1					
	1,065	1,060			
2					
	1,042	1,060			
3					
	987	998	1,002		
4					
	964		981		
5					
	1,009				
6					
	940			926	
7					
	(907)[a]			909	
8					
					862
9					

****

[a]Extrapolated; see Figure 7-2.

TABLE 7-IV

Analysis of ν_2' and ν_3', cm^{-1} (data from Table 7-II)

ν_1'	$B_n - A_n$	$C_n - A_n$	$D_n - A_n$	$E_n - A_n$
0	349			
1	341			
2	336			
3	354			
4	365	464		
5		502		
6		474	708	
7			694	
8			696	1,170
assignment:	ν_3' fund.	ν_2' fund.	$2\nu_3$' fund.	$(2\nu_3' + \nu_2')$
average value:	349 ± 22 cm^{-1}	480 ± 40 cm^{-1}	699 ± 16 cm^{-1}	1,170 cm^{-1} [a]

****

[a]This value can be compared to the sum of the averages for $2\nu_3$' and ν_2': 699 + 480 = 1,179 ± 43 cm^{-1}.

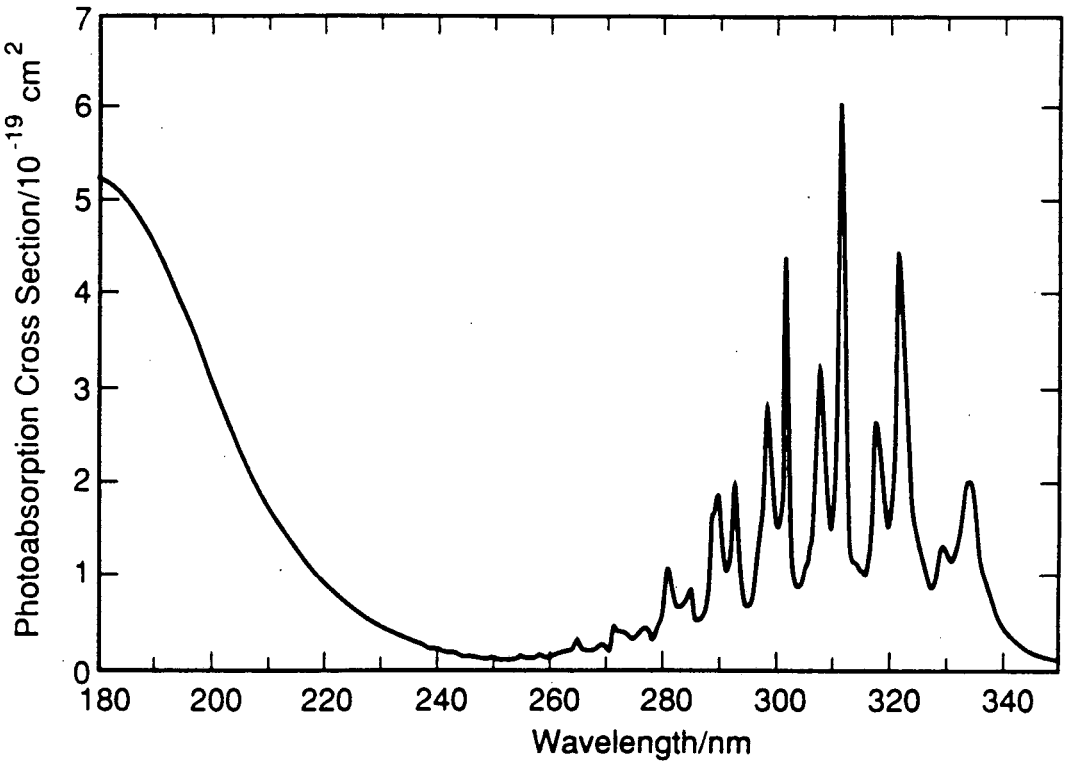

Figure 7-1. Photoabsorption cross sections for FNO. Cross sections correspond to $\sigma = [\ln(I_0/I)]/\ell c$, where ℓ is the path length of the cell (10 cm) and c is the concentration of FNO in molecules cm^{-3}. The step size of the spectrometer is 0.20 nm.

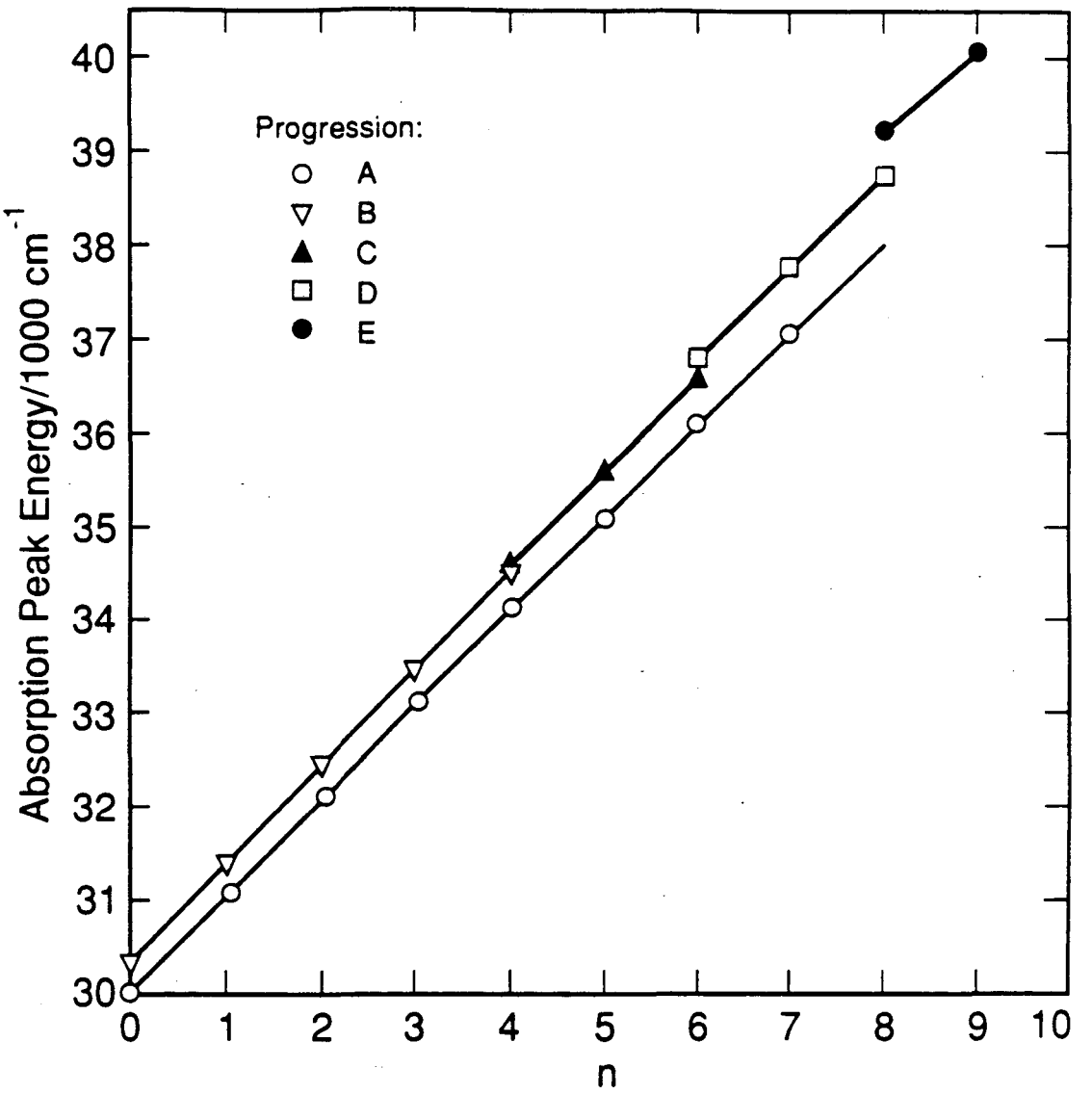

Figure 7-2. Empirical progressions in the FNO spectral data. Absolute energies of the observed peaks are plotted along the y axis, while the number of vibrational quanta in the progression are plotted along the x axis. The lowest energy progression is denoted by the open circles and is assigned the label A, while progressions which are vertically offset from the A progression by roughly 350, 480, 700, and 1,170 cm^{-1} are designated by the filled triangles (B), open inverted triangles (C), open squares (D), and filled circles (E), respectively. The line for the A progression is extrapolated one quantum to n = 8, to obtain an A8 estimate of 38,000 cm^{-1}.

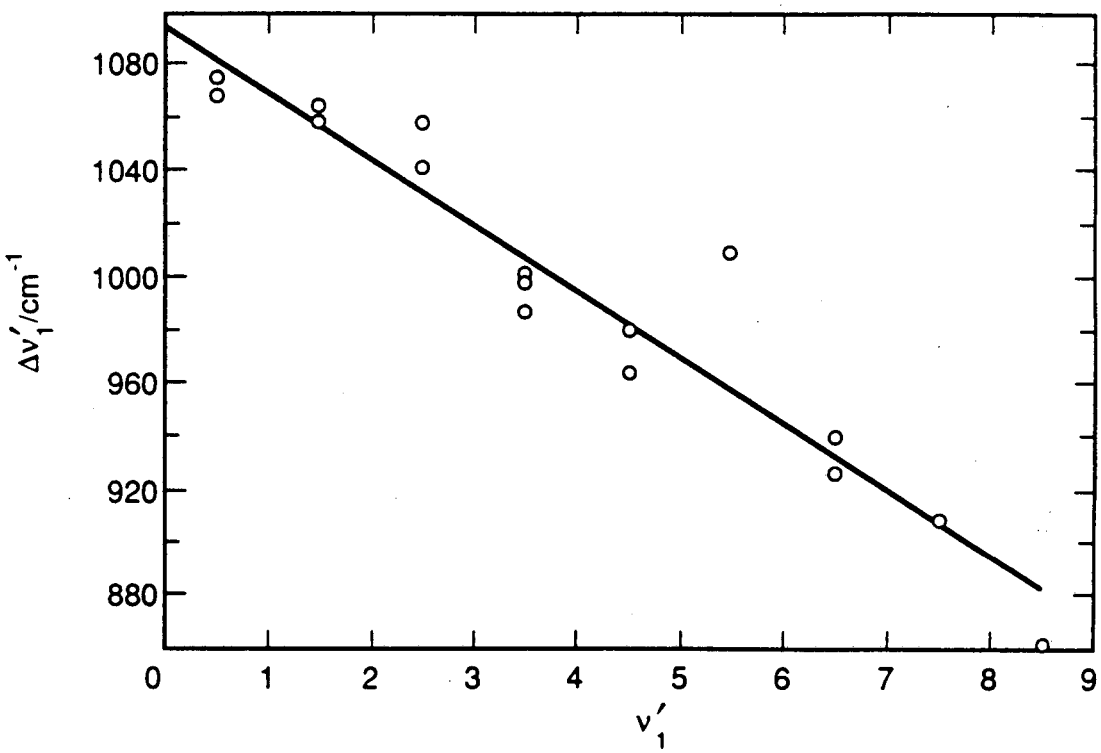

Figure 7-3. Birge-Sponer extrapolation for the excited state NO stretch progressions. The data are taken from Table 7-III, and yield a linear regression fit of $\Delta\nu_1' = 1{,}096 - 25.1\ (\nu_1')$.

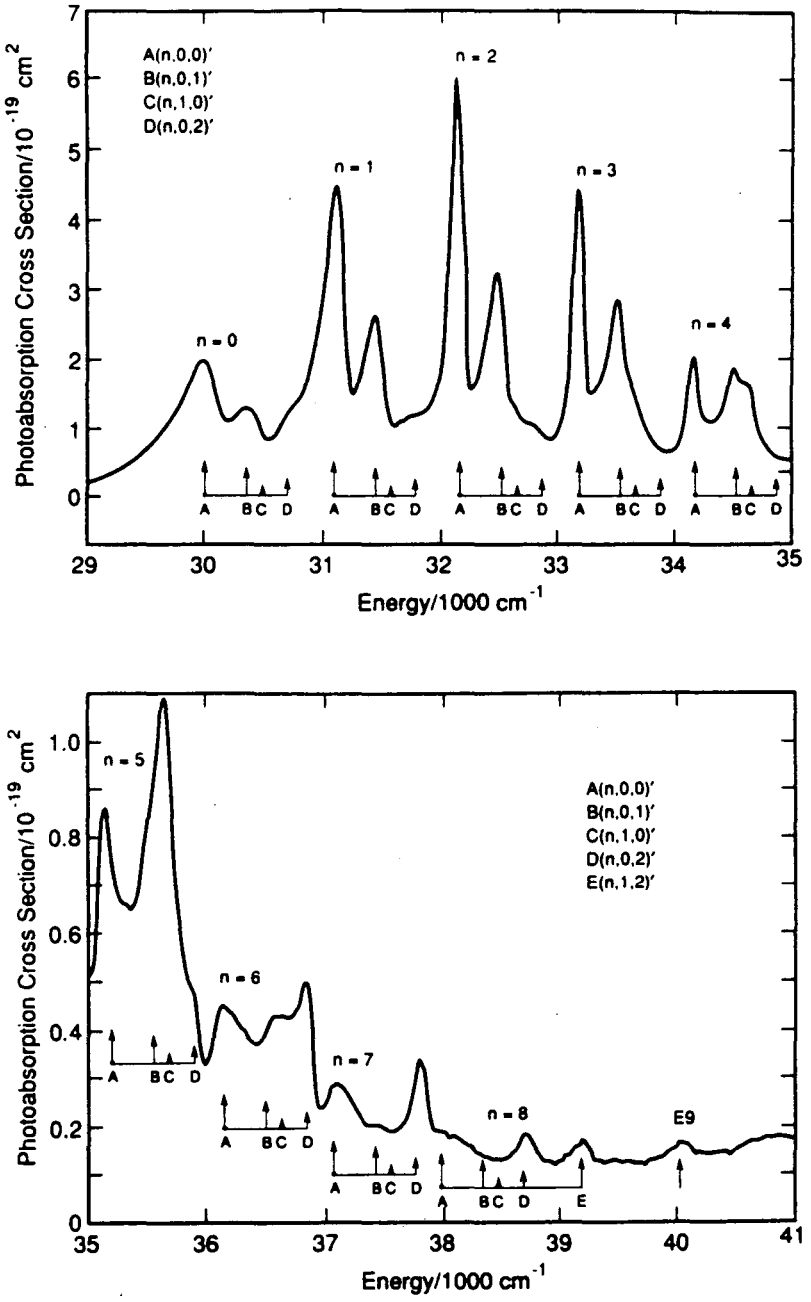

Figure 7-4. Spectrum and possible assignments for 29,000 to 35,000 cm^{-1} (part a), and for 35,000 to 41,000 cm^{-1} (part b). Peaks corresponding to the same number of quanta in ν_1'(denoted by n) are grouped together in four-pronged brackets along the lower x axis. According to this scheme, progressions A through D correspond to the transitions (n, 0, 0)' ← (0, 0, 0)", (n, 0, 1)' ← (0, 0, 0)", (n, 1, 0)' ← (0, 0, 0)", and (n, 0, 2)' ← (0, 0, 0)", respectively, while peaks E8 and E9 denote (8, 1, 2)' ← (0, 0, 0)" and (9, 1, 2)' ← (0, 0, 0)".

LAWRENCE BERKELEY LABORATORY
UNIVERSITY OF CALIFORNIA
INFORMATION RESOURCES DEPARTMENT
BERKELEY, CALIFORNIA 94720